이학박사 학위논문

Studies on Transition metal dimers in Li_2RuO_3

Li_2RuO_3의 전이금속 이합체에 대한 연구

2020 년 8 월

서울대학교 대학원

물리천문학부 물리학전공

윤석환

Studies on Transition metal dimers in Li_2RuO_3

Seokhwan Yun

Supervised by

Professor Je-Geun Park

A Dissertation submitted to the Faculty of Seoul National
University in Partial Fulfillment of the Requirements for
the Degree of Doctor of Philosophy

August 2020

Department of Physics and Astronomy

Graduate School

Seoul National University

Abstract

Transition metal ions in the oxides, which have d orbitals as a valence orbital, has been considered that the only orbital overlap between ligands and the metal is essential to describe the behavior of electrons. Recent studies, however, show that a direct overlap can be formed between the *d*-orbitals by various factors: for instance, the periodicity of the transition metal, the shape of wave functions in the t_{2g} manifold, and the local network of the metal-ligand polyhedral. In this case, the direct overlap becomes to be much essential to describe electronic behavior. Especially when those conditions are satisfied, the transition metal ions form a cluster, and the electronic wave function has to be described using molecular orbitals. In this thesis, I study on a dimer in Li_2RuO_3, which is a condensation of two transition metal ions.

The 4*d* Ru oxide Li_2RuO_3 has a layered honeycomb structure composed by edge-sharing RuO_6 octahedra. It exhibits a structural transition at $T = 550$ K, below which one-third of the Ru-Ru bonds in the honeycomb lattice becomes shorter than others by about 20%. This stable dimerization enhances the direct orbital overlap, so induces the spin-singlet, molecular orbital state. The main question of my thesis is how the dimerization influences the behavior of electrons in the Ru ion.

The Ru-Ru dimers form a herringbone pattern; thus, it expected that this system would have anisotropic physical properties reflecting ones of the dimer. The single-crystal sample was required to verify this idea and successfully synthesized. With this crystal, the anisotropies in electrical and magnetic properties were measured. The DFT calculation shows that the opening of the electronic gap requires Coulomb interaction and the correlation between electrons affects the anisotropy of the resistivity. Based on this picture, a dimer model of correlation effect was constructed to simulate the magnetic anisotropy and the calculation with the exact diagonalization method verified its validity. Those results imply that electronic correlation plays a significant role in the dimer.

X-ray Spectroscopic study is an excellent way to observe the correlated electrons directly. The experiment is carried out in the I16 beamline of Diamond Light Source. The X-ray absorption spectroscopy result shows that the energy gaps between the t_{2g} and e_g level absorption energies depend on the absorption edge; L_2 or L_3. Furthermore, resonant elastic x-ray scattering (REXS) result on (010) reflection also shows the absorption edge selective behaviors. The simulation with FDMNES, the code with a single electron approach, did not reproduce the experimental results. These results signify that not only the spin-orbit coupling of the 4*d* electrons is essential but also the direct overlap inducing the correlation exert a strong influence on the electronic structure of the dimer.

Orbital radius, according to the periodicity of the transition metal, is one of the critical conditions for forming the cluster. Series of studies on $Li_2Ru_{1-x}Mn_xO_3$ solid solution shows that the replacement with the ion with smaller orbital breaks the herringbone-patterned dimer phase at the Mn substitution rate of 20 %. Within this range, the entropy change during the structural phase transition decreases linearly with increasing the substitution rate, and the local structure around the Ru ion does not that change. Those results back up that the Mn ion does not participate in the dimer, and disrupts the inter-dimer interaction and breaks the herringbone pattern in the end. Also, the local structure measurement with the extended x-ray absorption fine structure (EXAFS) method exhibits the existence of the dimer above the transition temperature more significantly than the pair distribution function analysis with the total scattering.

Keywords: Li_2RuO_3, ruthenium oxide, dimerization, anisotropy, resonant elastic x-ray scattering, REXS, extended x-ray absorption fine structure, EXAFS

Student Number: 2015-20340

Abstract

List of Tables

List of Figures

List of Tables

List of Figures

geometry, the lobe of each orbital directs to the neighbor transition metal atom. [Ref 1. 3] (b) (Top) The energy levels of molecular orbits of Ru^{4+}-Ru^{4+} pairs in the dimer. (Bottom) The schematic figures of the wave functions of the σ-, π-, δ-molecular orbits formed by the t_{2g} orbits. [Ref 1. 16]

1.9 (a) LDA density of states (DOS) of O-2*p* and Ru-4*d*. (b) O *Kα* x-ray emission (XES) and O 1s x-ray absorption (XAS) spectra of polycrystalline Li_2RuO_3, and (c) LDA+DMFT spectral function for $U = 3$ eV and $J_H = 0.7$ eV. The LDA+DMFT spectral functions for polycrystalline Li_2RuO_3 for $U = 3$ eV and different values of J_H: (d) 0.3 eV (e) 0.5 eV, and (f) 0.7 eV. [Ref 1. 22] (g) A plot of the electronic contribution to the heat capacity (γ) versus the low-temperature value of the susceptibility (χ_0) for the Li_2RuO_3 systems with different levels of disorder (x) compared with those for other heavy fermion systems [Ref 1. 25].

2.1 Crystal growth equipment by F. Freund (crucible diameter 1.6mm). Arrangement of the materials before and after the growth process is in (a,b), respectively. The rings with spikes set like a spiral staircase to nucleate the vapor at different positions with less intergrowth of the crystals. Formation of the most massive α-Li2IrO3 single crystals appears on spikes located ~ 4 mm above the Ir starting materials. (c) Individual parts made from Al2O3 and (d) typical appearance of the tips covered with α-Li2IrO3 crystals at the bottom side, scale bar 1mm [Ref.2. 1].

2.2 (a) The cross-section of the simplified SE method. The Li_2CO_3 layer places above the RuO_2 layer. Li_2RuO_3 single crystals form at the interface of the two layers. (b) typical appearances of the crystals grown by the simplified SE method.

2.3 Non-symmorphic symmetry operations: (a) Glide plane: a reflection followed by a translation parallel with the reflection plane. (b) Screw operation: a rotation followed by a translation along the rotational axis [Ref.2. 12].

3.1 (a) Single-crystal refinement results of the Li_2RuO_3 single-crystal. The inset shows a hexagonal Li_2RuO_3 single-crystal. The horizontal (vertical) axis is the observed (calculated) scattering intensity of reflections of the Li_2RuO_3. (b) Li_2RuO_3 at room temperature, viewed along the perpendicular direction to the Ru honeycomb layer in the *ab*-plane. The yellow and green spheres represent, respectively, the Ru and Li-ions. The blue polygons represent oxygen octahedrons. There are two unequal Ru–Ru bonds, i.e., dimerized bonds (red) and two other bonds (yellow) with similar lengths. (c) X-ray diffraction image in the (hk0) plane of single-crystal Li_2RuO_3 with no sign of twinning

energy diagram of the Ru dimer in Figure 3.8c is from [Ref.3. 4].

4.1 X-ray Absorption spectra with the fluorescence-yield mode of both Ru (a) L_3 and (b) L_2 edge. The black dotted lines in both are the arctangent type background function, and the inset graphs show them in a broader range. The green (brown) Lorentzian shape peaks correspond to the photon absorption process, exciting electrons from the $2p$ core levels of Ru to the valence $4d$ t_{2g} (e_g) levels. The red lines are the summation of the absorption peaks and the background function. All measurements were carried out at 300 K.

4.2 The elements of the space group $P2_1/\mathrm{m}$ and the scattering geometry of our experiment for observing the (010) reflection of Li_2RuO_3. The pink ovals represent Ru dimers, and they contain an inversion symmetry at their center. The angle ψ in the azimuthal scan for the rotation of the scattering plane is defined between the scattering plane and the a^*-axis

4.3 The rocking curve of the (a) (010) and (b) (020) reflections at the L_3 edge. While the (020) reflection has a significant intensity in the σ-σ' scattering channel and a small signal in the σ-π' channel, the (010) reflection shows the opposite tendency. Both measurements were carried out at 300 K. (c) Temperature dependence of the intensities of the $(010)_{\sigma\pi'}$ and $(020)_{\sigma\sigma'}$ polarized reflections. The $(010)_{\sigma\pi'}$ disappears at 550 K when the system is heating

4.4 A 2d map of the intensity of the $(010)_{\sigma\pi'}$ reflection as a function of the azimuthal angle and the energy of the incident photon. The top figures are the same as Figure 4.1. Both maps have no signal at the photon energy of the e_g absorption process

4.5 Several energy cuts of the REXS spectra in Figure 4.4 The red markers represent the data at both absorption edges, and the black markers do the data measured below the absorption edges.

4.6 The calculations with the FDMNES code. (a) XAS spectra at both absorption edges. The dashed lines are the calculation without SOC, and the solid lines are with SOC. (b) the REXS spectra at the L_3 edge. The calculation at the L_2 edge was the same as that of L_3. (c) The energy cut along the red dash line in the 4.7*b*. It has a 2-fold symmetry about the azimuthal angle

5.1 Valence bond liquid phase in Li_2RuO_3. (a) Selected narrow region of the X-ray diffraction profile of Li_2RuO_3 as a function of temperature: the (10-2) reflection disappears at the structural phase transition temperature (550 K ~ 270 °C). Temperature dependence of (b) the unit cell volume and (c) the Ru-Ru bond length. (d) Pair distribution data fitting result with the C2/m

Chapter 1

Introduction

1.1 Transition metal cluster in solids

1.1.1 Bonding in solids

Identifying the nature of bonds that form a solid is essential for classifying condensed matters. Traditionally, they are classified into five categories: ionic, metallic, hydrogen, van der Waals, and covalent bonds [Ref.1. 1]. While hydrogen and van der Waals bonds are formed by the interaction between dipolar moments, the others are developed by mediating electrons. Ionic crystals are formed by the ionic bonding between negative and positive ions. For instance, NaCl consists of Na^+, a cation with high ionization energy of 5.14 eV, and Cl^-, an anion that has a significant electron affinity of 3.71 eV. In total, it requires an electron in Na 1.43 eV of energy to transfer to the Cl. Ionic bonding between the two ions reduces the energy to about 4.51 eV, making it possible to overcome the energy barrier [Ref.1. 2]. But this chemical interaction is not quantum mechanical but is completely electrostatic. On the contrary, metallic and covalent bonds are explained using the wave function of the valence electrons, which is a quantum mechanical description [Ref.1. 1]. They are the two extreme cases in which mediating electrons are placed between the cores of ion to bind the atoms. In metallic bonds, the electronic wave functions are much extensive, associated with many neighboring ions. On the other hand, the mediating electrons are bound within the range of the nearest neighbors in covalent bonds. Here, the interaction between the atoms is of prime importance. The neighboring atoms are connected by sharing pairs of electrons, or bonding pairs [Ref.1. 3]. This bond is called a molecular bond because it mainly appears in molecules. The wave function of the electrons participating in the bond is called a molecular orbital.

Generally, the bonds that compose a solid can be explained as a combination of conventional bonds. Especially when two atoms with unmatching electron affinity and ionization energy bind together, the link can be described as having an intermediate nature of an ionic and a covalent bond [Ref.1. 2]. To explain the character of the bond, the concept of electronegativity should be introduced. The larger the electronegativity of an atom is, the stronger the atom attracts a bonding pair to itself. Transition metal ions in transition metal oxides are known to have sufficiently weaker electronegativity values of 1.5 to 2.5 in the Pauling scale than those of oxygen, which is 3.44 [Ref.1. 4]. Thus the researchers, especially condensed matter physicists, consider the transition metal atoms in solids as ions. The assumption is the heart of the crystal field theory (CFT), which describes the electronic structure of the metal cation in a surrounding anionic cage [Ref.1. 5]. The CFT represents the electrons of a transition metal ion as a superposition of atomic orbitals of a metal atom.

Although CFT might be an approximate theory, it is often an accurate way to describe the magnetism of solids. The accuracy of CFT is remarkable in the case of the transition metal ions with low electron negativities such as Mn or Ti. For instance, the theory predicts S = 3/2 state as the magnetic ground state for a Mn^{4+} ion when it is at the center of the O^{2-} octahedral cage. The ion has a $3d^3$ outmost electronic shell, and the corresponding magnetic moment, in this case, is $\mu = 3.87\ \mu_B$, where μ_B is the Bohr magneton. It coincides well with the experimental value of 3.56 μ_B, which is obtained from Li_2MnO_3 [Ref.1. 6]. Magnetic states of a solid can be captured more precisely by the ligand field theory (LFT), a more rigorous version of CFT [Ref.1. 7]. In this theory, the electrons in anions are not only the sources of the crystal electric field but also the participants of the chemical bonding; thus, the molecular orbital represents electronic wave functions. In the cases of transition metal oxides, however, the results calculated from the two theories usually concur with each other because the electronegativities of the cation and the anion are significantly different.

1.1.2 Molecular Orbital and Cluster formation

Although CFT successfully describes numerous systems, it has some drawbacks that must be noted. The essential assumption, which is the localization of the *d*-orbital wave function at around the transition metal ion, can become invalid by two factors [Ref.1. 5]. The first factor is the extent of the *d*-orbital wave function. When a transition metal ion resides in an octahedron, the 5-fold degenerated *d*-orbital wave functions are split into two discrete levels, the t_{2g} and the e_g orbitals, due to its cubic symmetry. (Figure 1.1). The lobes of t_{2g} orbitals stretch towards the middle of the two oxygen ions while those of e_g orbitals directly point to the oxygen ions of the cage. As the quantum number n increases, the radial distribution of the wave function becomes sufficiently large so that the lobes of t_{2g} orbitals stick out of the oxygen cage. Therefore, the t_{2g} orbitals of a 4d or 5d ion are very likely to violate CFT. The second factor is the specific structures of the local octahedron packing. There are three possible types of packings (Figure 1.2). In the corner-sharing geometry, the transition metal ions are far away from each other compared to other circumstances. The oxygen at the shared corner interferes with the direct path from a transition metal ion to another, so the d-orbitals cannot be directly overlapped. On the other hand, the two transition metal atoms are relatively close in the different two geometries, having no obstruction of the direct overlap. In these structures, the electrons are not localized at the center of the oxygen cage anymore, so one cannot treat as atomic orbitals.

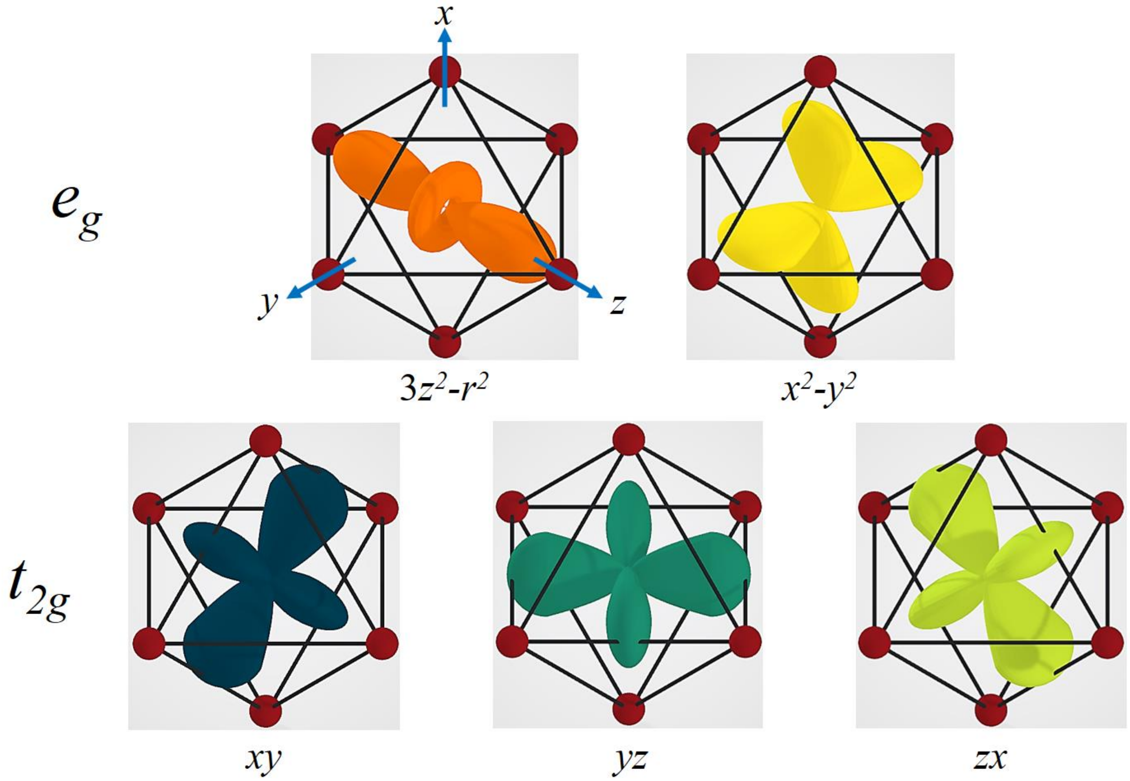

Figure 1.1 Cubic harmonics corresponding to d-orbital wave functions in an octahedral oxygen cage. (Top) $d_{3z^2-r^2}$ and $d_{x^2-y^2}$ orbitals in e_g level. (Bottom) d_{xy}, d_{yz}, and d_{zx} orbitals in the t_{2g} level.

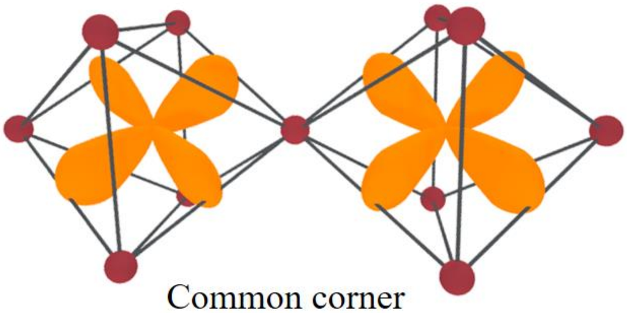

Common corner

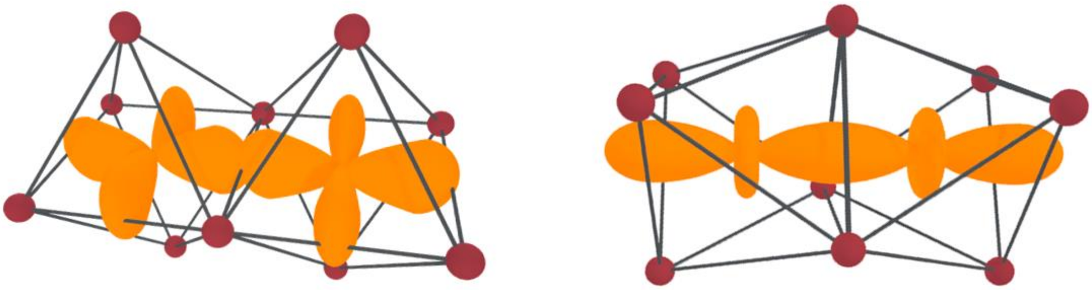

Common edge

Common face

Figure 1.2 Three types of the geometry of octahedra packing in transition metal compounds: corner-, edge-, face-sharing cases are presented. The red balls represent ligand (anions).

The most famous example is VO_2 [Ref.1. 8,9], which has a rutile structure above 67 °C. Below the temperature, it suffers a metal-insulator transition with structural distortion. The rutile structure contains edge-sharing V-centered octahedral chains along the c-axis. The chains undergo dimerization, which is the structural pairing of the vanadium ions in the chain. As a result, the V-V distances in the chain become irregular, showing long and short bonds alternatively. The top panel of Figure 1.3a shows the schematic electronic structure of VO_2. Goodenough argued that one has to discriminate between the $d_{||}$ orbitals and bands, which are formed by the t_{2g} orbitals with substantial direct overlap with the neighboring V in chains, and π^* orbitals and bands, those made of the two other t_{2g} orbitals [Ref.1. 8]. In the high-temperature rutile structure, the two electronic bands are overlapped. But when the material undergoes the dimerization, the $d_{||}$ band splits into two subbands while the π^* band does not. From the perspective of the molecular orbital theory, the substantial direct overlap generates a covalent bonding and divides the electronic states into a bonding and an antibonding state. Thus the two subbands in the electronic structure could be interpreted as a band related to the bonding state and another band associated with the antibonding state, respectively. The formation of the covalent bond can be verified by examining the $L_{2,3}$ edges of V atoms through the x-ray absorption spectroscopy. An x-ray magnetic linear dichroism (XMLD) signal, the absorption rate difference between two x-rays having orthogonal polarizations, is present in the dimerization phase. In contrast, the amplitude decreases drastically in the rutile phase (Figure 1.3b, c). Haverkort claims that the XMLD rises because the transition from the core level to an occupied state through the absorption process is prohibited [Ref.1. 9]. The result signifies that the state parallel to the c-axis, which is the $d_{||}$ orbital with low energy in Figure 1.3a, is already occupied in the dimerized phase. It is the σ-molecular orbital of the bonding state.

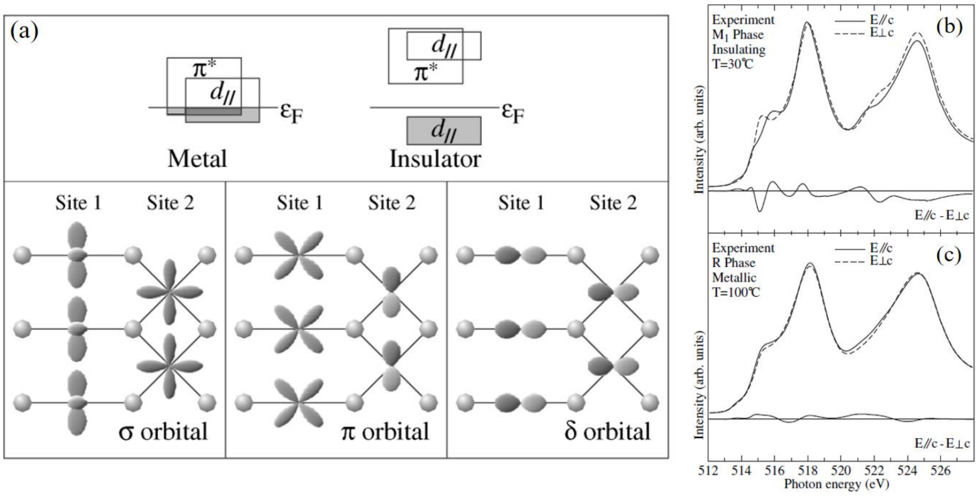

Figure 1.3 (a) Top panel: Schematic electronic structure of VO_2 Bottom panel: Definition of the relevant V 3*d* t_{2g} orbitals used in this work, drawn in the (110) plane spanned by the *a*, *b* and *c* axes of VO_2. Sites 1 and 2 are related by a 90° rotation around the *c* axis. Experimental V $L_{2,3}$ XAS spectra of VO_2 in the (b) insulating phase (T = 30 °C) and (c) metallic phase (T = 100 °C), taken with the light polarization $E \| c$ (solid lines) and $E \perp c$ (dash lines). The metal-insulator transition temperature is 67 °C [Ref.1. 9].

There are also other types of clusters composed of transition metal ions other than dimers. For instance, $LiZn_2Mo_3O_8$ has a layered kagome structure composed of Mo atoms (Figure 1.4) [Ref.1. 10]. The triangle in the kagome layer shrinks to form a trimer comprised of three Mo atoms. The three Mo have seven electrons in total, but those electrons are not localized at each site. Instead, they occupy the molecular orbital spanned by the three Mo. $Ba_5CuIr_3O_{12}$ is another example with linear trimers that consist of three iridium ions (Figure 1.5) [Ref.1. 11]. The DFT calculation shows that the bonding state is formed even in the presence of the strong spin-orbit coupling of Ir.

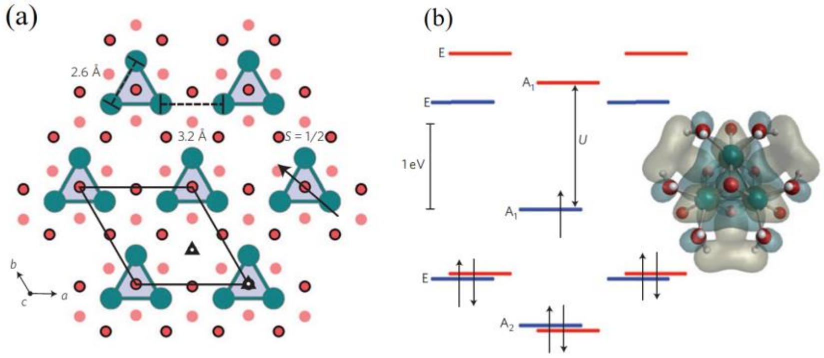

Figure 1.4 (a) Top-down view of the Mo layers showing the triangular network formed by the Mo_3O_{13} S=1/2 Clusters. (b) A spin-polarized molecular orbital diagram of $Mo_3O_{13}H_{15}$ (C_{3v}). There is one unpaired electron in the cluster, with a large energy gap to the next state. The hybrid functional estimates the on-site Coulomb repulsion energy $U \sim 1.2$ eV [Ref.1. 10]

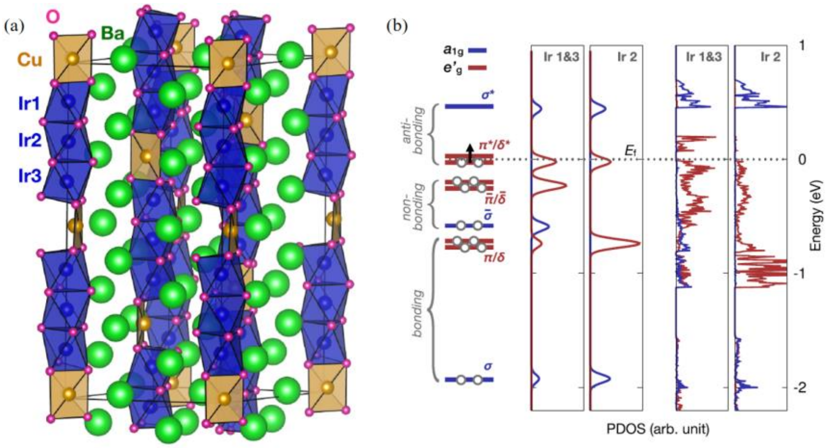

Figure 1.5 (a) The crystal structure of $Ba_5CuIr_3O_{12}$. (b) Left: Energy-level diagram showing the split of the t_{2g} states in an Ir trimer into MO states. Here, $\sigma/\pi/\delta$, $\bar{\sigma}/\bar{\pi}/\bar{\delta}$, and $\sigma^*/\pi^*/\delta^*$ denote bonding, nonbonding, and antibonding states, respectively. Electrons in filled states are represented by gray circles, while black arrows represent magnetically active electrons. Right: The Projected DOS from the simple tight-bonding model for Ir trimers and *ab initio* calculation without SOC and magnetism. The color scheme of the orbital character is the same in all graphs [Ref.1. 11].

If there are multiple electrons in the t_{2g} manifold, an intractable problem arises. There are selected orbitals that can have a direct σ-type overlap. Figure 1.6 shows the possible hopping between the t_{2g} orbitals of transition metal ions in the edge-sharing octahedra case. Only the d_{xy} orbitals have sizeable direct overlap, and the hopping between the two is represented as t_3. For the other orbitals, the unmediated hopping is not dominant. Because the hopping parameter t_1 between the two d_{xz} *and* d_{yz} orbital is too small, the electrons hop to the nearest sight via the oxygen at the joint edge with the indirect hopping constant t_2. Thus, the d_{xz} and d_{yz} orbitals could be considered as the atomic orbital of the transition metal ion.

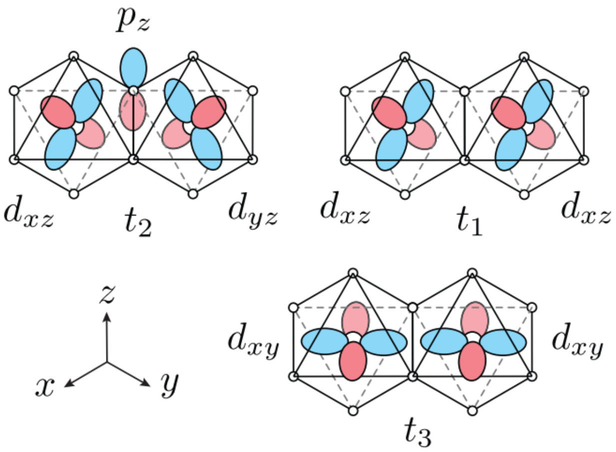

Figure 1.6 The nearest neighboring hopping in the edge-sharing octahedra case [Ref.1. 12].

There is a criterion of which direct overlap of the orbital forms a covalent bond. If the hopping (t) between two orbitals occurred by the direct hopping is sufficiently more substantial than the Hund coupling (J_H), it is possible to regard it as covalent bonding. If the opposite, it is considered as an ionic bonding between the two atomic orbitals. The Hund's coupling, which is intra-atomic correlation energy to make the spins of electrons parallel, becomes smaller as the principal quantum number n increases. On the other hand, the direct overlap and the hopping t between orbitals have the opposite tendency. Thus, the atomic and the molecular orbitals can coexist in one transition metal atom, especially in a 4*d* or 5*d* cases.

Although the electrons in those atomic orbitals have magnetic moments, there is no magnetic ordering with time-reversal symmetry breaking, such as ferro- or antiferromagnetism. Instead, they form a local singlet that can be described by the Heitler-London model (In the dimer case, $\Psi_{HL} = (c_{1\uparrow}^{\dagger} c_{2\downarrow}^{\dagger} - c_{1\downarrow}^{\dagger} c_{2\uparrow}^{\dagger})|0\rangle)$ [Ref.1. 3]. Those local singlets are arranged periodically, and this state called a valence bond solid-state (VBS) [Ref.1. 13]. There are several theoretical suggestions for VBS, such as Affleck-Lieb-Kennedy-Tasaki (AKLT) model [Ref.1. 14], but there are a few real examples. The VBS in the clustered systems accompanies severe lattice distortion, and the singlet state is well localized. Thus it is hard to expect the resonating VBS, which is an itinerant singlet state with the quantum entanglement [Ref.1. 15]. Nevertheless, it is still a fascinating system to study the entanglement associated with the singlet state of the chemical bonds.

1.2 Li_2RuO_3: The layered honeycomb structural compound with dimerization

A honeycomb lattice composed of transition metal ions is a promising system because of its possible novel states originating from certain electronic and magnetic configurations. Many factors may influence the competition between Kitaev physics, magnetism, and dimerization in the honeycomb lattice [Ref.1. 5,12] . On a microscopic level, they are governed by the strength of spin-orbit coupling and the correlation effects of several *d* electrons of transition metals [Ref.1. 3]. When the competition between these factors is fierce, especially in the case of 4*d* orbitals, the ground state of the oxides, in particular of ruthenates, becomes vulnerable to perturbations with the distinct sense of those related to the orbital degrees of freedom.

Li_2RuO_3 has a layered honeycomb structure separated by the Li layer, and the honeycomb layer is composed of edge-sharing RuO_6 octahedra [Ref.1. 16,17]. Y. Miura has reported a peculiar structural feature of this system, which is the strong transition metal dimers in the honeycomb lattice (Figure 1.7a) [Ref.1. 16]. The length of the dimerized Ru-Ru bond is 2.57 Å at room temperature, which is shorter than that in Ru metal (~ 2.65 Å) [Ref.1. 3]. Those dimers form a herringbone pattern in the honeycomb lattice. Whereas the other Ru-Ru bonds that are not dimerized are longer than the dimer with a length of about 3.05 Å. This dimerized system goes through a structural transition at a quite high transition temperature of 550 K. After the transition, the honeycomb lattice becomes ideal, and the space group changes from $P2_1/m$ to $C2/m$.

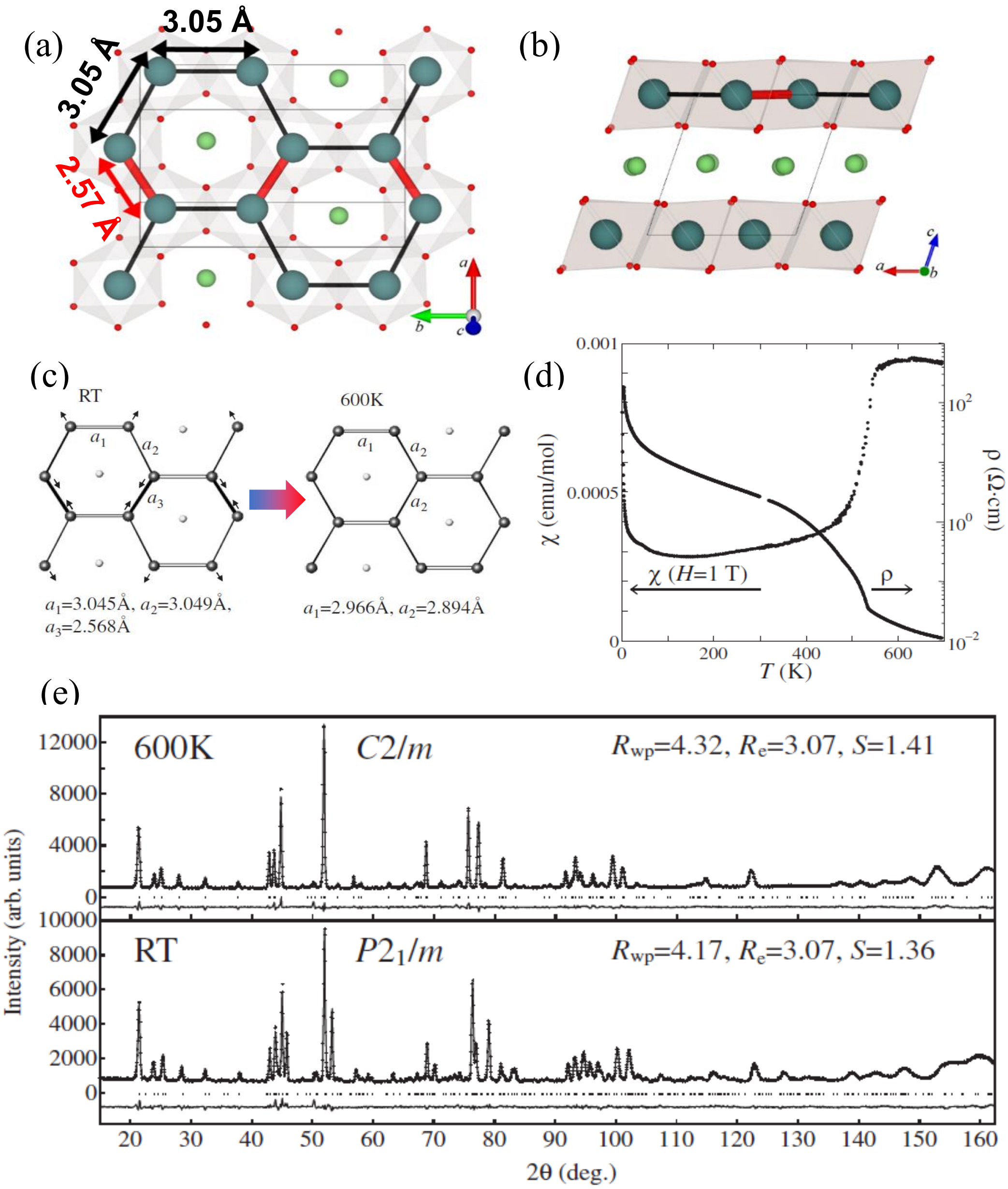

Figure 1.7 The ab-plane (a) and ac-plane of Li_2RuO_3 (b). The green (red) spheres in the figures are Ru (O), and the light green circles represent Li atoms. (c) The Ru honeycomb lattices at 600 K (right, C2/m) and room temperature (left, $P2_1/m$). (d) Temperature dependence of magnetic susceptibility (χ) measured under magnetic field H = 1T and the electric resistivity (ρ) of Li_2RuO_3 [Ref.1. 16]

This structural distortion influences several physical properties of this system, especially the magnetic property. In the $P2_1/m$ phase, it has a small and nearly temperature-independent magnetic susceptibility over a wide range of temperatures. It increases suddenly and shows a paramagnetic behavior above the transition temperature as in a transition from an antiferromagnetic ordering. Nevertheless, the neutron diffraction result does not show any magnetic reflection that occurs from the magnetic order (Figure 1.7e). These features, such as the structural deformation, the sudden drop of the magnetic moment, and the lack of long-range magnetic ordering, indicate the formation of a molecular orbital in the Ru dimer. The electrical resistance of the system is also noteworthy. It shows semiconducting behavior over the whole temperature range, although there is an abrupt change at the transition temperature. If this is a typical dimerization originating from Peierls' transition, which happens from the Fermi surface instability of the system, it has to be metallic above the transition temperature. However, it is still an insulator, even after the structural distortion vanishes.

G. Jackeli and D. I. Khomskii presumed that the spontaneous dimerization is induced by the orbital degrees of freedom of the partially field t_{2g} levels of Ru ion in the honeycomb lattice [Ref.1. 18]. The oxidation number of the Ru ion is +4, and there are four $4d$ electrons in the t_{2g} manifold, which have a three-fold spin and a three-fold orbital degeneracy. The system is mathematically described by the Kugel-Khomskii type spin-orbital Hamiltonian [Ref.1. 19]. They showed that the undistorted honeycomb has structural instabilities towards symmetry reductions and the spins of the $4d$ electrons in the t_{2g} manifold couples into a quantum spin-singlet dimer with a spin gap. They also demonstrated that the herringbone-patterned ordering of the dimers has the smallest energy among the possible states because the pattern has the most significant possible number of dimers without forming long Heisenberg chains.

They analyze this model in the zero Hund's coupling limit, in which every spin configuration has the same energy. It could be valid if the overlap between the d-orbitals is significant enough to ignore the intra-atomic correlation energy. Thus one has to examine the local geometry of RuO_6 octahedron and the connection between them to discuss the validity of the assumption. The RuO_6 octahedra are connected through a common-edge network. In this configuration, two RuO_6 octahedra share two adjacent oxygen at the corner. The distance between the two transition metal atoms is much closer than that of the corner-sharing case. The length of the Ru-O bond is almost independent of the local geometry of RuO_6 and is about 2.0 Å. For an ideal octahedron, the interatomic distance between the nearest two Ru atoms of the edge-sharing structure is only 70 % of that of the corner-sharing case (Figure 1.2).

The edge-sharing case guarantees a considerable direct σ-type overlap between the *d*-orbitals and forms the Ru dimer to enhance the electronic hopping between the transition metal atoms. The hopping constant of the direct σ-type overlap between the d-orbitals ($t_{dd\sigma}$) is ~ 1.2 eV for Li_2RuO_3 [Ref.1. 20]. This value is larger than the strength of Hund's coupling of Ru, which is about 0.4 eV [Ref.1. 21]. Therefore, the model in zero-Hund's coupling limit is reasonable to explain the origin of the dimerization.

But the limit does not apply to all t_{2g} orbitals due to the directional nature of the t_{2g} wave functions (Figure 1.8). Notably, the directional nature of the orbitals is known to have a more massive effect in the edge-sharing octahedral geometry than in the corner-sharing one. The valence Ru electrons of the in-plane orbitals form the *σ*-bonds stronger than the intra-atomic Hund's coupling. However, the electrons in the orbitals that are orthogonal to the Ru_2O_2 dimer plane form a weaker oxygen-mediated bonding. The strength of the fragile bonds is estimated to be less than 0.3 eV [Ref.1. 20], which is smaller than the Hund's energy. Therefore, only the strong *σ*-bonds play a leading role in the dimerization, and the transition is called the orbital-selective Peierls transition (OSPT) [Ref.1. 3].

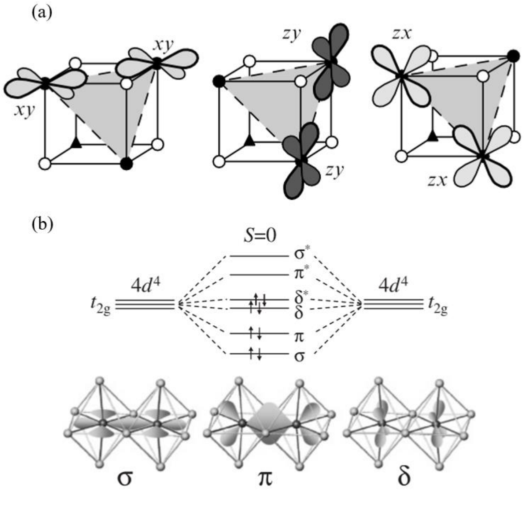

Figure 1.8 (a) the directional nature of t_{2g} orbital wave functions (d_{xy}, d_{yz}, d_{zx}). In the edge-sharing geometry, the lobe of each orbital directs to the neighbor transition metal atom. [Ref.1. 3] (b) (Top) The energy levels of molecular orbits of Ru^{4+}-Ru^{4+} pairs in the dimer. (Bottom) The schematic figures of the wave functions of the σ-, π-, δ-molecular orbitals formed by t_{2g}. [Ref.1. 16]

Although the source of the dimerization in Li_2RuO_3 is apparent, there are some remaining questions. The electrons participating in the strong σ-bond do not contribute to the physical properties such as electrical resistivity and magnetism due to their substantial binding energies [Ref.1. 20]. These electrons are located a few eVs below the Fermi-level in the band picture; therefore, it is electrically inactive. The dynamical mean-field theory (DMFT) calculation in the previous research shows that the electrons in the orbital-selective singlet state have no contribution to the magnetic susceptibility due to its large spin gap [Ref.1. 20]. On the other hand, the electrons belonging to the weaker bonds, which is located near the Fermi-level, would directly affect the physical properties of Li_2RuO_3. Thus, the response of the dimerized ruthenate originates from the electrons influenced by a small electric or magnetic field.

Still, the σ-bond can indirectly modify the physical properties because the electronic structure relevant to the oxygen-mediated bonding is significantly affected by the local dimerization [Ref.1. 17]. In particular, the bands occupied by the mediating electrons are degenerate at the boundary of the Brillouin zone owing to the non-symmorphic lattice symmetry of 2_1, which somehow is overlooked in the previous calculations [Ref.1. 17]. This degenerate band can easily be perturbed by the considerable spin-orbit coupling of Ru and form flat bands, which itself is a very intriguing observation with potentially fascinating possibilities to explore.

There are several experimental results to offer a clue to help understand this system. The electronic structure of Li_2RuO_3 was studied by examining the *K*-edge of the oxygen through x-ray spectroscopy as well as the theoretical calculations using the local density approximation (LDA) and its combination with DMFT (LDA+DMFT) [Ref.1. 22]. The study showed that the electrons of the weaker bonds could be regarded as local atomic orbitals rather than the molecular orbital. That is, they proved that the electrons that can be represented as the local atomic orbital states that are much more susceptible to Coulomb interaction U, unlike when it is described as the molecular orbital which is almost unresponsive to the interaction. Along with the X-ray study, the nuclear magnetic resonance (NMR) data show that there are remaining magnetic moments in the atomic orbital states. However, it is smaller than the non-interacting case [Ref.1. 23,24]. The NMR study also confirmed that the super-exchange interaction via oxygen in a common-edge plays a crucial role in the localization of the moments while the direct-exchange interaction between the d-orbitals is dominant in the molecular orbital picture. In conclusion, the results display that the correlation between the localized atomic moments is also significant for understanding the insulating system. Notably, this correlation effect becomes the main component that determines the physical properties of the system as the dimer is broken by doping [Ref.1. 25]. Despite the doping, the system is not converted into a metallic system. Instead, the electrons are dragged by themselves. Therefore the Sommerfeld-Wilson ratio, which is 1 for the free electron gas, is highly decreased.

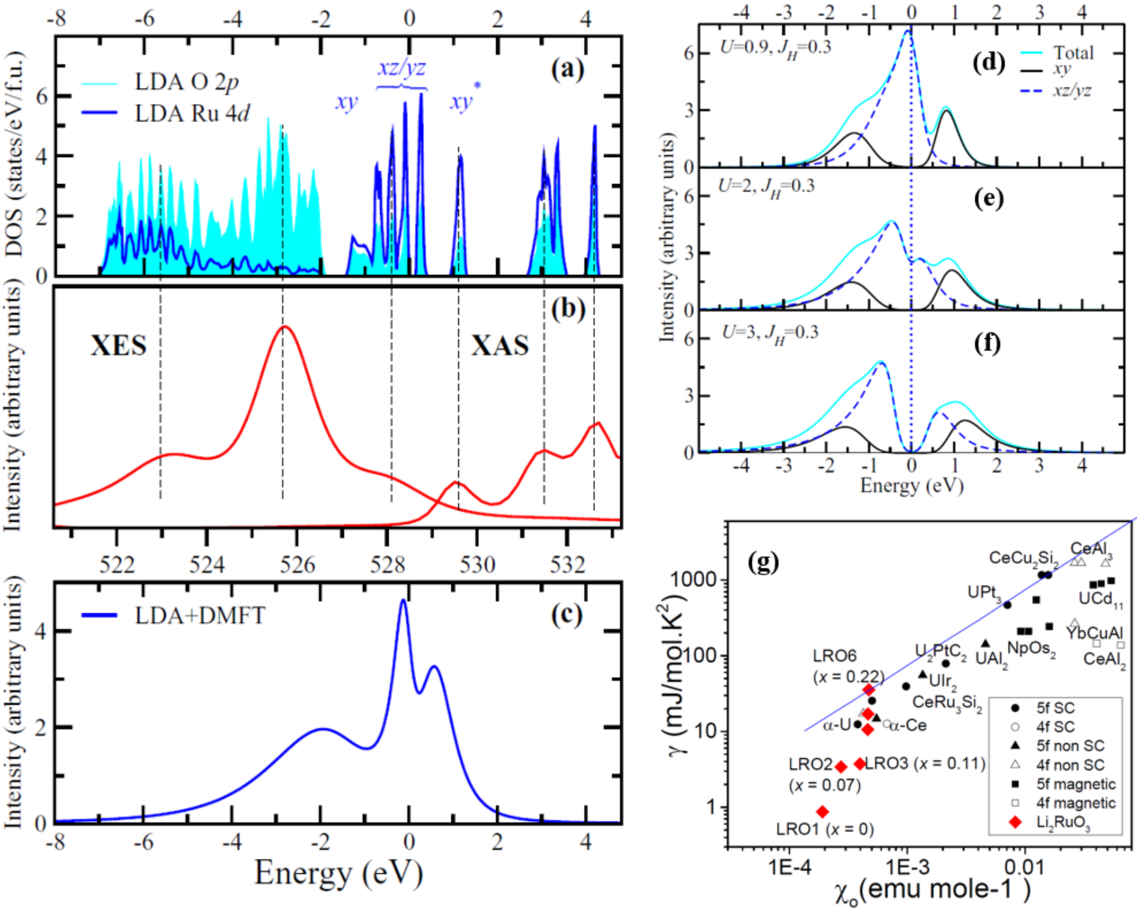

Figure 1.9 (a) LDA density of states (DOS) of O-2*p* and Ru-4*d*. (b) O *Kα* x-ray emission (XES) and O 1s x-ray absorption (XAS) spectra of polycrystalline Li_2RuO_3, and (c) LDA+DMFT spectral function for *U* = 3 eV and J_H = 0.7 eV. The LDA+DMFT spectral functions for polycrystalline Li_2RuO_3 for *U* = 3 eV and different values of J_H: (d) 0.3 eV (e) 0.5 eV, and (f) 0.7 eV. [Ref.1. 22] **(g) A plot of the electronic contribution to the heat capacity (γ) versus the low-temperature value of the susceptibility (χ_0) for the Li_2RuO_3 systems with different levels of disorder (x) compared with those for other heavy fermion systems. [Ref.1. 25]**

Besides, this system behaves bizarrely above the structural transition temperature. As the XRD result indicates, there is no structural distortion signifying the dimerization above transition. However, the pair distribution function analysis (PDF) with total scattering measurement manifests the dimerized states [Ref.1. 26]. These local dimers rising from the thermal fluctuations are called the valence bond liquid (VBL) state. Because the phase transition to the VBL state accompanies the sudden change of volume and release of latent heat during the phase transition as when the ice melts, it seems like a first-order phase transition. Nonetheless, the recent Raman scattering experimental result shows that the phase transition has the combined features of both first- and second-order transitions. That is, some phonon lines shift with a drastic softening of their frequencies, which is a characteristic of a first-order transition. In contrast, others change continuously, indicating the second-order transition [Ref.1. 27].

1. 3 Outline of the thesis

Throughout this thesis, the transition metal dimer and their ordering in Li_2RuO_3 are discussed. Chapter 2 introduces the pivotal experimental techniques of the research, such as Li_2RuO_3 single-crystal synthesis, and resonant elastic x-ray scattering (REXS). It is well known that growing a single-crystal sample containing lithium in the chemical formula is quite delicate. To successfully synthesize the challenging material, the separated educts method was used, which is a modified chemical vapor transport method. The chapter provides the details of the synthesis as well as the description of REXS. A synchrotron light source is an efficient tool to investigate condensed matters. It is mainly because the generated photons have a broad range of energy. Since every element has the characteristic absorption energy of a photon, various scattering techniques are available. REXS is a novel diffraction method for observing charge, magnetic, and orbital orderings in a solid. Because the scattering amplitude that can be obtained from general x-ray scattering experiments is weak, the broken symmetries are hard to be observed. Fortunately, the resonant scattering allows us to illuminate and discover them. In Chapter 3, the correlation effect associated with the dimer of Li_2RuO_3 is explained through the investigation of the anisotropic physical properties. The anisotropy of the resistivity and the magnetic susceptibility are measured and compared with the DFT calculation result. The REXS study that reveals the physics of the t_{2g} orbitals is presented in the following chapter 4. The examination of the resonant reflection measured by REXS explains the orbital ordering in Li_2RuO_3. Throughout the final chapter, the evolution of the VBL state in Li_2RuO_3 is explored by doping Mn ions. The physical characterization of the $Li_2Ru_{1-x}Mn_xO_3$ suggests how the liquid state can reside in the solid.

References

[Ref.1.1] Kittel C, *Introduction to Solid State Physics, 8th Edition, Berkeley* (1996).

[Ref.1.2] H. Ibach and H. (Hans) Lüth, *Solid-State Physics : An Introduction to Principles of Materials Science* (Springer, 2009).

[Ref.1.3] S. V. Streltsov and D. I. Khomskii, Phys. - Uspekhi **60**, 1121 (2017).

[Ref.1.4] L. Pauling, J. Am. Chem. Soc. **54**, 3570 (1932).

[Ref.1.5] D. I. Khomskii, *Transition Metal Compounds* (Cambridge University Press, Cambridge, 2014).

[Ref.1.6] S. Lee, S. Choi, J. Kim, H. Sim, C. Won, S. Lee, S. A. Kim, N. Hur, and J. G. Park, J. Phys. Condens. Matter **24**, (2012).

[Ref.1.7] C. A. Daul, J. Phys. Conf. Ser. **428**, (2013).

[Ref.1.8] J. B. Goodenough, J. Solid State Chem. **3**, 490 (1971).

[Ref.1.9] M. W. Haverkort, Z. Hu, A. Tanaka, W. Reichelt, S. V. Streltsov, M. A. Korotin, V. I. Anisimov, H. H. Hsieh, H. J. Lin, C. T. Chen, D. I. Khomskii, and L. H. Tjeng, Phys. Rev. Lett. **95**, 196404 (2005).

[Ref.1.10] J. P. Sheckelton, J. R. Neilson, D. G. Soltan, and T. M. McQueen, Nat. Mater. **11**, 493 (2012).

[Ref.1.11] M. Ye, H. S. Kim, J. W. Kim, C. J. Won, K. Haule, D. Vanderbilt, S. W. Cheong, and G. Blumberg, Phys. Rev. B **98**, 201105 (2018).

[Ref.1.12] S. M. Winter, A. A. Tsirlin, M. Daghofer, J. Van Den Brink, Y. Singh, P. Gegenwart, and R. Valentí, J. Phys. Condens. Matter **29**, (2017).

[Ref.1.13] N. Read and S. Sachdev, Phys. Rev. B **42**, 4568 (1990).

[Ref.1.14] I. Affleck, T. Kennedy, E. H. Lieb, and H. Tasaki, Phys. Rev. Lett. **59**, 799 (1987).

[Ref.1.15] Y. Zhou, K. Kanoda, and T. K. Ng, Rev. Mod. Phys. **89**, 025003 (2017).

[Ref.1.16] Y. Miura, Y. Yasui, M. Sato, N. Igawa, and K. Kakurai, J. Phys. Soc. Japan **76**, 033705 (2007).

[Ref.1.17] S. Yun, K. H. Lee, S. Y. Park, T. Y. Tan, J. Park, S. Kang, D. I. Khomskii, Y. Jo, and J. G. Park, Phys. Rev. B **100**, 165119 (2019).

[Ref.1.18] G. Jackeli and D. I. Khomskii, Phys. Rev. Lett. **100**, 147203 (2008).

[Ref.1.19] K. I. Kugel and D. I. Khomskii, Sov. Phys. - Uspekhi **25**, 621 (1982).

[Ref.1.20] S. V. Streltsov and D. I. Khomskii, Phys. Rev. B **89**, 161112(R) (2014).

[Ref.1.21] D. Sutter, C. G. Fatuzzo, S. Moser, M. Kim, R. Fittipaldi, A. Vecchione, V. Granata, Y. Sassa, F. Cossalter, G. Gatti, M. Grioni, H. M. Rønnow, N. C. Plumb, C. E. Matt, M. Shi, M. Hoesch, T. K. Kim, T. R. Chang, H. T. Jeng, C. Jozwiak, A. Bostwick, E. Rotenberg, A. Georges, T. Neupert, and J. Chang, Nat. Commun. **8**, 1 (2017).

[Ref.1.22] Z. V. Pchelkina, A. L. Pitman, A. Moewes, E. Z. Kurmaev, T.-Y. Tan, D. C. Peets, J.-G. Park, and S. V. Streltsov, Phys. Rev. B **91**, 115138 (2015).

[Ref.1.23] P. J. Reeves, I. D. Seymour, K. J. Griffith, and C. P. Grey, Chem. Mater. (2019).

[Ref.1.24] I. Y. Arapova, A. L. Buzlukov, A. Y. Germov, K. N. Mikhalev, T.-Y. Tan, J.-G. Park, and S. V. Streltsov, JETP Lett. **105**, 375 (2017).

[Ref.1.25] J. Park, T.-Y. Tan, D. T. Adroja, A. Daoud-Aladine, S. Choi, D.-Y. Cho, S.-H. Lee, J. Kim, H. Sim, T. Morioka, H. Nojiri, V. V. Krishnamurthy, P. Manuel, M. R. Lees, S. V. Streltsov, D. I. Khomskii, and J.-G. Park, Sci. Rep. **6**, 25238 (2016).

[Ref.1.26] S. A. J. Kimber, I. I. Mazin, J. Shen, H. O. Jeschke, S. V. Streltsov, D. N. Argyriou, R. Valentí, and D. I. Khomskii, Phys. Rev. B **89**, 081408(R) (2014).

[Ref.1.27] Y. S. Ponosov, E. V Komleva, and S. V Streltsov, Phys. Rev. B **100**, 134310 (2019).

Chapter 2

Experimental Techniques

2.1 Sample synthesis

Starting materials for growing Li_2RuO_3 single crystals were Li_2CO_3 (99.995%, Alfa Aesar) and RuO_2 (99.95%, Alfa Aesar). Both raw compounds are hygroscopic; thus, I carried out the drying process (300°C, 6h) before weighing. Because they quickly evaporate during the crystal growth due to their low vapor pressure, it is hard to use the conventional flux method. The quartz sealing method, which is a usual synthesis technique for such evaporable starting materials, is also not applicable because Li reacts with SiO_2. The Li-reacted quartz is much weaker than the pristine one, so it is easy to break. To overcome these difficulties, I used the separated educts (SE) method with simplification. The SE method is a modified chemical vapor transport (CVT) method [Ref.2. 1]. The (classical) CVT method requires a sealed container, generally made by quartz, with a temperature gradient and the transport agent, which conveys the starting material from the high-temperature zone to the low-temperature region.

In contrast to the classical CVT method, the SE method has more freedom in selecting a material for the container. Moreover, because this method uses H_2O and O_2 as the transport agent, it does not require the quartz sealing for the controlled environment. Figure 2.1 shows the SE method conducted by F. Freund [Ref.2. 1]. In my case, the two starting materials were just stacked in an alumina crucible without the complicated construction, and the Li_2RuO_3 single crystals were grown at the interface between the two raw materials. I ground them finely to increase the amount of evaporating flux. I added an 8% excess of Li_2CO_3 to compensate Li deficiency occurred by the difference of vapor pressure between the two materials. The prepared materials were baked at 1100°C for 24 hours. Figure 2.2 shows the simplified SE method I used and the grown Li_2RuO_3 single crystals. As shown in Figure 2.2a, the Li_2CO_3 layer was placed above the RuO_2 layer. No single crystal was produced with the inverse order stacking.

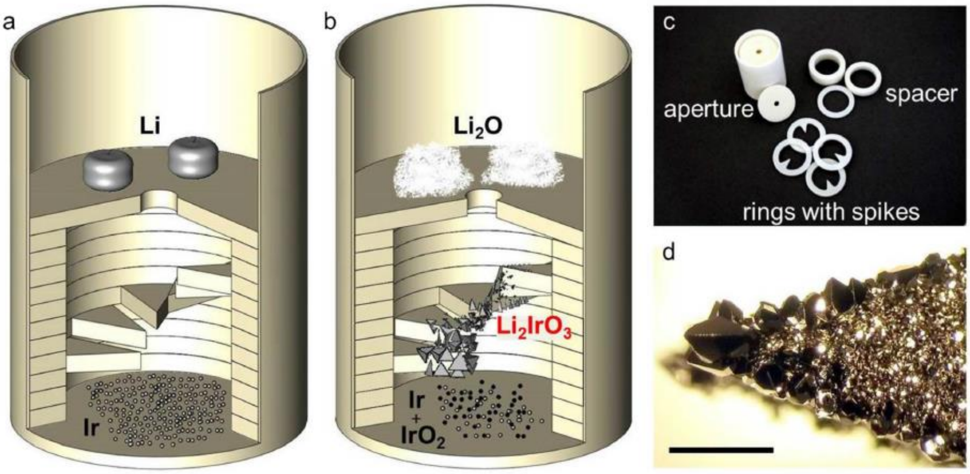

Figure 2.1 Crystal growth equipment by F. Freund (crucible diameter 1.6mm). Arrangement of the materials before and after the growth process is in (a,b), respectively. The rings with spikes set like a spiral staircase to nucleate the vapor at different positions with less intergrowth of the crystals. Formation of the most massive α-Li_2IrO_3 single crystals appears on spikes located ~ 4 mm above the Ir starting materials. (c) Individual parts made from Al_2O_3 and (d) typical appearance of the tips covered with α-Li_2IrO_3 crystals at the bottom side, scale bar 1mm. [Ref.2. 1]

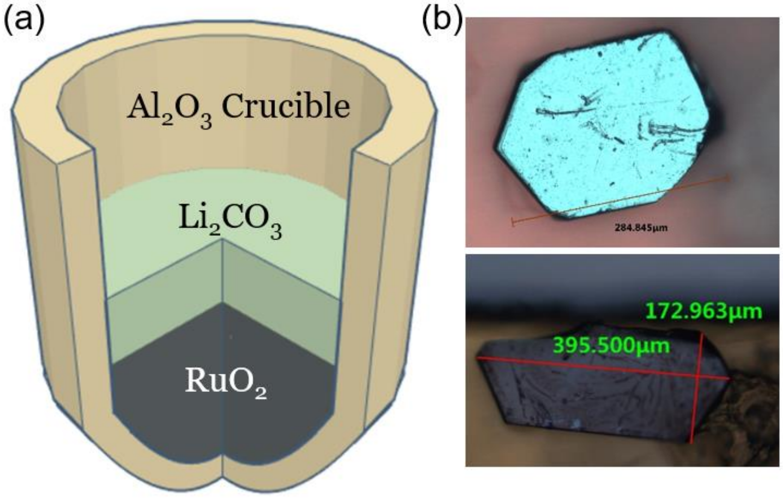

Figure 2.2 (a) The cross-section of the simplified SE method. The Li_2CO_3 layer places above the RuO_2 layer. Li_2RuO_3 single crystals form at the interface of the two layers. (b) typical appearances of the crystals grown by the simplified SE method.

2.2 Resonant Elastic X-ray Scattering (REXS)

Translational symmetry and its breaking is the most crucial concept in solid-state physics [Ref.2. 2]. Because of an enormous number of particles in the solid, it is impossible to consider a motion of particles one by one. The discrete translational symmetry, which is the pattern of particle configuration of solid, gives a framework for handling lots of objects by bundling them up: the densely packed atoms can be considered as a repeating pattern of a unit-cell. X-ray diffraction (XRD), which is the cornerstone of condensed matter physics, is a primary tool for detecting the repeating patterns [Ref.2. 3]. Although this method is old, it is still fundamental and vital for exploring the world of the solid. The X-ray beams scattered by an array of atoms give constructive interference, and one can discover its periodicity, i.e., the symmetry of the system by counting backward the phase difference. When the symmetry is broken, a new interference pattern emerges with supplementary information about the original symmetry.

Although it is, in principle, possible to detect any periodicity of the solid by XRD, it is sometimes subtle to be observed. Especially when the broken symmetry is related to the degrees of freedom of valence electrons, it is difficult to measure because of the too-small intensity of the emerging peaks. Resonant elastic X-ray scattering (REXS), also known as resonant X-ray diffraction, is a modified XRD technique using specific energy of incident photons [Ref.2. 4]. The scattering amplitude is enhanced drastically by the resonant process, which includes the excitation and decay of the core-electron state. It allows us to study degrees of freedom such as charge, spin, and orbital, which has only a tiny signal in the conventional XRD [Ref.2. 5]. Besides, REXS can measure not only the spatial modulation of those degrees of freedom but also the local detail of valence electrons: X-ray absorption spectroscopy, which is another root of the REXS, is a specialized tool for observing the local environment of the electrons [Ref.2. 6].

In this section, I review how REXS works, based on previous studies of Blume, Dmitrienko, Altarelli, and Di Matteo's [Ref.2. 6–9]. First, I describe how photons of X-ray interact with matter. The Dirac equation, a relativistic wave equation, is required to understand the interaction between the spin of electrons and light. Thus, I start from the Dirac equation and progress to the non-relativistic limit. Second, I discuss the X-ray scattering cross-section, restricted to the elastic scattering process. In the elastic process, the state of electrons remains the same after the scattering event. There are three types of elastic scattering: Thomson scattering, non-resonant magnetic scattering, and resonant elastic scattering. I account briefly for them and compare the resonant scattering to the non-resonant scattering process. Finally, I explain the condition for REXS and how to extract the local information of electrons.

2.2.1 Electronic matter-radiation interaction Hamiltonian

Electromagnetic radiation, which is the propagating electromagnetic field through space, perturbs bound electrons in solids. By investigating the behavior of electrons under the perturbation, one can obtain plenty of information about the electronic system. This part aims to derive the interaction Hamiltonian of the radiation and electrons in solids. I first start from the Dirac equation and bring it into a low-energy limit with the Foldy-Wouthuysen transformation [Ref.2. 10].

The Dirac Hamiltonian, H_D, is given as

$$H_D = \sum_{j=1}^{N} \beta mc^2 + V(\vec{r}_j) + c\vec{\alpha} \cdot (\vec{p}_j - \frac{e}{c}\vec{A}(\vec{r}_j, t)) \ ,$$

where $V(r)$ is the scalar potential and $\vec{A}(\vec{r}, t)$ is the vector potential. This Hamiltonian is represented by a 4×4 matrix, determined by β and $\vec{\alpha}$ matrices in standard notation,

$$\beta = \begin{pmatrix} 1 & 0 \\ 0 & 1 \end{pmatrix}, \qquad \vec{\alpha} = \begin{pmatrix} 0 & \vec{\sigma} \\ \vec{\sigma} & 0 \end{pmatrix} \ .$$

Here, 1 is the 2×2 identity matrix and $\vec{\sigma}$ is the vector, consisting of the three Pauli matrices σ_x, σ_y and σ_z. The absorption edges of interest in REXS is in the range of 0.2–20 keV, much lower than the rest energy of the electrons (mc^2 ~ 511 keV). It allows us to focus on the low-energy limit of H_D, rewritten with Foldy-Wouthuysen transformation,

$$H_D \cong H_{FW} = \sum_{j=1}^{N} \left[\frac{\left(\vec{p}_j - \frac{e}{c}\vec{A}(\vec{r}_j, t)\right)^2}{2m} - \frac{\vec{p}_j^{\,4}}{8m^3c^2} + V(\vec{r}_j) - \left(\frac{e}{mc}\right)\vec{s}_j \cdot \vec{B} - \left(\frac{e}{2m^2c^2}\right)\vec{s}_j \right.$$

$$\left. \cdot \left(\vec{E} \times \left(\vec{p}_j - \frac{e}{c}\vec{A}(\vec{r}_i, t)\right)\right) + \left(\frac{e\hbar^2}{8m^2c^2}\right)\nabla \cdot \vec{E} \ \right] \ .$$

The first term is the usual modification of the kinetic energy in the presence of a field. The second is a relativistic correction to the kinetic energy, but it does not involve the field; thus, it is irrelevant to my discussion. The third term is the potential energy of the electron, and the fourth term is the interaction of the electronic spin $\vec{s} = \frac{\hbar}{2}\vec{\sigma}$, where the $\hbar$ is the reduced Planck constant. The fifth term is the term of the spin-orbit interaction with kinetic energy modification. And the last term is the Darwin correction, which vanishes due to the transversal nature of the electromagnetic wave ($\nabla \cdot \vec{E} = \vec{k} \cdot \vec{E} = 0$).

An arbitrary space- and time-dependent vector potential can be described with plane-wave basis distinguished by a wave-vector k and two polarization modes labeled by λ,

$$\vec{A}(\vec{r},t) = \sum_{\vec{k},\lambda} \left(\frac{hc^2}{\Omega\omega_{\vec{k}}}\right)^{\frac{1}{2}} \left[\vec{e}_\lambda a_{\vec{k},\lambda} e^{i\left(\vec{k}\cdot\vec{r}-\omega_{\vec{k}}t\right)} + \vec{e}_\lambda^{*} a_{\vec{k},\lambda}^{\dagger} e^{-i\left(\vec{k}\cdot\vec{r}-\omega_{\vec{k}}t\right)}\right] ,$$

where Ω is the box volume for quantization and does not have any physical meaning in this discussion. $\omega_{\vec{k}}$ is the angular frequency of light, $c|\vec{k}|$. $\vec{e}_\lambda$ is the polarization vector of the photon with the λ-polarization, which is orthogonal to the $\vec{k}$. $a_{\vec{k},\lambda}$ ($a_{\vec{k},\lambda}^{\dagger}$) is the annihilation (creation) operator of the photon with a quantum number ($\vec{k},\lambda$). In this formalism, the Hamiltonian of the photon system is

$$H_{rad} = \sum_{\vec{k},\lambda} \hbar\omega_{\vec{k}} \left(a_{\vec{k},\lambda}^{\dagger} a_{\vec{k},\lambda} + \frac{1}{2}\right)$$

Thus the Hamiltonian for the system of electrons and the radiation field is written as

$$\begin{aligned} H &= H_{FW} + H_{rad} \\ &= \sum_{j=1}^{N} \left[\frac{\left(\vec{p}_j - \frac{e}{c}\vec{A}(\vec{r}_j,t)\right)^2}{2m} + V(\vec{r}_j) - \left(\frac{e}{mc}\right)\vec{s}_j \cdot \vec{B}(\vec{r}_j) \right. \\ &\qquad \left. - \left(\frac{e}{2m^2c^2}\right)\vec{s}_j \cdot \left(\vec{E} \times \left(\vec{p}_i - \frac{e}{c}\vec{A}(\vec{r}_j,t)\right)\right) \right] \\ &\quad + \sum_{\vec{k},\lambda} \hbar\omega_{\vec{k}} \left(a_{\vec{k},\lambda}^{\dagger} a_{\vec{k},\lambda} + \frac{1}{2}\right) . \end{aligned}$$

This Hamiltonian can be separated into three terms, H_{el}, H_{rad}, and H_{int}:

$$H = H_{el} + H_{rad} + H_{int}$$

$$H_{el} = \sum_{j=1}^{N} \left[\frac{\vec{p}_j^2}{2m} + V(\vec{r}_j) + \left(\frac{e}{2m^2c^2}\right)\vec{s}_j \cdot \left(\nabla V(\vec{r}_j) \times \vec{p}_j\right)\right]$$

$$H_{\mathrm{rad}} = \sum_{\vec{k},\lambda} \hbar\omega_{\vec{k}} \left(a_{\vec{k},\lambda}^{\dagger} a_{\vec{k},\lambda} + \frac{1}{2}\right)$$

$$H_{int} = \sum_{j=1}^{N} \left[\left(\frac{e^2}{2mc^2}\right) \vec{A}^2 - \left(\frac{e^2}{2m^2c^4}\right) \vec{s}_j \cdot \left(\frac{\partial \vec{A}}{\partial t} \times \vec{A}\right) - \left(\frac{e}{mc}\right) \vec{A} \cdot \vec{p}_j - \left(\frac{e}{mc}\right) \vec{s}_j \cdot \nabla \times \vec{A} \right],$$

where $\vec{E} = -\nabla V(\vec{r}_j) - \frac{\partial \vec{A}}{\partial t}(\vec{r}_j, t)$ and $\vec{B}(\vec{r}_j) = \nabla \times \vec{A}(\vec{r}_j, t)$. The H_{el} and H_{rad} describe behaviors of non-interacting electron and the radiation field, respectively. The interaction Hamiltonian, H_{int}, contains all terms related to the vector field. It has four terms, named H_1, H_2, H_3, and H_4, respectively.

$$H_1 = \sum_{j=1}^{N} \left(\frac{e^2}{2mc^2}\right) \vec{A}^2(\vec{r}_j, t), \qquad H_2 = -\sum_{j=1}^{N} \left(\frac{e^2}{2m^2c^4}\right) \vec{s}_j \cdot \left(\frac{\partial \vec{A}(\vec{r}_j)}{\partial t} \times \vec{A}(\vec{r}_j, t)\right)$$

$$H_3 = -\sum_{j=1}^{N} \left(\frac{e}{mc}\right) \vec{A}(\vec{r}_j, t) \cdot \vec{p}_j, \qquad H_4 = -\sum_{j=1}^{N} \left(\frac{e}{mc}\right) \vec{s}_j \cdot \nabla \times \vec{A}(\vec{r}_j, t) \ .$$

The first two terms are quadratic in the vector potential. The vector potential is associated with the absorption (annihilation, $a_{\vec{k},\lambda}$) or the emission (creation, $a^{\dagger}_{\vec{k},\lambda}$) of a photon; therefore, the product of the vector potential represents a continuous process of absorption-emission of a photon. The first term, H_1, describes Thomson scattering, the elastic scattering of electromagnetic radiation by a free-charged particle in classical electromagnetism. The second term, H_2, describes non-resonant magnetic scattering, and it is linear in the spin magnetic moment of the electron. The last two terms are for resonant scattering, linear in the vector potential.

2.2.2 Scattering cross-section (Elastic scattering)

In this part, I derive only the elastic scattering process, in which the system stays in the same state before and after the scattering event. This process conserves the energy of the scattered photon. When the incoming photon has a polarization vector $\vec{e}_\lambda$ and wave-vector $\vec{k}$, and the outgoing photon has a polarization vector $\vec{e}'_{\lambda'}$ and wave-vector $\vec{k}'$, the conservation laws implies $|\vec{k}| = |\vec{k}'|$, and the initial and final state of the total system are:

$$|i\rangle = \left|0; \cdots, (\vec{e}_\lambda, \vec{k}), \cdots\right\rangle \ ,$$
$$|f\rangle = \left|0; \cdots, (\vec{e}'_{\lambda'}, \vec{k}'), \cdots\right\rangle \ .$$

The notation ‘0’ labels the ground state of the electronic system, and $(\vec{e}_\lambda, \vec{k})$ and $(\vec{e}'_{\lambda'}, \vec{k}')$ represent the state of the incoming- and outgoing-photon, respectively. It is clear that $\langle f | a_{\vec{k},\lambda} | i \rangle$

and $\left\langle f \middle| a^{\dagger}_{\vec{k},\lambda} \middle| i \right\rangle$ are zero, thus $\langle f|\vec{A}|i\rangle$ is zero because the vector potential is a linear combination of the annihilation and the creation operators. It implies that the lowest-order contribution of the vector potential comes from second-order perturbation theory, and the H_3 and H_4 should be addressed in this way because they are first-order in the vector potential. The following expression gives the total scattering intensity:

$$
\begin{aligned}
I(\omega_k) = {} & \left|F(\vec{Q})\right|^2 \left|S(\vec{Q})\right|^2 \\
& \propto \left| \sum_{a}^{u.c} e^{\mathrm{i}(\vec{k}'-\vec{k})\cdot\vec{R}_a} \left(\langle f|H_1 + H_2|i\rangle \right.\right. \\
& \left.\left. + \sum_{n} \frac{\langle f|H_3 + H_4|n\rangle\langle n|H_3 + H_4|i\rangle}{\hbar\omega_k + E_0 - E_n} \right)_a \right|^2 \left| \sum_{N} e^{\mathrm{i}(\vec{k}'-\vec{k})\cdot\vec{R}_{hkl}} \right|^2 ,
\end{aligned}
$$

where $\vec{Q} = \vec{k}' - \vec{k}$ is the scattering vector, F(Q) is the structure factor of the unit cell, and S(Q) is the form factor. $|n\rangle$ is an intermediate state during the resonant process.

Thomson scattering term *H*₁

The calculation result of the Thomson scattering term H_1 is given by

$$
\begin{aligned}
\langle f|H_1|i\rangle = {} & \frac{hc^2}{\Omega\omega_{\vec{k}}}\frac{e^2}{mc^2}\sum_{i}\left\langle 0;\left(\vec{e}'_{\lambda'},\vec{k}'\right)\middle|\left(\vec{e}'_{\lambda'}\cdot\vec{e}_{\lambda}\right)a^{\dagger}_{\vec{k}',\lambda'}a_{\vec{k},\lambda}e^{i(\vec{k}-\vec{k}')\cdot\vec{r}_i}\middle|0;\left(\vec{e}_{\lambda},\vec{k}\right)\right\rangle \\
& = \frac{hc^2}{\Omega\omega_{\vec{k}}} r_0\left(\vec{e}'_{\lambda'}\cdot\vec{e}_{\lambda}\right)\sum_{i}\left\langle 0\middle|e^{i\vec{Q}\cdot\vec{r}_i}\middle|0\right\rangle \equiv \frac{hc^2}{\Omega\omega_{\vec{k}}} r_0\left(\vec{e}'_{\lambda'}\cdot\vec{e}_{\lambda}\right) f_0(\vec{Q}) \ .
\end{aligned}
$$

The magnitude of electron scattering is controlled by the quantity $r_0 \equiv e^2/mc^2$, called the Thomson radius, $r_0 = 2.818\times10^{-15}$ m. The polarization dependency $\left(\vec{e}'_{\lambda'}\cdot\vec{e}_{\lambda}\right)$ shows that this process does not change the polarization of the scattered photon. $f_0(\vec{Q}) = \sum_i \left\langle 0\middle|e^{i\vec{Q}\cdot\vec{r}_i}\middle|0\right\rangle$ is the atomic scattering factor considered in the case of the normal (or routinely happening in our lab) X-ray diffraction.

Non-resonant magnetic scattering term *H*₂

The cross product of the vector potential and its time derivative is given by

$$\frac{\partial\vec{A}}{\partial t}\times\vec{A}=\frac{hc^2}{\Omega\omega_{\vec{k}}}\left[-\mathrm{i}\omega_{\vec{k}}\left\{\vec{e}_\lambda a_{\vec{k},\lambda}e^{\mathrm{i}\left(\vec{k}\cdot\vec{r}_j-\omega_{\vec{k}}t\right)}-\vec{e}_\lambda^{\,*}a_{\vec{k},\lambda}^{\dagger}e^{-\mathrm{i}\left(\vec{k}\cdot\vec{r}_j-\omega_{\vec{k}}t\right)}\right\}\right]$$
$$\times\left[\vec{e}_\lambda a_{\vec{k}',\lambda'}e^{\mathrm{i}\left(\vec{k}'\cdot\vec{r}_j-\omega_{\vec{k}'}t\right)}+\vec{e}_{\lambda'}^{\,*}a_{\vec{k}',\lambda'}^{\dagger}e^{-\mathrm{i}\left(\vec{k}'\cdot\vec{r}_j-\omega_{\vec{k}'}t\right)}\right].$$

The matrix element of the non-resonant magnetic scattering term is given by

$$\langle f|H_2'|i\rangle=-\mathrm{i}r_0\left(\frac{hc^2}{\Omega\omega_{\vec{k}}}\right)\left(\frac{\omega_{\vec{k}}}{mc^2}\right)\sum_i\left\langle 0\middle|\vec{s}_i\cdot\left(\vec{e}_{\lambda'}^{\,\prime}\times\vec{e}_\lambda\right)e^{i(\vec{k}-\vec{k}')\cdot\vec{r}_i}\middle|0\right\rangle\ .$$

It contains the spin operator, and its magnitude is reduced by the factor $\left(\frac{\omega_{\vec{k}}}{mc^2}\right)$; it is a small number because the typical energy of the X-ray is of the order of 10 keV while the rest energy of the electron is 511 keV. The polarization dependency $\left(\vec{e}_{\lambda'}^{\,\prime}\times\vec{e}_\lambda\right)$ shows that the polarization direction of the incident photon changes in this scattering process.

Resonant scattering terms *H*₃ & *H*₄

The partial matrix element of the resonant scattering part is given by

$$\langle n|H_3+H_4|i\rangle=\left(\frac{hc^2}{\Omega\omega_{\vec{k}}}\right)^{\frac{1}{2}}\frac{e}{mc}\ \left\langle n\middle|\vec{e}_\lambda\cdot\vec{J}(\vec{k})a_{\vec{k},\lambda}+\vec{e}_\lambda^{\,*}\cdot\vec{J}^{\dagger}(\vec{k})a_{\vec{k},\lambda}^{\dagger}\middle|i\right\rangle\ ,$$

where the current operator is $\vec{J}(\vec{k})=\sum_j(\vec{p}_j-\mathrm{i}\vec{k}\times\vec{s}_j)e^{i\vec{k}\cdot\vec{r}_j}$. There are two kinds of processes in the resonant term. The first process is that the incoming photon is annihilated first; afterward, the outgoing photon is created. In this case, the core-hole lifetime (Γ) has to be considered; its value is usually of the order of 1 eV. The second process is that the outgoing photon is created first; afterward, the incoming photon is annihilated. The following expression gives the resonant scattering term with those two processes:

$$\left(\frac{hc^2}{\Omega\omega_{\vec{k}}}\right)\frac{r_0}{m}\sum_n\frac{E_0-E_n}{\hbar\omega_k}\left[\frac{\vec{e}_\lambda^{\,*}\cdot\langle 0|\vec{J}^{\dagger}(\vec{k})|n\rangle\langle n|\vec{J}(\vec{k})|0\rangle\cdot\vec{e}_\lambda}{E_0+\hbar\omega_k-E_n+\mathrm{i}\Gamma_\mathrm{n}/2}-\frac{\vec{e}_\lambda\cdot\langle 0|\vec{J}(\vec{k})|n\rangle\langle n|\vec{J}^{\dagger}(\vec{k})|0\rangle\cdot\vec{e}_\lambda^{\,*}}{E_0-E_n-\hbar\omega_k}\right]\ .$$

The factor $\frac{E_0-E_n}{\hbar\omega_k}$ comes from the pole analysis of two resonant terms. The last term has no contribution to the scattering cross-section because only the excited state with higher energy is in consideration.

The plane wave component in the current operator $\vec{J}(\vec{k})=\sum_j(\vec{p}_j-\mathrm{i}\vec{k}\times\vec{s}_j)e^{i\vec{k}\cdot\vec{r}_j}$ can be expressed with a series of expansion. A multipole expansion based on spherical harmonics (Bessel function for the radial part and Legendre polynomials for the angular part) is generally used. Here I used the Taylor expansion.

$$\vec{p}_j e^{i\vec{k}\cdot\vec{r}_j} = \vec{p}_j\left(1 + \mathrm{i}\vec{k}\cdot\vec{r}_j - \frac{1}{2}\left(\vec{k}\cdot\vec{r}_j\right)^2 + \cdots\right) = \sum_{\hbar} O_{j,h}\left(\vec{k}\right)$$

$$\left(\vec{s}_j\times\vec{k}\right)e^{i\vec{k}\cdot\vec{r}_j} = \left(\vec{s}_j\times\vec{k}\right)\left(1 + i\vec{k}\cdot\vec{r}_j - \frac{1}{2}\left(\vec{k}\cdot\vec{r}_j\right)^2 + \cdots\right) = \sum_{\hbar} O'_{j,h}\left(\vec{k}\right)$$

The first term in $O_{j,h}\left(\vec{k}\right)$ (electric dipole, E1) is calculated as

$$O^{E1}_{n0}\left(\vec{k},\lambda\right) = \sum_j \langle n|O_{j,1}\left(\vec{k}\right)|0\rangle = \sum_j \langle n|\vec{p}_j|0\rangle = \sum_j \left\langle n\left|\frac{m}{\mathrm{i}\hbar}\left[\vec{r}_j, H_{el}\right]\right|0\right\rangle = \mathrm{i}m\omega_{n0}\langle n|\vec{R}|0\rangle,$$

where the third equality is obtained through the Heisenberg equation of motion, and $\omega_{no} \equiv \frac{E_n - E_0}{\hbar}$, $\vec{R} \equiv \sum_j \vec{r}_j$. The higher-order terms also can be calculated from the commutator. For example, the term in $k\cdot r$ can be derived as

$$\frac{m}{2\hbar}[xy, H_{el}] = \frac{1}{2}\left(p_x y + x p_y\right) = \mathrm{i}p_x\mathrm{y} + \frac{1}{2}l_z \ .$$

Thus the second term $O_{j,2}\left(\vec{k}\right)$ is calculated as

$$\mathrm{i}\vec{p}_j\left(\vec{k}\cdot\vec{r}_j\right) = \frac{m}{2\hbar}\left[\vec{r}_j\left(\vec{k}\cdot\vec{r}_j\right), H_{el}\right] + \frac{\mathrm{i}}{2}\left(\vec{l}_j\times\vec{k}\right) \ .$$

The first term of this expression gives the electric quadrupole (E2) contribution:

$$O^{E2}_{n0}\left(\vec{k},\lambda\right) = -\frac{m\omega_{n0}}{2}\langle n|\textstyle\sum_j \vec{r}_j\left(\vec{k}\cdot\vec{r}_j\right)|0\rangle \ .$$

The second term $\frac{\mathrm{i}}{2}\left(\vec{l}_j\times\vec{k}\right)$ depends on the orbital moment; thus, it is magnetic. It can be grouped with the first term of the $O'_{j,h}\left(\vec{k}\right)$. The two terms form the magnetic dipole (M1):

$$\begin{aligned} O^{M1}_{n0}\left(\vec{k},\lambda\right) &= \sum_j \left[\mathrm{i}\langle n|\left(\vec{s}_j\times\vec{k}\right)|0\rangle + \frac{\mathrm{i}}{2}\langle n|\left(\vec{l}_j\times\vec{k}\right)|0\rangle\right] \\ &= \frac{\mathrm{i}}{2}\langle n|\left(\textstyle\sum_j \vec{l}_j + 2\vec{s}_j\right)\times\vec{k}|0\rangle = \frac{\mathrm{i}}{2}\langle n|\vec{M}\times\vec{k}|0\rangle \ , \end{aligned}$$

where $\vec{M} = \sum_j \vec{l}_j + 2\vec{s}_j$ is the total magnetic dipole moment of the atomic electrons.

Non-symmorphic symmetry of crystals

Because the resonant scattering is a second-order process, the scattering amplitude is much smaller than the first-order scattering events, such as the Thomson scattering. Therefore, to resolve the resonant scattering, I had to select the Bragg forbidden reflection in the reciprocal lattice. The condition for the forbidden reflection is given by

$$\sum_{a}^{\text{unit cell}} e^{\mathrm{i}\vec{Q}\cdot\vec{R}_a} f_{0,a}(\vec{Q}) = 0,$$

where $f_{0,a}(\vec{Q})$ is an atomic scattering factor of the atom at $\vec{R}_a$. These conditions were calculated and listed in International Tables for Crystallography Vol. A [Ref.2. 11]. They are determined by the phase differences between the scattering amplitudes of symmetry-equivalent atom positions in the unit cell (Wyckoff positions), and those differences depend on the space group and the occupied atomic sites.

Non-symmorphic symmetry operations involve translations with fractional lattice parameters. There are two kinds of non-symmorphic operations: glide plane and screw operation, as shown in Figure 2.3 for crystal systems.

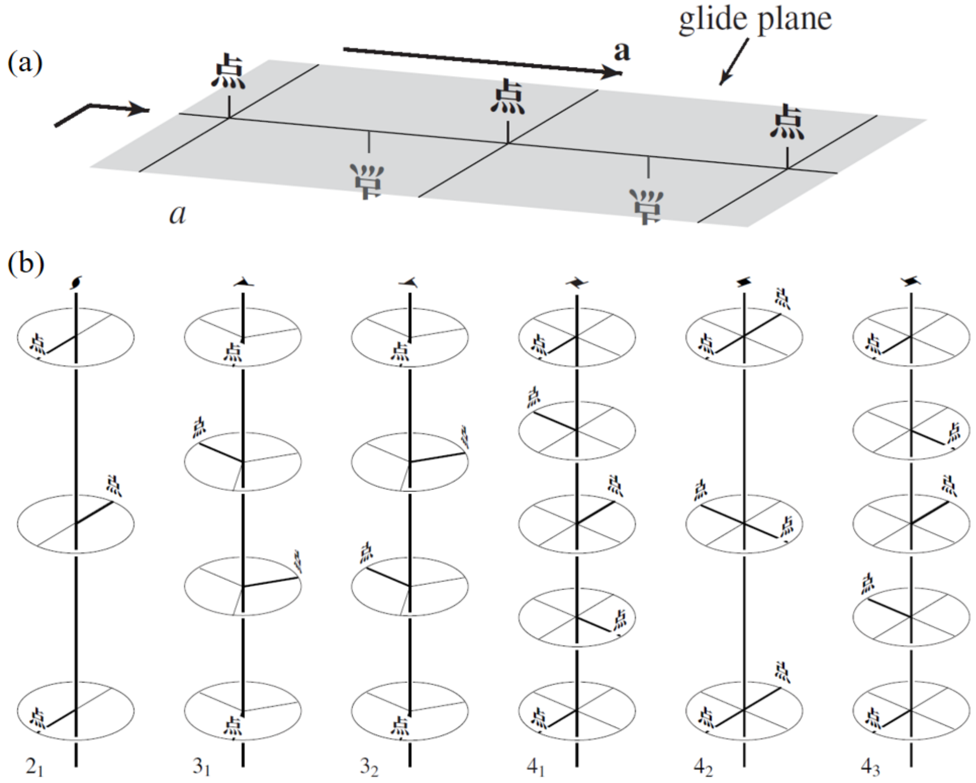

Figure 2.3 Non-symmorphic symmetry operations: (a) Glide plane: a reflection followed by a translation parallel with the reflection plane. (b) Screw operation: a rotation followed by a translation along the rotational axis [Ref.2. 12]**.**

When the space group of the crystal includes such non-symmorphic symmetry operations, specific reflections are extinct. The scattered photons related to the Thomson process interfere destructively. For example, there is no intensity at (010) reflection with space group $P2_1/m$ because of the screw axis 2_1 parallel to the crystallographic *b*-axis. On the other hand, the scattered photons through the resonant process can change its polarization and interfere constructively with the photon scattered from the other unit cell. Thus, at particular reflection positions corresponding to the nonsymmorphic operations, it is possible to observe the purely resonant reflection.

For example, if I consider only the resonant process with the electric dipole (E1), the structure factor is given by

$$F^{E1-E1}(\vec{Q}) \propto \sum_{a}^{u.c} e^{\mathrm{i}\vec{Q}\cdot\vec{R}_a} \left(\sum_{n} \frac{\omega_{n0}^{3}}{\omega_k} \frac{\vec{e}_{\lambda'}^{\,\prime *} \cdot \langle 0|\vec{R}|n\rangle\langle n|\vec{R}|0\rangle \cdot \vec{e}_{\lambda}}{\omega_k - \omega_{n0} + \frac{\mathrm{i}\Gamma_n}{2\hbar}} \right)_a$$

$$= \vec{e}_{\lambda'}^{\,\prime *} \cdot \left(\sum_{a}^{u.c} e^{\mathrm{i}\vec{Q}\cdot\vec{R}_a} f_a^{E1-E1} \right) \cdot \vec{e}_{\lambda} \ ,$$

where the f_a^{E1-E1}, called a tensorial atomic scattering factor, has a second-rank tensor form. The structure factor can be described briefly by Jone's matrix, which is a matrix representation for each scattering channel of respective polarization of light [Ref.2. 13]. For a linearly polarized electromagnetic wave, each element of the matrix is described as

$$\hat{\boldsymbol{\epsilon}}' \cdot F(Q) \cdot \hat{\boldsymbol{\epsilon}} = \begin{pmatrix} \epsilon_{\sigma'} \cdot F(Q) \cdot \epsilon_{\sigma} & \epsilon_{\sigma'} \cdot F(Q) \cdot \epsilon_{\pi} \\ \epsilon_{\pi'} \cdot F(Q) \cdot \epsilon_{\sigma} & \epsilon_{\pi'} \cdot F(Q) \cdot \epsilon_{\pi} \end{pmatrix} ,$$

where the $\hat{\epsilon}$ and $\hat{\epsilon}'$ represent the polarization directions of the incident and scattered light, respectively. The σ (π) expresses the polarization perpendicular to (lying in) the scattering plane, which is the plane defined by the incident and outgoing wave vectors. It is possible to extract several factors of the scattering factor by the polarization analysis. Notably, changing the orientation of the scattering plane by rotating the sample provides rich information about local and global symmetries of the scattering center: it is the primary purpose of REXS.

I carried out the REXS experiment on Li_2RuO_3 at the I16 beamline in Diamond Light Source (U. K.) [Ref.2. 14]. I will show the experimental details in chapter 4.

References

[Ref.2.1] F. Freund, S. C. Williams, R. D. Johnson, R. Coldea, P. Gegenwart, and A. Jesche, Sci. Rep. **6**, 35362 (2016).

[Ref.2.2] A. M. Glazer and G. Burns, *Space Groups for Solid State Scientists* (Academic Pr, 2013).

[Ref.2.3] W. H. Bragg, Nature **91**, 477 (1913).

[Ref.2.4] S. W. Lovesey, E. Balcar, K. S. Knight, and J. Fernández Rodríguez, Phys. Rep. **411**, 233 (2005).

[Ref.2.5] J. Fink, E. Schierle, E. Weschke, and J. Geck, Reports Prog. Phys. **76**, 056502 (2013).

[Ref.2.6] V. E. Dmitrienko, K. Ishida, A. Kirfel, and E. N. Ovchinnikova, Acta Crystallogr. Sect. A Found. Crystallogr. **61**, 481 (2005).

[Ref.2.7] S. Di Matteo, J. Phys. D. Appl. Phys. **45**, 163001 (2012).

[Ref.2.8] G. Materlik and C. J. Sparks, *Resonant Anomalous X-Ray Scattering: Theory and Applications* (North-Holland, 1994).

[Ref.2.9] E. Beaurepaire, *Magnetism : A Synchrotron Radiation Approach* (Springer, 2006).

[Ref.2.10] L. L. Foldy and S. A. Wouthuysen, Phys. Rev. **78**, 29 (1950).

[Ref.2.11] T. Hahn, *International Tables for Crystallography* (International Union of Crystallography, Chester, England, 2006).

[Ref.2.12] U. Müller, H. Wondratschek, and Bärnighausen. Hartmut., *Symmetry Relationships between Crystal Structures : Applications of Crystallographic Group Theory in Crystal Chemistry* (Oxford University Press, 2017).

[Ref.2.13] G. R. Fowles, *Introduction to Modern Optics* (Dover Publications, 1989).

[Ref.2.14] S. P. Collins, A. Bombardi, A. R. Marshall, J. H. Williams, G. Barlow, A. G. Day, M. R. Pearson, R. J. Woolliscroft, R. D. Walton, G. Beutier, and G. Nisbet, AIP Conf. Proc. **1234**, 303 (2010).

Chapter 3

Anisotropy and transition metal dimer in Li_2RuO_3

The formation of the transition metal clusters makes the system irregular because that structural transition accompanies the breaking of the symmetry elements in the space group [Ref.3. 1,2]. The nonuniformity in the lattice induces an anisotropy in several physical properties, e.g., structural deformation, magnetic susceptibility, and resistivity. Thus it is possible to acquire lots of information about the cluster by measuring such anisotropies. In the Li_2RuO_3 case, because the dimers are lined up in the herringbone-patterned honeycomb lattice, comparing the physical properties along with the a- and b-directions would reveal the directional nature of the dimer.

3.1 Structural Distortion by the dimerization

A_2MO_3 (A = Li or Na, M = transition metal) is a prospective candidate in the search for particular states originating from specific structural, electronic, and magnetic configurations on a honeycomb lattice. Li_2RuO_3, having a honeycomb lattice and 4d t_{2g}^4 electronic configuration, has attracted significant attention on account of the presence of an orbital-selective Peierls transition (OSPT) leading to the strongest inclination toward dimerization among the A_2MO_3 systems [Ref.3. 3]. Most interestingly, the dimerized bonds between Ru atoms display a herringbone pattern with a remarkable difference in length between the short and long bonds alternating along the bond direction, and simultaneously it changes space group from C2/m to $P2_1/m$ [Ref.3. 4]. It should be noted that this bond length disparity is as large as 0.5 Å, which is consistent with the strong direct bonding between two adjacent Ru atoms for the shorter bond. The short bonds in Li_2RuO_3 are even shorter than those in Ru metal. The short bonds present long-range structural order and form a valence bond solid (VBS) with a local spin-singlet state. As such, all particularity of this material lies in structural aspects. Therefore, it is crucial to scrutinize the structural factors to understand this system.

3.1.1 Crystal Structure Analysis

The crystal structure was measured by X-ray diffraction (XRD) using a Rigaku XtalLab P200 (Mo target, averaged K_α) and refined with the WinPLOTER program [Ref.3. 5]. Figure 3.1a displays the refinement result of the XRD data acquired at 300 K. The number of reflections in the data is about 1,700; the refined lattice parameters are a = 4.931 Å, b= 8.795 Å and c= 5.132 Å with a β-angle of 108.22 °. The refined atomic positions in the unit cell are in Table 3.1. The result also shows a noticeable difference in the inter-Ru bond lengths within the Ru honeycomb layers reported in previous findings [Ref.3. 4]. According to the analysis, the shortest Ru–Ru bond (red cylinders in Fig. 3.1b) length (d_S) is 2.571 Å, while those of the other bonds (orange cylinders in Fig. 3.1b) are 3.048 Å (d_l) and 3.058 Å (d_L), where $(d_L - d_S)/d_S$ ~ 0.186: almost identical to the reported value [Ref.3. 4].

Element	Wyckoff Position	x	y	z	B_{iso}	Occupancy
Ru	4f	0.27949	0.07675	0.00411	0.44724	1
Li(1)	4f	0.77008	0.09553	0.50741	1.28114	1
Li(2)	2e	0.77365	0.25	0.00564	0.61161	0.5
Li(3)	2e	0.25235	0.25	0.48588	1.26203	0.5
O(1)	4f	0.00487	0.07762	0.022640	0.70170	1.0
O(2)	4f	0.50272	0.08292	0.74546	0.74520	1.0
O(3)	2e	0.50939	0.25	0.23413	0.81105	0.5
O(4)	2e	0.04510	0.25	0.78186	0.73350	0.5

Table 3.1 The refined atomic positions of Li_2RuO_3 ($P2_1/m$, 300 K)

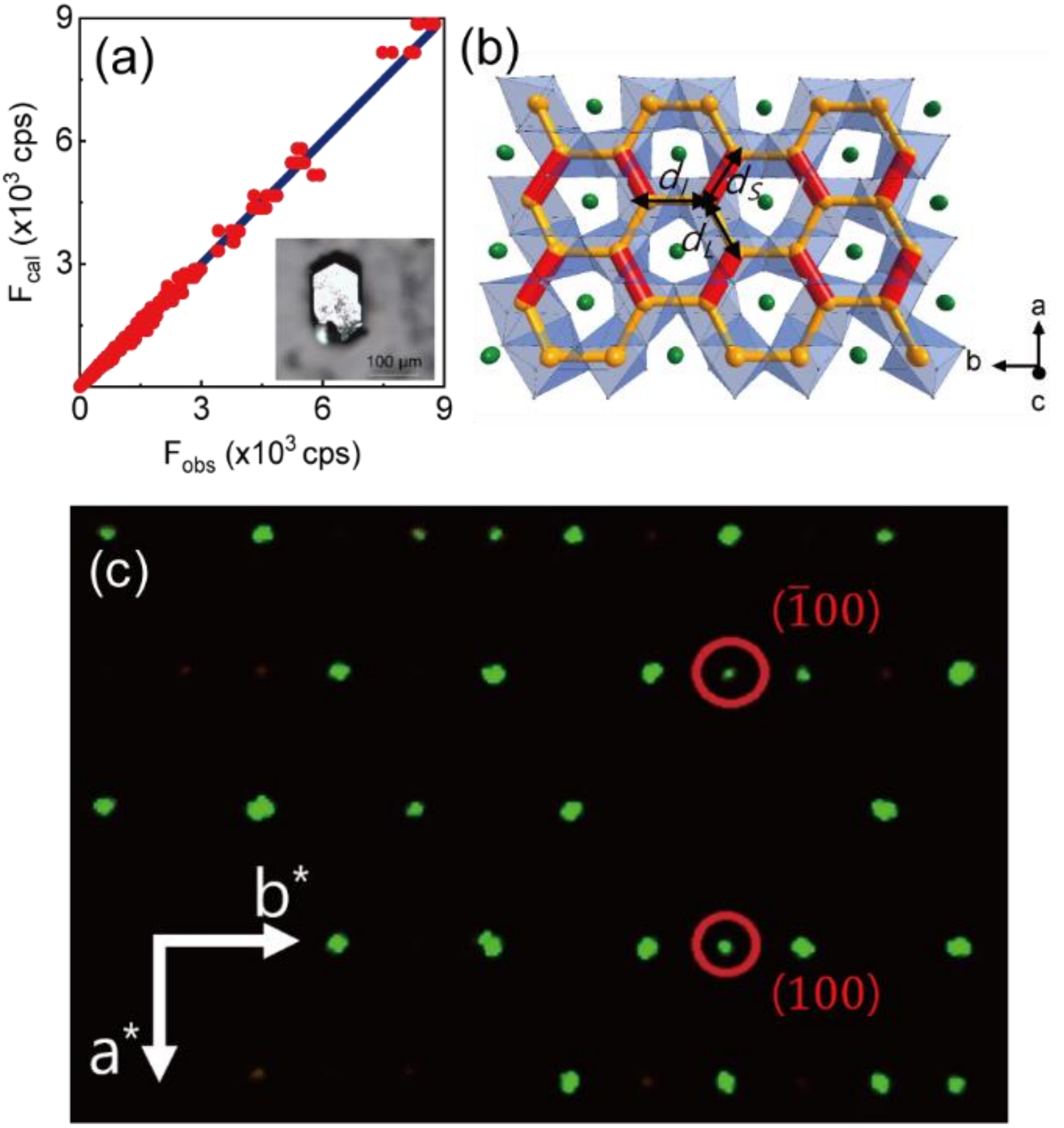

Figure 3.1 (a) Single-crystal refinement results of the Li_2RuO_3 single-crystal. The inset shows a hexagonal Li_2RuO_3 single-crystal. The horizontal (vertical) axis is the observed (calculated) scattering intensity of reflections of the Li_2RuO_3. (b) Li_2RuO_3 at room temperature, viewed along the perpendicular direction to the Ru honeycomb layer in the *ab*-plane. The yellow and green spheres represent, respectively, the Ru and Li-ions. The blue polygons represent oxygen octahedrons. There are two unequal Ru–Ru bonds, i.e., dimerized bonds (red) and two other bonds (yellow) with similar lengths. (c) X-ray diffraction image in the (hk0) plane of single-crystal Li_2RuO_3 with no sign of twinning.

3.1.2 The *b/a* ratio: A parameter of distortion

Figure 3.2a shows the intensity of the (101) reflection as a function of temperature up to 600 K. It vanishes above the transition temperature of ~ 550 K with a structural transition from $P2_1/m$ to C2/m. Figure 3.2b shows the relative ratio of the two lattice parameters *b*/*a* as a function of temperature. We note that this ratio can serve as a quality check of the samples; it is susceptible to the disorder of dimers [Ref.3. 6]. Table 3.2 shows the list of the *b/a* ratios at 300 K reported in previous researches: for our sample, the rate is 1.784. Upon heating, this ratio converges to $\sqrt{3}$ at 600 K with a homogeneous Ru-Ru bond length, and the honeycomb layers become almost regular in the higher temperature range (inset in Fig. 3.2b). Thus, the *b/a* ratio directly measures the lattice distortion by dimerization and serves as a good indicator for the quality of the crystal.

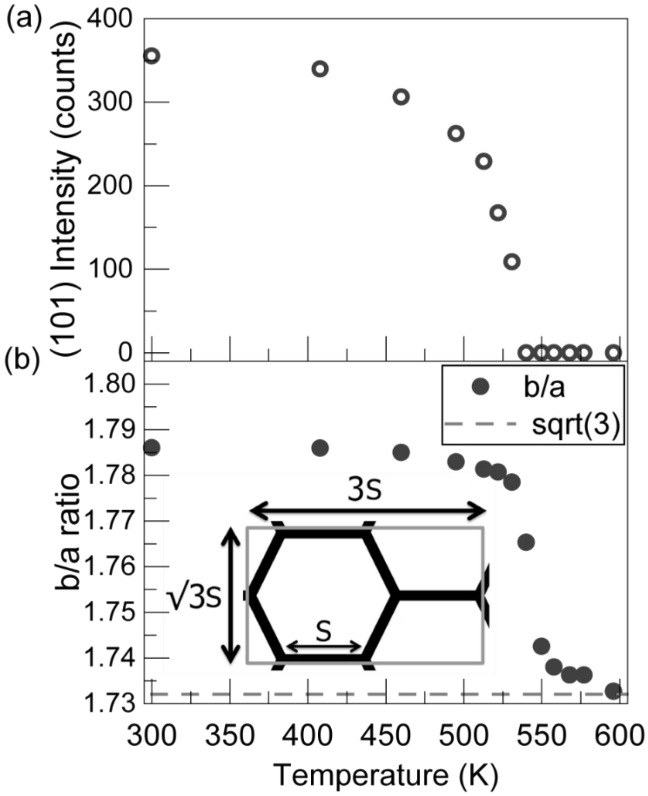

Figure 3.2 Temperature dependence of (a) the intensity of the (101) peak and (b) the *b*/*a* ratio of the lattice parameters. The blue dashed line represents the value of *b*/*a* ~ $\sqrt{3}$, a value found for the honeycomb structure with an almost ideal honeycomb lattice. The inset shows an illustration of the perfect hexagonal honeycomb structure.

	References		b/a	$(b/a-\sqrt{3})/\sqrt{3}$ (%)
Calculation	[Ref.3. 7]	VASP	1.789	3.260
Powder	[Ref.3. 4]	Li_2RuO_3	1.785	3.044
	[Ref.3. 8]	LRO1	1.780	2.779
		LRO2	1.784	2.982
		LRO3	1.780	2.740
		LRO4	1.777	2.581
		LRO5	1.776	2.561
		LRO6	1.767	2.039
	[Ref.3. 6]	A	1.774	2.438
		B	1.771	2.261
		C	1.781	2.836
		D	1.782	2.855
		E	1.782	2.893
		F	1.784	2.975
		G	1.785	3.042
		H	1.785	3.061
	[Ref.3. 9]	Li_2RuO_3	1.781	2.799
		$(Li_{0.95}Na_{0.5})_2RuO_3$	1.778	2.669
	[Ref.3. 10]	Li_2RuO_3	1.785	3.044
Single Crystal	[Ref.3. 10]	Li_2RuO_3(P)	1.766	1.976
		Li_2RuO_3(C)	1.744	0.671
	This work	Li_2RuO_3	1.784	2.977

Table 3.2 Summary of b/a parameter taken after several references.

3.2 Resistivity anisotropy and the dimerization

The resistivities of the principal crystallographic axes were measured with a two-probe method because the sample size is too small for the conventional, more accurate, four-probe method. (Fig. 3.3a). The dimensions of the samples for the electric measurement were as follows: for ρ_a –[w(width)=125 μm, l(length)=151 μm, h(height)=47 μm], ρ_b –[w=249 μm, l=200 μm, h=54 μm], ρ_c –[w=220 μm, l=51 μm, h=221 μm]. The applied voltage between the two electrodes was kept below 0.2 V to prevent any possible electric charging effect that could occur from the high mobility of the Li^+ ions [Ref.3. 11]. We used two different systems for the resistivity measurements to cover a broad temperature range: one with a cryostat for low temperature from 5 to 300 K and another with SiC heaters for high temperature from 300 to 650 K.

I also measured the high-temperature resistivity along the b-axis with a 4-probes method to verify several issues: the effect of contact resistance in the 2-probe measurement, a thermal hysteresis of the resistance, and the identification for the conductance character in the high-temperature phase (Fig 3.3b). The sizes of the sample for the 4-terminal measurement are as follows: w=44.4 μm, l=200 μm, h=32.5 μm.

3.2.1 Resistivity anisotropy of Li_2RuO_3

The resistivity in Fig 3.3c displays distinct anisotropic behavior. The resistivity along the c^*-axis is the largest over the whole temperature range because the LiO layers disjoin the RuO_2 honeycomb layers along this direction. Of particular interest is anisotropy of the in-plane orientation. The measurement shows that the resistivity along the b-axis is larger than the a-axis. This in-plane anisotropy suggests that an electronic hopping between the dimers along the b-axis (d_I in Fig. 3.1b) is smaller than that along the a-axis (d_L and d_S in Fig 3.1b). This ratio ρ_b/ρ_a is found to be ~ 2 above the phase transition. It increases as decreasing temperature and attains around 10 at 5 K. This in-plane electric anisotropy indicates the directional anisotropy of the hopping integrals in the dimer phase, which is most likely to be related to the orbital degrees of freedom of the Ru 4*d* bands.

The temperature-dependence and value of resistivity of the 4-probe result are almost the same as those of the 2-probe result in Fig 3.3d. These data exhibit an explicit thermal hysteresis and insulating behavior in the high-temperature phase.

Arrhenius type plot of the resistivity data is displayed in the inset of Fig 3.3c. For all three crystallographic directions, the curves are well-matched with a straight line with an energy gap of ~ 0.15 eV in the high-temperature phase. However, they do not follow the activation formula in the low-temperature state with the dimerized bonds. To check whether this low-temperature curves could be explained with a theory for topological insulators as suggested for SmB_6 [Ref.3. 12], we have calculated a topology of the bands using the VASP2trace code/program and discovered that all the bands in Li_2RuO_3 are topologically trivial [Ref.3. 13]. Thus, we assume that this low-temperature flattening behavior of the resistivity curves is more likely to be extrinsic, probably due to Li defects in the system.

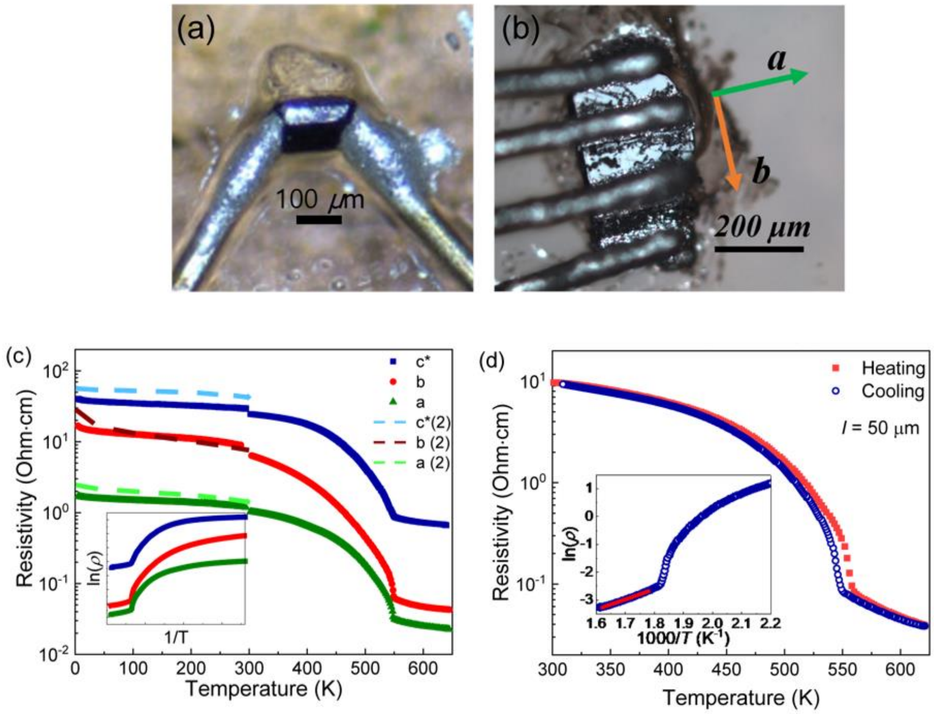

Figure 3.3 The pictures of (a) 2- and (b) 4-probe contact on the single-crystal Li_2RuO_3 (c) Resistivity curves of the Li_2RuO_3 single-crystal in a temperature range of 5–650 K, along the *a*-(green), *b*-(red), and *c-(blue) crystal axes. The dashed lines in the range of 5–300 K are for the data to check the reproducibility of the results with other samples. The inset shows the Arrhenius type plots of the resistivity curves from 300 to 650 K. (d) 4-probe resistivity curves along the b-axis in the range of 300-630 K, with heating (red) and cooling (blue).**

3.2.2 DFT calculation

To understand the anisotropic behavior of resistivity, we carried density functional theory (DFT) calculations using WIEN2k [Ref.3. 14] with 12×6×12 *k*-points in the full Brillouin zone using the Tran-Blaha modified Becke Johnson (TB-mBJ) potential for exchange-correlation [Ref.3. 15,16]. The TB-mBJ potential is known to give a better estimation for an electronic bandgap than the standard functionals such as local density approximation (LDA) or generalized gradient approximation (GGA) functionals, without much computational cost. The spin-orbit coupling effect was included in the calculations (spin-orbit coupling strength of Ru is ~ 75 meV). The resistivity was then computed with a BoltzWann module in Wannier90 to estimate the resistivity anisotropy [Ref.3. 17,18]. The BoltzWann utilizes a semiclassical Boltzmann transport equation to calculate resistivity. It assumes a constant relaxation time approximation and a dispersion relation from the Wannierized tight-binding Hamiltonian. We then guessed the macroscopic magnetic susceptibility from the macroscopic susceptibility outputs provided by the NMR calculation module of WIEN2k [Ref.3. 19,20]. The macroscopic magnetic susceptibility is calculated using the 2nd order perturbation theory on the DFT results by taking modulated external magnetic fields with a long wavelength.

A significant point worth noting here is that when we used the standard potential (GGA or LDA) for the DFT calculation, the bandgap could not be opened. Only when we employed the TB-mBJ potential did we succeed in causing an indirect electronic bandgap of 170 meV: whose value is more or less consistent with the experimental values. This reliance on the bandgap on the potentials employed for the DFT calculations implicitly implies that the Coulomb *U* plays an essential role in realizing the insulating phase, which is involved in the TB-mBJ potential.

With the band structures developing the correct value of the bandgap, we computed both the resistivity and susceptibility results using the modules embedded in the WIEN2k code. According to our calculations done without spin-orbit coupling, we obtained the following values: $\chi_a = 1.83$, $\chi_b = 2.34$, and $\chi_c = 1.21$, all in units of 10^{-4} emu/mol. These calculations not only give the right anisotropy but also give values of the same order of magnitude as experimentally observed. The resistivity calculation with the BoltzWann code was proposed to capture the thermally-excited charge carrier contribution under the constant relaxation time approximation. In this resistivity calculation, we succeeded in getting the right anisotropy of out-of-plane and in-plane resistivity, as one can see in Fig 3.4c.

Interestingly, one can modify this anisotropy in the resistivity by moving the Fermi level by 0.1 eV with more electron doping. But we note that this computation failed to reproduce the right in-plane anisotropy of the resistivity. Experimentally, we discovered that the a-axis resistivity is smaller than the b-axis, while the calculation results suggest the b-axis resistivity smaller than the a-axis. The origin of this disagreement in the resistivity anisotropy is unclear at the moment. It might originate from noticeable anisotropic renormalization of bands due to the electron correlation effects, which goes beyond the scope of the attempted DFT calculations.

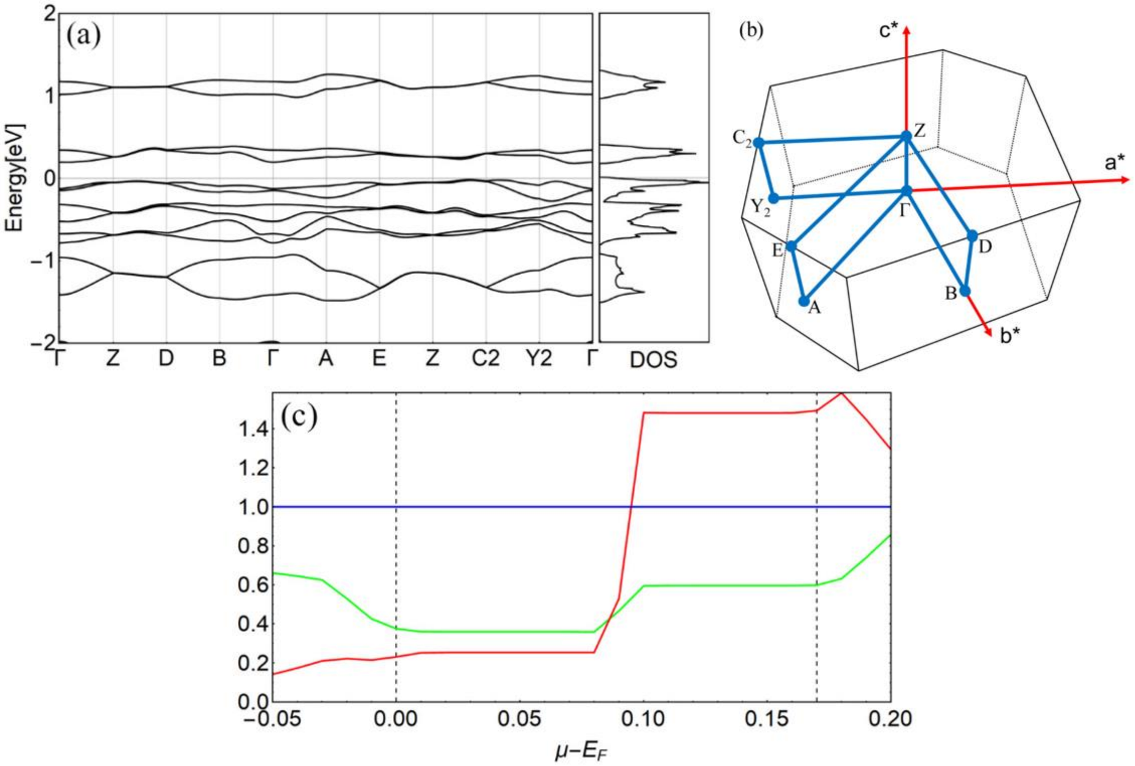

Figure 3.4 (a) DFT band structure: upper six bands are from anti-bonding states, and the lower six bands are from bonding states. (b) Various points in the first Brillouin zone of the Li_2RuO_3 (c) Resistivity divided by ρ_{c^*} at 100 K with changing chemical potential. The green line represents ρ_a/ρ_{c^*} while the red line ρ_b/ρ_{c^*}.

3.3 Van Vleck type susceptibility and its anisotropy

For the magnetism measurements, we aligned ~ 250 pieces of the Li_2RuO_3 crystals with the total mass of ~ 1.091 mg along the c*-axis (perpendicular to the honeycomb layer) using polyimide tape. We piled them in five segments (see the photo in the inset of Fig. 3.5a). The magnetic susceptibility measurement was then carried out from room temperature down to 2 K in an applied field of 1 T parallel and perpendicular to the c^*-axis, using a commercial SQUID magnetometer (MPMS3, Quantum Design). Then we computed the ionic Langevin diamagnetic contribution of the susceptibility using the table in [Ref.3. 21] and subtracted the value from our measured susceptibility.

The magnetic anisotropy of the *ab*-plane was measured by a torque magnetometer because of the meager signal from the tiny crystal. After checking the crystallinity and the crystal axes of the sample with SC-XRD, we attached it on the top of a piezo-resistive microcantilever and measured the magnetic torque along θ_{c*} with ϕ_{ba}-rotation (Fig. 3.5c): θ_{c*} is the angle between the direction of the applied field and the c*-axis, and ϕ_{ba} is the azimuthal angle in the *ab*-plane (see Fig. 3.5c). All the measurements have been conducted using a physical property measurement system (PPMS-9, Quantum Design) with a rotator.

The susceptibility curves in Fig. 3.5a are almost independent of temperature due to the singlet formation of the 4*d*-electrons in the Ru dimers. The up-turn behavior at low temperatures, most probably originating from paramagnetic impurities, is observed regardless of the measurement direction. But what is most notable is that the low-temperature susceptibility has a large van Vleck paramagnetic contribution of 4 to 6 × 10^{-4} emu/mol, which is much larger than the ionic Langevin diamagnetic contribution of -5.6× 10^{-5} emu/mol [Ref.3. 21]. We also note that the c*-axis susceptibility is smaller than that of the in-plane average. This anisotropy of the susceptibility is consistent with the reported data in [Ref.3. 9], but not that of [Ref.3. 10]: the ratio of those two values ($=\chi_{\perp}/\chi_{\|}$) is ~ 0.70 in my data, similar to that of [Ref.3. 9]; in contrast, the susceptibility of the plane-orthogonal direction was reported to be larger than that of the in-plane direction in [Ref.3. 10].

As shown in figure 3.3b and c, the magnetic easy-axis can be identified from a complete angular dependence of the field-induced torque, $\tau(\theta_{c*})$. The amplitude of the $\sin 2\theta_{c*}$ -dependence is proportional to the principal components of the magnetic anisotropy α_{ij}. Figure 3.5b shows that $\tau(\theta_{c*})$ at different azimuthal angles ϕ_{ba}, and $\tau(\theta_{c*})$ can be fitted with a π-periodic sinusoidal function. From these torque data set, we find that the susceptibility in any in-plane direction is always larger than the out-of-plane direction one, confirming the susceptibility measurement results with the five-storied crystals. Figure 3.5c shows the fitted amplitude of the data with a b-to-a rotation. The difference between χ_{ab} and χ_{c*} varies with the azimuthal angle ϕ_{ba}; it is the smallest along the a-axis and the largest along the b-axis. From those two experiments, we could separate the value of the in-plane susceptibility along the a-axis and b-axis.: $\chi_a = 1.56\chi_{c^*}, \chi_b = 1.16\chi_{c^*}$

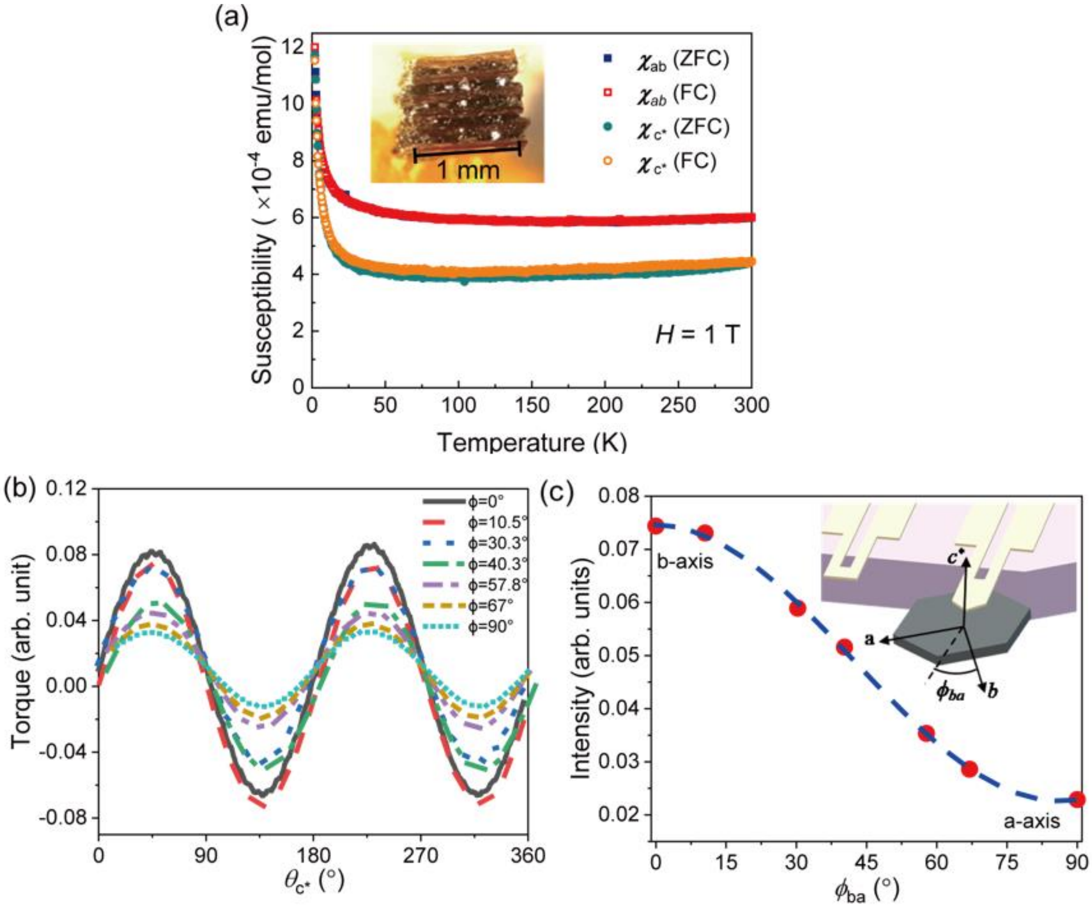

Figure 3.5. (a) Magnetic susceptibilities of the *caxis-aligned filed single-crystals as a function of temperature in the range of 2–300 K, along the out-of-plane (χ_{c^*}, circle marks) and in-plane (χ_{ab}, square marks) directions; the inset figure shows the sample used for this measurement. (b) The angular-dependent torque measurement at fixed azimuthal ϕ angles from ϕ_{ba} = 0° (*b*-axis) to ϕ_{ba} = 90° (*a*-axis). (c) Fitted amplitudes from the data with *ab*-rotation. The inset illustrates the rotating angles and the crystal axes of the measurement.**

3.3.1 "Dimer array" approximation and symmetry analysis

If we ignore the interaction between the Ru-dimers, we can consider the honeycomb lattice as an array of the dimers. In this case, the magnetic susceptibility of the system is just a sum of each dimer. The dimer has three principal axes: one is along with the dimer, and the others are perpendicular to the direction of the dimer, as shown in figure 3.6. There is no off-diagonal term in the 2nd rank tensorial magnetic susceptibility with the principal axes. Still, we have to convert the tensorial magnetic susceptibility with rotation matrices to merge with the contribution of the other dimers. The conversion formula is as follows:

$$\chi_{ij} = \frac{\partial M_i}{\partial H_j} = \sum_{q=x',\, y'z'} (\hat{\imath}\cdot\hat{q})\chi_q(\hat{q}\cdot\hat{\jmath})$$

The $(\hat{q}\cdot\hat{\imath})$ is an element of the rotation matrix. Because of the mirror plane perpendicular to the *b*-axis, we can write a summation of the susceptibility of two dimers in the unit-cell briefly:

$$\chi_a \equiv 2\chi_{aa} = 2\left[(\hat{a}\cdot\widehat{x'})^2\chi_{x'} + (\hat{a}\cdot\widehat{y'})^2\chi_{y'} + (\hat{a}\cdot\widehat{z'})^2\chi_{z'}\right]$$

$$\chi_b \equiv 2\chi_{bb} = 2\left[(\hat{b}\cdot\widehat{x'})^2\chi_{x'} + (\hat{b}\cdot\widehat{y'})^2\chi_{y'} + (\hat{b}\cdot\widehat{z'})^2\chi_{z'}\right]$$

$$\chi_{c^*} \equiv 2\chi_{c^*c^*} = 2\left[(\widehat{c^*}\cdot\widehat{x'})^2\chi_{x'} + (\widehat{c^*}\cdot\widehat{y'})^2\chi_{y'} + (\widehat{c^*}\cdot\widehat{z'})^2\chi_{z'}\right]$$

With this formula, it is possible to calculate the ratio between $\chi_{x'}$, $\chi_{y'}$, and $\chi_{z'}$: the $\chi_{x'}:\chi_{y'}:\chi_{z'}$ ratio is 4:1:10.

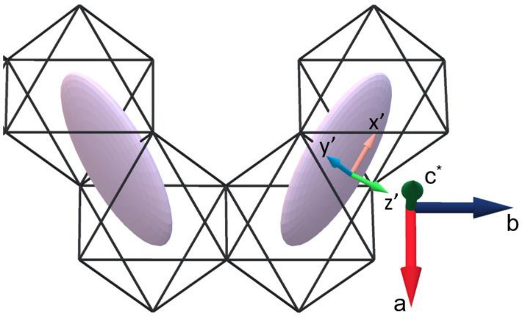

Figure 3.6. The illustration of the dimer array approximation for the honeycomb lattice. The purple ovals are the Ru dimers, and the x′, y′, and z′ are the principal axes of the dimer.

3.3.2 Exact diagonalization calculation

We calculate the van Vleck magnetic susceptibility of the dimer with the exact diagonalization method. The Hamiltonian consists of local Kanamori Hamiltonian with intersite hopping, spin-orbit coupling, and crystal electric field within t_{2g} manifold.

$$H = H_{Kanamori} + H_{CEF} + H_{SOC} + H_{hopping}$$

$$H_{Kanamori} = \frac{U-3J_H}{2}N(N-1) - J_H\left(2\boldsymbol{S}^2 + \frac{1}{2}\boldsymbol{L}^2\right)$$

$$H_{CEF} = \sum_{\alpha\sigma,\beta\sigma'} V_{\alpha\beta}^{CEF} d_{\alpha\sigma}^{\dagger} d_{\beta\sigma'}$$

$$H_{SOC} = \sum_{\alpha\sigma,\beta\sigma'} \lambda(\boldsymbol{l}\cdot\boldsymbol{s})_{\alpha\sigma,\beta\sigma'} d_{\alpha\sigma}^{\dagger} d_{\beta\sigma'}$$

$$H_{hopping} = \sum_{i\neq j,\alpha\sigma,\beta\sigma'} T_{i\alpha,j\beta} d_{i\alpha\sigma}^{\dagger} d_{j\beta\sigma'}$$

Note that for the on-site Coulomb interaction, we have assumed full rotational symmetry. Two system-dependent parameters are V^{CEF} and T. To estimate the size of the crystal electric field (CEF), we use a point charge model and scale the strength of CEF to fit the $10Dq$ to be 3 eV. The CEF matrix is complicated as there is no symmetry to simplify the structure of the matrix, but maximum energy splitting within the t_{2g} manifold should be within 0.1 eV. We choose hopping integrals from DFT calculation to reproduce the gap between bonding and anti-bonding states. To simplify the model, we consider three types of hopping.

$$T_{i,j} = \begin{pmatrix} t_1 & t_2 & 0 \\ t_2 & t_1 & 0 \\ 0 & 0 & t_3 \end{pmatrix}$$

Where t_1 and t_3 are direct intra-orbital *dd*-hopping, and t_2 is from the oxygen mediated *d-p-d* inter-orbital hopping. The t_1 and t_3 are expected to be smaller than t_2 in a typical ideal honeycomb case. But it is longer the case once the lattice dimerized as the size of t_3 increased greatly and t_2 to be slightly increased. The value of t_3 is so large and comparable to U and much larger than Hund coupling. We take $t_1 = -0.17$, $t_2 = 0.32$, $t_3 = -1.2$, $U = 3$, $J_H = 0.4$ and $\lambda = 0.075$. Fig. 3.7a shows the calculated density of the states of each molecular orbital. The dot lines indicate the energy of each single-particle states assigned in the Miura's previous study. Our calculation result shows that our Hamiltonian for the dimer, especially the Kanamori term, which is related to the electron correlation, enhances the electronic gap near the Fermi energy. In both single ion or dimer, the ground state does not have a magnetic moment; therefore, the magnetic susceptibility is originated from the Van Vleck magnetism. The van Vleck paramagnetism along n direction is

$$\chi_{VV} = \frac{2\mu_0\mu_B^2}{V}\sum_{n\neq 0}\frac{|\langle n|\boldsymbol{n}\cdot\boldsymbol{M}|0\rangle|^2}{E_n - E_0}$$

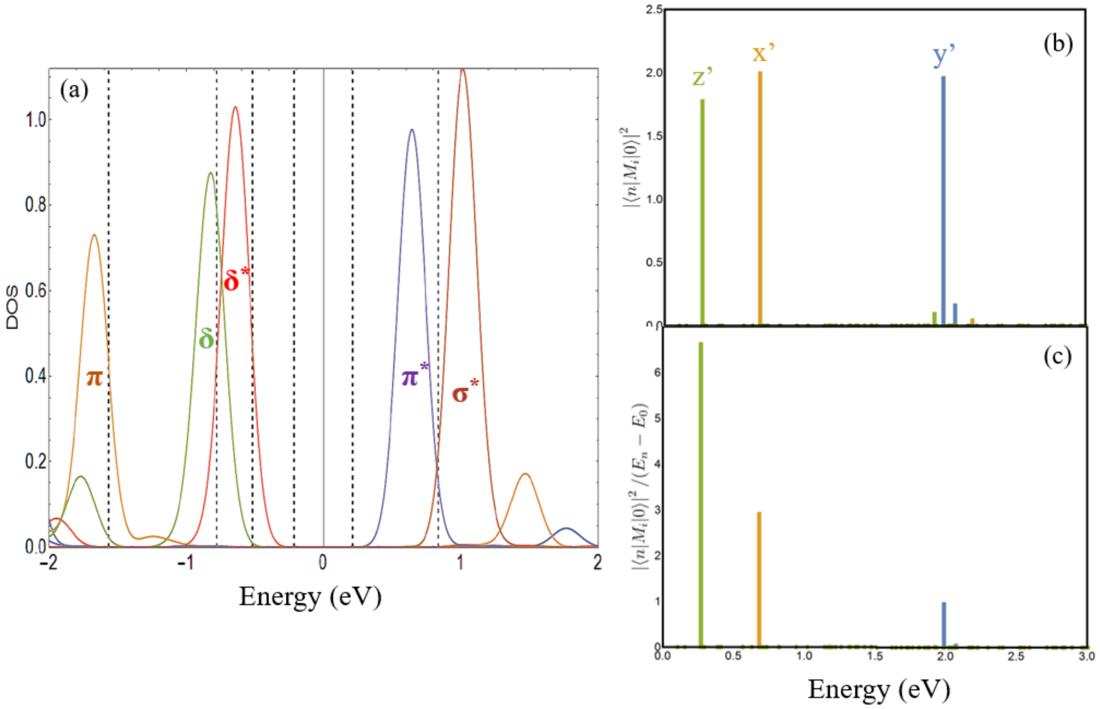

Figure 3.7 (a) The calculated densities of states (DOS) of each molecular orbitals. Black dot lines in the figure signify energies of the single electron state with approximation. (b) Calculated numerators in the equation of the VV magnetism and (c) the gap-weighted numerators. The ratio of the calculation results along the principal axes of the dimer is 3:1:7 (=$\chi_{x'}$:$\chi_{y'}$:$\chi_{z'}$)

The graph in Figure 3.7b shows the numerator of the van Vleck magnetism of the principal axes of the dimer. Although the related orbital for each direction is different, the numerators almost independent of the direction. But the energy gaps, the denominator of the van Vleck magnetism formula, depend on the direction because each molecular orbitals related to the directions have different energy gaps between the bonding and anti-bonding states. Thus, the calculated magnetic susceptibility is highly anisotropic, and the ratio $\chi_{x'}:\chi_{y'}:\chi_{z'}$ is 3:1:7. This calculated ratio has the same tendency as the experimental result, which is 4:1:10. In the calculation, because we did not consider the inter-dimer hopping, which can change the electronic gap, the electronic gaps for the z′ and x′ direction, related to the states near the Fermi-surface, were overestimated. If we correct the energy gap, the calculated values will be more close to the experimental result. Nevertheless, the similarity of the empirical and calculation results back up the validity for the dimer-based analysis for the honeycomb lattice in Li_2RuO_3.

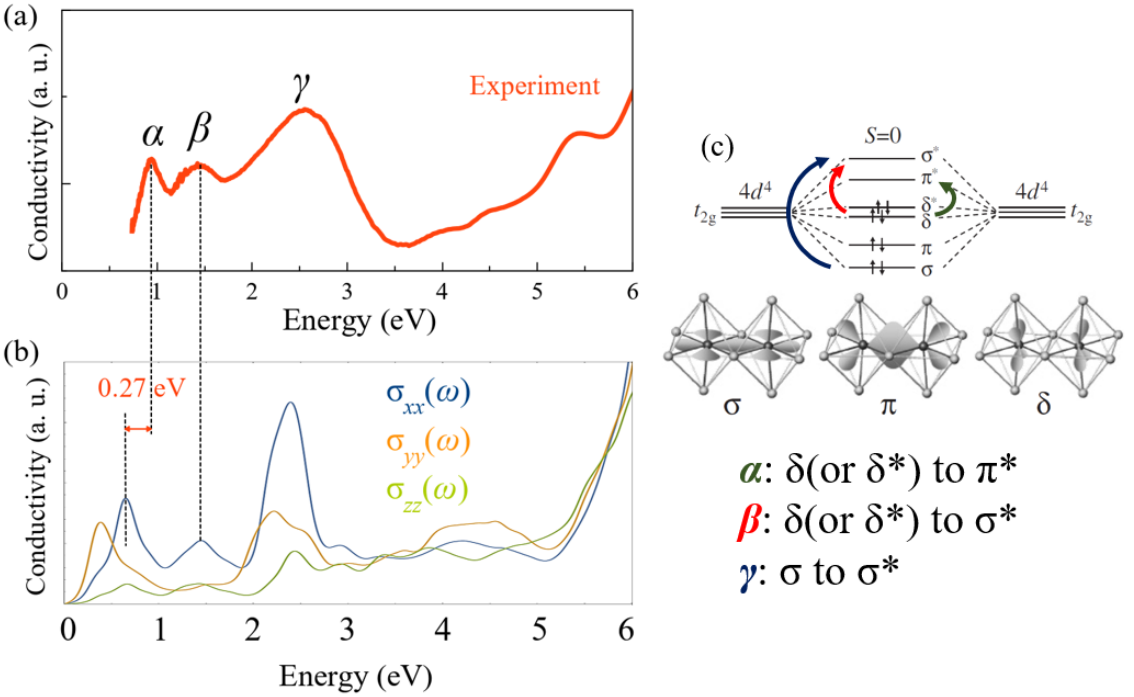

Figure 3.8 (a) Optical Spectra of Li_2RuO_3 and (b) the simulation by the DFT calculation with TB-mBJ potential. (c) Identification of the *α*, *β*, and *γ* peaks in the optical spectra. The *α* peak occurs from an electronic light absorption process from the δ bonds to the *π* bond, and there is about 0.27 eV difference in the position of the peak between the experimental and calculation results. The energy diagram of the Ru dimer in Figure 3.8c is from [Ref.3. 4]**.**

3.4 Discussion and Summary

We examined the anisotropy of physical properties to investigate the effects of both correlation and spin-orbit coupling on the dimerized state. In the DFT calculation, the metallic solution (e.g., in LDA or GGA methods) cannot reproduce the experimentally measured anisotropies in the physical properties, such as resistivity and magnetism. On the other hand, as we discussed above, the calculations with the U give the rational description of the observed anisotropy. It is the discussion in favor of the Coulomb correlations U playing a crucial role in the behavior of Li_2RuO_3.

Of further note, it is insufficient to explain the anisotropic nature of the Li_2RuO_3 with the correlation effect with the TB-mBJ potential only. Figure 3.8a is the optical spectra of the material obtained with ellipsometry, and Figure 3.8b is the calculated spectra based on the DFT calculation results with TB-mBJ potential. The low energy peak α does not fit on the calculation result, while the higher energy peaks β & γ are relatively fit well. The β and γ peaks occur from the absorption process to the σ* anti-bonding of the dimer, whereas the gamma peak is related to the absorption process to the π* anti-bonding. The disagreement of the low energy absorption peak signifies that the DFT calculation with TB-mBJ calculation underestimated the electronic gap. However, the potential function could open the gap, which is not opened by the calculation with LDA and GGA Methods. And as the kinetic energy gain due to the formation of the π- and δ-bonding (~0.3 eV) is smaller than the Hund coupling energy of Ru ion (~0.4 eV), it is not reasonable for us to anticipate that the t_{2g} orbitals, except for the d_{xy} orbitals participating the strong σ-bond, will form the molecular orbital. Therefore it is more valid to consider these orbitals as single atomic orbital and have to take the other interactions, such as spin-orbit coupling, into account for estimating an electronic state of the dimer.

Another point worth noting is the band degeneracy along with directions of specific momentum directions: the Z-D and E-Z-C2-Y2 directions, as shown in Fig. 3.4a. It is perfectly degenerate without the spin-orbit coupling and becomes split slightly with a spin-orbit coupling of 75 meV. This degeneracy is protected by the nonsymmorphic symmetry, a screw axis 2_1 along the b-axis, of the low-temperature phase of $P2_1/m$. This degenerate and nearly flat-band gives rise to a large density of states just below the energy of the Fermi level: our Hall experiment shows that Li_2RuO_3 is intrinsically n-type. Thus, with some control of the Fermi level, such as gating experiments, one might be able to control the ground state - an intriguing direction for future study.

To summarize, we found the clear experimental evidence of anisotropies in both resistivity and susceptibility data for single crystals of Li_2RuO_3. Using theoretical studies, we confirmed that the anisotropy in the susceptibility is reproducible with the DFT calculations using the TB-mBJ potential, indicative of the importance of correlation effects.

References

[Ref.3.1] J. P. Attfield, APL Mater. **3**, 041510 (2015).

[Ref.3.2] S. V. Streltsov and D. I. Khomskii, Phys. - Uspekhi **60**, 1121 (2017).

[Ref.3.3] S. V. Streltsov and D. I. Khomskii, Phys. Rev. B **89**, 161112(R) (2014).

[Ref.3.4] Y. Miura, Y. Yasui, M. Sato, N. Igawa, and K. Kakurai, J. Phys. Soc. Japan **76**, 033705 (2007).

[Ref.3.5] J. Rodríguez-Carvajal, Phys. B Phys. Condens. Matter **192**, 55 (1993).

[Ref.3.6] M. P. Jimenez-Segura, A. Ikeda, S. Yonezawa, and Y. Maeno, Phys. Rev. B **93**, 075133 (2016).

[Ref.3.7] S. A. J. Kimber, I. I. Mazin, J. Shen, H. O. Jeschke, S. V. Streltsov, D. N. Argyriou, R. Valentí, and D. I. Khomskii, Phys. Rev. B **89**, 081408(R) (2014).

[Ref.3.8] J. Park, T.-Y. Tan, D. T. Adroja, A. Daoud-Aladine, S. Choi, D.-Y. Cho, S.-H. Lee, J. Kim, H. Sim, T. Morioka, H. Nojiri, V. V. Krishnamurthy, P. Manuel, M. R. Lees, S. V. Streltsov, D. I. Khomskii, and J.-G. Park, Sci. Rep. **6**, 25238 (2016).

[Ref.3.9] K. Mehlawat and Y. Singh, Phys. Rev. B **95**, 075105 (2017).

[Ref.3.10] J. C. Wang, J. Terzic, T. F. Qi, F. Ye, S. J. Yuan, S. Aswartham, S. V. Streltsov, D. I. Khomskii, R. K. Kaul, and G. Cao, Phys. Rev. B **90**, 161110 (2014).

[Ref.3.11] M. Sathiya, G. Rousse, K. Ramesha, C. P. Laisa, H. Vezin, M. T. Sougrati, M. L. Doublet, D. Foix, D. Gonbeau, W. Walker, A. S. Prakash, M. Ben Hassine, L. Dupont, and J. M. Tarascon, Nat. Mater. **12**, 827 (2013).

[Ref.3.12] P. Syers, D. Kim, M. S. Fuhrer, and J. Paglione, Phys. Rev. Lett. **114**, 096601 (2015).

[Ref.3.13] M. G. Vergniory, L. Elcoro, C. Felser, N. Regnault, B. A. Bernevig, and Z. Wang, Nature **566**, 480 (2019).

[Ref.3.14] P. Blaha, K. Schwarz, G. K. H. Madsen, D. Kvasnicka, J. Luitz, R. Laskowsk, F. Tran, L. Marks, and L. Marks, *WIEN2k: An Augmented Plane Wave Plus Local Orbitals Program for Calculating Crystal Properties* (Techn. Universitat, 2019).

[Ref.3.15] F. Tran and P. Blaha, Phys. Rev. Lett. **102**, 226401 (2009).

[Ref.3.16] A. D. Becke and E. R. Johnson, J. Chem. Phys. **124**, 221101 (2006).

[Ref.3.17] G. Pizzi, D. Volja, B. Kozinsky, M. Fornari, and N. Marzari, Comput. Phys. Commun. **185**, 422 (2014).

[Ref.3.18] A. A. Mostofi, J. R. Yates, G. Pizzi, Y. S. Lee, I. Souza, D. Vanderbilt, and N. Marzari, Comput. Phys. Commun. **185**, 2309 (2014).

[Ref.3.19] F. Mauri and S. G. Louie, Phys. Rev. Lett. **76**, 4246 (1996).

[Ref.3.20] R. Laskowski and P. Blaha, Phys. Rev. B - Condens. Matter Mater. Phys. **85**, 035132 (2012).

[Ref.3.21] G. A. Bain and J. F. Berry, J. Chem. Educ. **85**, 532 (2008).

Chapter 4

Resonant Elastic X-ray Scattering on Li_2RuO_3

Resonant elastic x-ray scattering (REXS) is a specialized tool for observing valence electronic states such as charge, spin, and orbital degrees of freedoms [Ref.4. 1–3]. I employed this technique to survey the molecular orbital in the Ru dimer and its effect on electrons in states near the Fermi energy. The experiment was conducted in the *I16* beamline of the diamond light source in the UK [Ref.4. 4]. This beamline was designed initially for hard x-ray experiments, but during our experiment, the optics for an incident beam was adjusted to control photons with energies of the Ru $L_{2,3}$-edges, which is below the energy of 3 keV (L_2: 2.967 keV / L_3: 2.838 keV). These photons with the energy of L-edges, which excite $2p$ core electrons to the $4d$ valence levels near the Fermi energy, are hard to deal with because they are quickly dissipated in the air, like a photon with energy in the range of a soft x-ray. Nevertheless, I selected those photon energies since resonant scattering processes with the absorption L-edges allow the dipole transition confined in the transition metal, and enable us to directly observe the local state of the valence electrons [Ref.4. 2]. Our experiment was as follows.

(1) X-ray absorption spectroscopy (XAS): I carried out the XAS with the fluorescence-yield mode, which is the way to detect the fluorescent decay of the core hole generated by the x-ray absorption [Ref.4. 5]. Because the fluorescence process for the decaying core hole is dominant in the hard x-ray regime, the majority of the hard x-ray beamlines adopt this method instead of the electron-yield mode. Our experiment also used the fluorescence yield, even though photons with the energy of the Ru-L edge quickly decay in the air.

(2) Scanning for superstructure peaks: I had considered that the super-exchange interaction between the Ru dimers might order the orbital or spin moments of the electrons [Ref.4. 6]. If the rest of the electrons in the t_{2g} manifold, which did not participate in the direct σ-bonds, formed these ordered states, additional resonant reflections, indicating the emerging order, have to appear. Since an orbital ordered state with doubled unit-cells was expected from the herringbone pattern of the dimer and the remaining electronic degrees of freedom, I searched the resonant reflection at every half position.

(3) Characterization of Resonant reflection (010): the nonsymmorphic symmetric operation 2_1 in the space group $P2_1/m$ allows a resonant reflection [Ref.4. 7]. I observed this reflection and measured it from several aspects: the polarization dependency of the scattered beam, temperature dependency with structural phase transition, and the absorption edge dependency and the azimuthal-energy structures near each edge. Then, these results were analyzed by comparison with calculations with FDMNES code, which adopts the Green formalism on a muffin-tin potential approximation [Ref.4. 8].

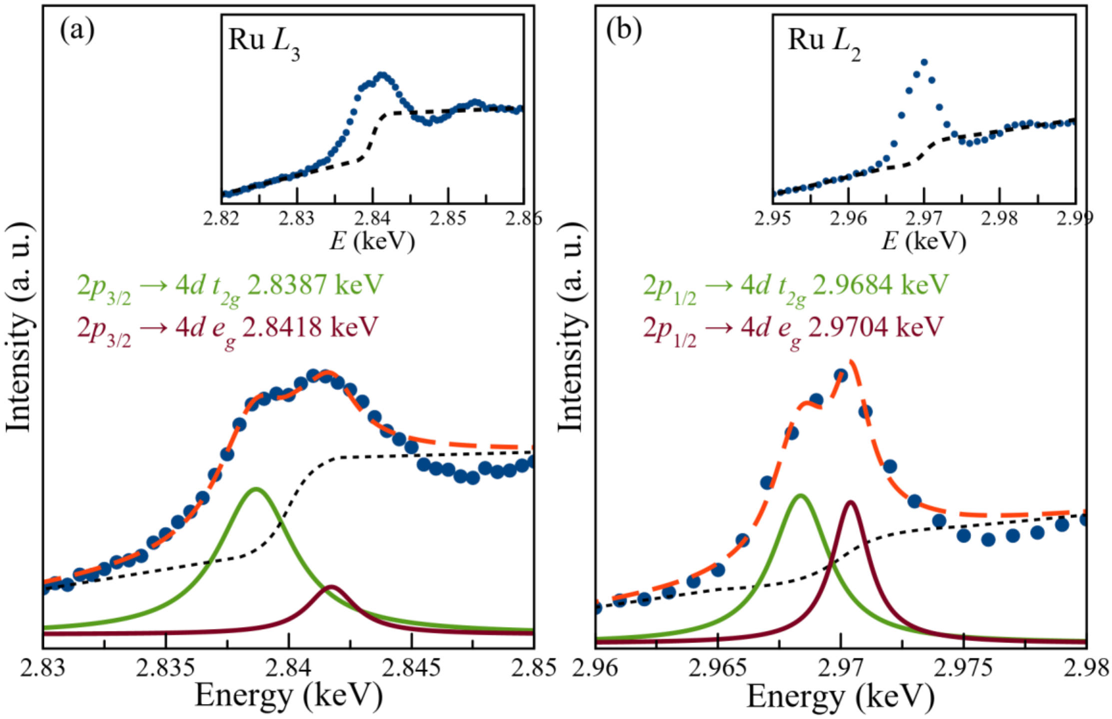

Figure 4.1 X-ray Absorption spectra with the fluorescence-yield mode of both Ru (a) L_3 and (b) L_2 edge. The black dotted lines in both are the arctangent type background function, and the inset graphs show them in a broader range. The green (brown) Lorentzian shape peaks correspond to the photon absorption process, exciting electrons from the 2*p* core levels of Ru to the valence 4*d* t_{2g} (e_g) levels. The red lines are the summation of the absorption peaks and the background function. All measurements were carried out at 300 K.

4.1 X-ray absorption spectroscopy of Li_2RuO_3

Figure 4.1 shows the x-ray absorption spectra of Li_2RuO_3 at both *L*-edges. The fitting results indicate that there are two peaks in both spectra. A previous XAS study on Ca_2RuO_4, which also had the Ru^{4+} ion in the oxygen octahedron, reported that there were also two peaks at L_3: the former peak corresponds to the photon absorption process, to excite 2p core electrons to the valence state of the t_{2g} manifold, and the latter is the result of the process to excite 2p electrons to the e_g level [Ref.4. 9]. The energy gap between the two peaks is 2.5 eV, and the origin of this gap is the crystal electric field splitting, owing to the interaction with oxygen ligands around the Ru ion.

I assigned the peaks in our spectra to be the same as those of Ca_2RuO_4. The energy gap between the two peaks was 3.1 eV in the L_3 spectrum, but 2 eV in the L_2 case. If the energy gap purely originated from the crystal field splitting, it must be identical on both absorption edges. The XAS of La_2RuO_5 showed that there were similar energy gaps between the two peaks at both L-edges [Ref.4. 10]. Although this system also has spin-singlet dimers like Li_2RuO_3, the RuO_6 octahedra have the edge-sharing geometry; thus, the direct overlap between the t_{2g} orbitals is negligible.

The RuO_6 octahedra of Li_2RuO_3, on the other hand, have an octahedron network with corner-sharing geometry. There is a sizeable direct overlap between t_{2g} orbitals, inducing a considerable hopping integral about 1.2 eV [Ref.4. 11]. But the orbital selective nature of the overlap between t_{2g} orbitals produces strongly non-uniform hopping integrals for different orbitals and splits the energy level of the t_{2g} orbitals.

A previous study with XAS on the O-K edge showed that the energy gap between the xy-antibonding molecular orbital and the e_g orbital was about 2 eV. It is the same as that of our L_2 case. Besides, the ratios of the area of both peaks are very different at both edges. The ratio ($=A_{t2g}/A_{eg}$) is 4.84 at L_3 but 1.59 at L_2: it is almost triple. Those distinctions in the energy gap and the area ratio support that the absorption processes of the two edges are accessing different t_{2g} levels.

4.2 Searching for superstructure reflection

I have verified that exchange interactions between dimers form some ordered state, and scanned 64 peak positions in the Ewald sphere of Li_2RuO_3, mainly focusing on the half peak positions. Table 4.1 is a list of the scanned positions in the reciprocal lattice. There is no peak anywhere. Thus I assumed that the symmetry of the electronic system of Li_2RuO_3 would be the same as that of the lattice structure and proceeded with the experiment.

#	*h*	*k*	*l*	#	*h*	*k*	*l*	#	*h*	*k*	*l*
1	-1.5	-1.5	0	22	-1	-1.5	-0.5	46	-0.5	-1.5	0
2			0.5	23			0	47			0.5
3			0.5	24			0.5	48			1
4			1	25			0.5	49			1.5
5		-1	-0.5	26			1	50		-1	-0.5
6			0	27			1.5	51			0
7			0.5	28		-1	-0.5	52			0.5
8			0.5	29			-0.5	53			0.5
9			1	30			0.5	54			1
10			1.5	31			1.5	55			1.5
11		-0.5	-0.5	32		-0.5	-0.5	56		-0.5	-0.5
12			0	33			0	57			0
13			0.5	34			0.5	58			0
14			1	35			0.5	59			0.5
15		0.5	-0.5	36			1	60			0.5
16			0	37			1.5	61			1
17			0.5	38		0	-0.5	62			1.5
18		1	-0.5	39		0.5	0	63		0.5	0.5
19			0	40			0.5	64		1	-0.5
20			0.5	41		1	-0.5				
21		1.5	0	42			0.5				
				43		1.5	-0.5				
				44			0				
				45			0.5				

Table 4.1 Scan list to search for expected superstructure reflections: there is no signal anywhere.

4.3 Tensorial structure factor calculation for Li_2RuO_3

As mentioned in Chapter 2.2, the non-symmorphic symmetry operations cause photons scattered by Thomson scattering to interfere destructively. On the other hand, photons scattered by the resonant process can interfere constructively, and in this case, resonant reflection is observable [Ref.4. 7]. Because only the x-ray absorbing atoms are important in this case, the structure factor of the system can be briefly described by just considering them. The Ru atoms in Li_2RuO_3 occupy the *4f* Wyckoff positions: $Ru_1 = (x, y, z), \mathrm{Ru}_2 = \left(-x, y + \frac{1}{2}, -z\right), \mathrm{Ru}_3 = (-x, -y, -z), \mathrm{Ru}_4 = (x, -y + \frac{1}{2}, z)$, where (x,y,z) = (0.2795, 0.0797, 0.004) The generalized structural factor for *hkl* reflection is as follows.

$$F_{hkl} = f_1 e^{2\pi i(hx+ky+lz)} + (-1)^k f_2 e^{2\pi i(-hx+ky-lz)} + f_3 e^{-2\pi i(hx+ky+lz)} + (-1)^k f_4 e^{-2\pi i(-hx+ky-lz)}$$

$$f_2 = \hat{C}_{2b} f_1, \; f_3 = \hat{I} f_1, \; f_4 = \widehat{m}_b f_1$$

where C_{2b} is the symmetric operation of 180° rotation around the *b*-axis, *I* is the inversion operation located at the center of the dimer, and *m* is the *b*-axis perpendicular mirror plane positioned at the center of two dimers (Figure 4.2). At the absorption *L*-edges where I carried out the experiment, E1-E1 transitions (transition by electric dipole operators) are dominant. Thus the atomic scattering factors are described by a 2nd rank tensor, and the action of the inversion symmetry on them is always +1. Under this condition, the structural factor is as below:

$$\begin{aligned} F_{hkl} &= \left[e^{2\pi i(hx+ky+lz)} + e^{-2\pi i(hx+ky+lz)} + (-1)^k \left(e^{2\pi i(-hx+ky-lz)} + e^{-2\pi i(-hx+ky-lz)}\right)\hat{C}_{2b}\right] f_1 \\ &= 2\left(\cos[2\pi(hx+ky+lz)] + (-1)^k \cos[2\pi(-hx+ky-lz)]\,\hat{C}_{2b}\right) f_1 \end{aligned}$$

For a (010) reflection, the structure factor F_{010} is $2\cos(2\pi y)\left(1 - \hat{C}_{2b}\right) f_1$. The atomic scattering factor is a symmetric tensor; thus the F_{010} represented by the orthonormal basis set $\left(\hat{a}^*, \hat{b}, \hat{c}\right)$ is as follows:

$$F_{010} = 4\cos(2\pi y)\begin{pmatrix} 0 & f_{a^*b} & 0 \\ f_{a^*b} & 0 & f_{bc} \\ 0 & f_{bc} & 0 \end{pmatrix} \sim \begin{pmatrix} 0 & f_{a^*b} & 0 \\ f_{a^*b} & 0 & f_{bc} \\ 0 & f_{bc} & 0 \end{pmatrix}$$

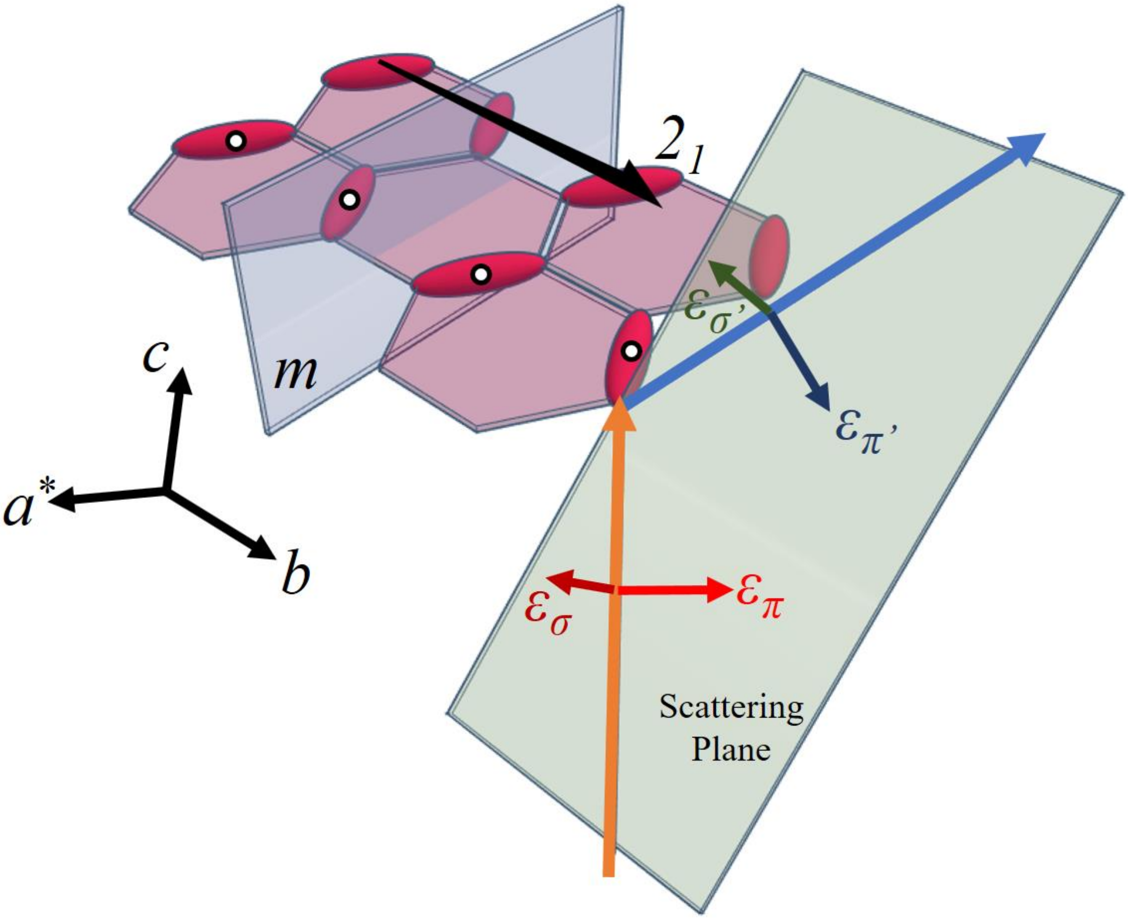

Figure 4.2 The elements of the space group $P2_1/m$ and the scattering geometry of our experiment for observing the (010) reflection of Li_2RuO_3. The pink ovals represent Ru dimers, and they contain an inversion symmetry at their center. The azimuthal scan means the rotation of the scattering plane, and the azimuthal ψ is defined as an angle between the scattering plane and the a^*-axis.

In this orthonormal basis set, the electric field directions of the incident and outgoing linearly polarized light can be expressed in the form:

$$\epsilon_\sigma = (-\cos\psi,\ 0, \sin\psi),\ \ \epsilon_{\sigma'} = (-\cos\psi,\ 0, \sin\psi)$$
$$\epsilon_\pi = (\sin\theta\sin\psi, \cos\theta, \sin\theta\cos\psi),\ \ \epsilon_{\pi'} = (-\sin\theta\sin\psi, \cos\theta, -\sin\theta\cos\psi)$$

where the ϵ_σ ($\epsilon_{\sigma'}$) is the incident (outgoing) X-ray polarization, and they are perpendicular to the scattering plane. The ϵ_π $(\epsilon_{\pi'})$ is the incident (outgoing) X-ray polarization confined in the scattering plane, and perpendicular to the wave vector of the light and the ϵ_σ $(\epsilon_{\sigma'})$ vectors. The ψ is an angle between the principal crystallographic axis $\hat{a}^*$ and the wave vector of the incident vector and the azimuthal zero is chosen when the scattering plane corresponds to the *b-c* plane. The Jones matrix describing each scattering channel is as follows:

$$\hat{\epsilon}' \cdot F_{010} \cdot \hat{\epsilon} = \begin{pmatrix} \epsilon_{\sigma'} \cdot F_{010} \cdot \epsilon_\sigma & \epsilon_{\sigma'} \cdot F_{010} \cdot \epsilon_\pi \\ \epsilon_{\pi'} \cdot F_{010} \cdot \epsilon_\sigma & \epsilon_{\pi'} \cdot F_{010} \cdot \epsilon_\pi \end{pmatrix} \sim cos\,\theta\,(-f_{a^*b}\,cos\,\psi + f_{bc}\,sin\,\psi) \begin{pmatrix} 0 & 1 \\ 1 & 0 \end{pmatrix}$$

Thus there is no signal in the scattering channel, conserving the polarization of light such as σ-σ' or π-π', but the polarization changing scattering processes such as the σ-π' or π-σ' channels are allowed. I can, therefore, write the measured intensity of the σ-π' scattering channel as:

$$I_{\sigma\pi'} = |\epsilon_{\sigma'} \cdot F_{010} \cdot \epsilon_\pi|^2 \sim |-f_{a^*b}\,cos\,\psi + f_{bc}\,sin\,\psi|^2$$

Using the formula, the elements of the atomic scattering factor can be obtained from the azimuthal scanning result.

4.4 Characterization of the resonant reflection (010)

4.4.1 Polarization and temperature dependency

The structure factor calculation result confirms that I can identify the existence of the 2_1 symmetry of this system by measuring the polarization dependence of the resonant reflection. If this system has a non-symmorphic symmetry, the (010) reflection is forbidden in the σ- σ' scattering channel but allowed in the σ-π'. Fig 4.3a shows the polarization dependency of the (010) reflection at the Ru *L_3*-edge. While the scattered intensity in the σ-σ' channel is almost not detected, in the σ-π'channel is observed. On the other hand, the (020) reflection, which emerges with the Thomson scattering process, shows the contrary tendency (Figure 4.3b).

Previous studies have reported that this system has a structural phase transition at 550 K, which changes the space group of this system from P2_1/m (low T. phase) to C2/m (high T. phase) [Ref.4. 12]. Because the space group of the high T. phase, C2/m, does not include the non-symmorphic symmetry operation 2_1, which is the cause of the resonant reflection (010), the resonant X-ray scattered intensity has to vanish with increasing temperature above the phase transition temperature. Fig 4.3c shows that the $(020)_{\sigma\sigma'}$ still exists at over 550 K, but the $(010)_{\sigma\pi'}$

disappears. Thus the resonant reflection originates from the 2_1 symmetry, and it can be reliably concluded that the symmetry of the electronic system is the same as that of the lattice system.

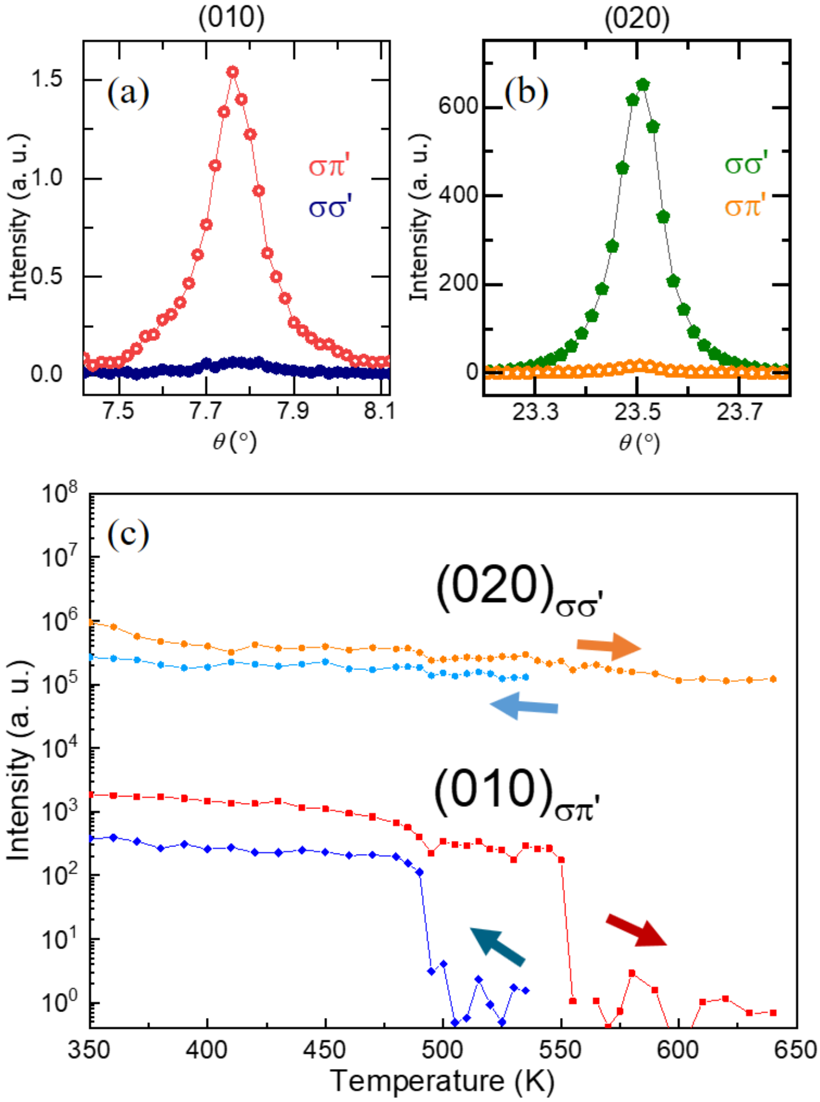

Figure 4.3. The rocking curve of the (a) (010) and (b) (020) reflections at the L_3 edge. While the (020) reflection has a significant intensity in the σ-σ' scattering channel and a small signal in the σ-π' channel, the (010) reflection shows the opposite tendency. Both measurements were carried out at 300 K. (c) Temperature dependence of the intensities of the $(010)_{\sigma\pi'}$ and $(020)_{\sigma\sigma'}$ polarized reflections. The $(010)_{\sigma\pi'}$ disappears at 550 K when the system is heating.

4.4.2 Azimuthal angle and absorption edge dependent behavior of $(010)_{\sigma\pi'}$

In the previous section, I discussed the discrepancy in the absorption spectra at both *L*-edges. The disagreement at both edges is more remarkable in the spectra of the resonant x-ray reflection $(010)_{\sigma\pi'}$. Figure 4.4a and b show the intensity of the resonant reflection varying with the energy of the incident photon and the orientation of the scattering plane at both edges. Both spectra have broad lobe-shaped peaks enhanced near the t_{2g} absorption energy, and those peaks weaken to almost zero intensity near the energy for the e_g level. After that, small peaks emerge and disappear with increasing energy. But the details of the two spectra are very different. First, they have a different behavior of intensity variation on the orientation of the scattering plane. The spectrum of the L_2 edge has a minimum value at ψ = 225° while the position of the minimum of the L_3 edge is ψ = 180°. Besides, the lobe of the L_3 edge is bent near the t_{2g} absorption energy, but that of the L_2 edge does not behave the same way.

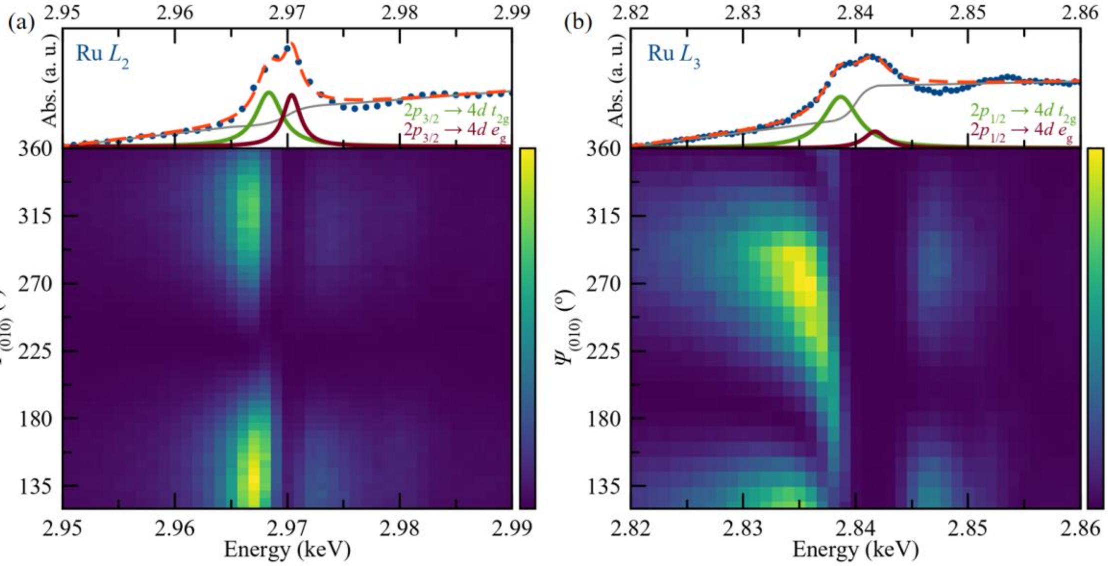

Figure 4.4 A 2d map of the intensity of the $(010)_{\sigma\pi'}$ reflection varying with the azimuthal angle and the energy of the incident photon. The top figures are the same as Figure 4.1. Both maps have no signal at the photon energy of the e_g absorption process.

Several energy cuts of the REXS spectra in Figure 4.4 are plotted in Figure 4.5. The red circles in both figures are the azimuthal scan results at both the L_2 and L_3 edges, and the black diamonds are the data away from the edges. The scans of the L_2 edge and the lower energy have the same orientation dependency. But those of the L_3 edge are almost π/2 different. Furthermore, while the minimum values of the other curves are zero, the azimuthal scan of the L_3 edge has a non-zero minimum. This background in the azimuthal scan results indicates that the atomic scattering factor of the Ru ion is described by a complex number [Ref.4. 13]. But it is impossible to fit the curves at the absorption edges to the equation for the σ-π' scattering channel because they do not have a two-fold symmetry about the azimuthal rotation.

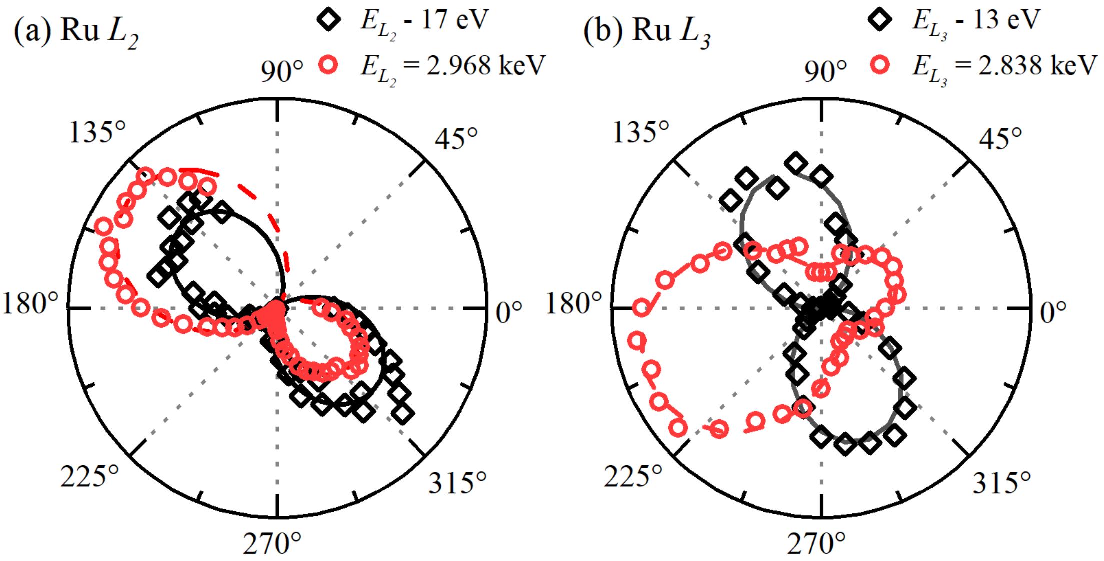

Figure 4.5 Several energy cuts of the REXS spectra in Figure 4.4 The red marks are the data at both absorption edges, and the black markers are data measured below the absorption edges.

To fit the experimental results, I modified the equation as follows:

$$I_{\sigma\pi'} \sim \left|f_0\, sin(\psi - \psi_0) + Be^{i\phi}\right|^2,$$

where B is independent of the orientation of the scattering plane and goes to zero when the energy of the incident photon is far away from the absorption edge, and f_0 and B are real numbers. The value of $tan(\psi_0)$ is f_{a^*b}/f_{bc} when the elements of the atomic scattering factor are real numbers. Table 4.2 shows the fitting results of the experimental results, and the fitting curves are plotted together in Figure 4.5.

Energy	ψ_0	$\sigma_{\psi 0}$	$tan(\psi_0)$	B/f_0	$\sigma_{B/f0}$	ϕ	σ_{ϕ}
E_{L2}	53.52°	0.70°	1.352	0.1684	0.0059	0°	-
E_{L2} - 17 eV	50.17°	1.22°	1.120	0	-	-	-
E_{L3}	-68.68°	0.91°	-2.562	0.7460	0.0279	115.06°	0.86°
E_{L3} - 13eV	19.68°	0.89°	0.358	0	-	-	-

Table 4.2 Fitting results of each energy cut in Fig 4.5

I tried to reproduce the XAS and REXS spectra with FDMNES code, which adopts the Green formalism on a muffin-tin potential approximation [Ref.4. 8]. The input file for running the program is in Appendix A. Previous studies showed that the Hubbard U for electron correlation plays an essential role in this system; thus, our calculation contains the $U = 3.0$.

Fig 4.6a shows the calculated XAS spectra at both absorption edges. In both top and bottom figures, the peaks at the front and back correspond to the absorption process from the 2p core-levels to the t_{2g} and e_g levels, respectively. A calculation with spin-orbital coupling (SOC) of the electrons was also tried. Still, the additional term did not change the spectra much because its intensity was relatively smaller than other terms, such as the crystal electric field splitting. The distance between the two peaks was about 2.6 eV, and they had an identical gap regardless of the absorption edge. It is the same behavior as the La_2RuO_5, which has the corner-sharing RuO_6 network [Ref.4. 10].

Because the muffin-tin approximation for the electric potential and the multiple scattering formalism cannot consider the formation of the Ru dimer, this spectra calculation does not include the direct overlap between the *d*-orbitals of both Ru atoms in the dimer. Figure 4.7b and c show the REXS calculation result of the $(010)_{\sigma\pi'}$ reflection at the L_3 edge with the FDMNES. They could not reproduce the experimental data at all. Figure 4.6c is an energy cut of the REXS along the red dashed line in Figure 4.6b. This azimuthal scan at the t_{2g} absorption energy has 2-fold symmetry. Those discrepancies between the experimental data and the FDMNES calculation results prove that the Ru atoms in the dimer cannot be treated simply as a source of the electric potential.

Instead, it is necessary to consider the overall electronic wave function in the dimer because the Ru dimer has a larger direct hopping integral, of about 1.2 eV. It guarantees the inter-atomic exchange interaction is as large as the intra-atomic one, known as Hund's coupling [Ref.4.

11,14,15]. Naively I can estimate roughly the size of the inter-atomic exchange as below:

$$J \sim \frac{t_{dd}^2}{U - 3J_H} = 0.8 \ eV$$

where t_{dd} is the hopping integral, and U-3J_H is the energy barrier for the direct hopping ($d^4d^4 \rightarrow d^3d^5$). I calculated it with U = 3 eV and J_H = 0.4 eV. The calculation result is larger than the Hund's coupling J_H of electrons in the t_{2g} orbitals of Ru. Thus it is valid for dealing with the significantly inter-atomic correlation, and this system has to be treated based on the dimer.

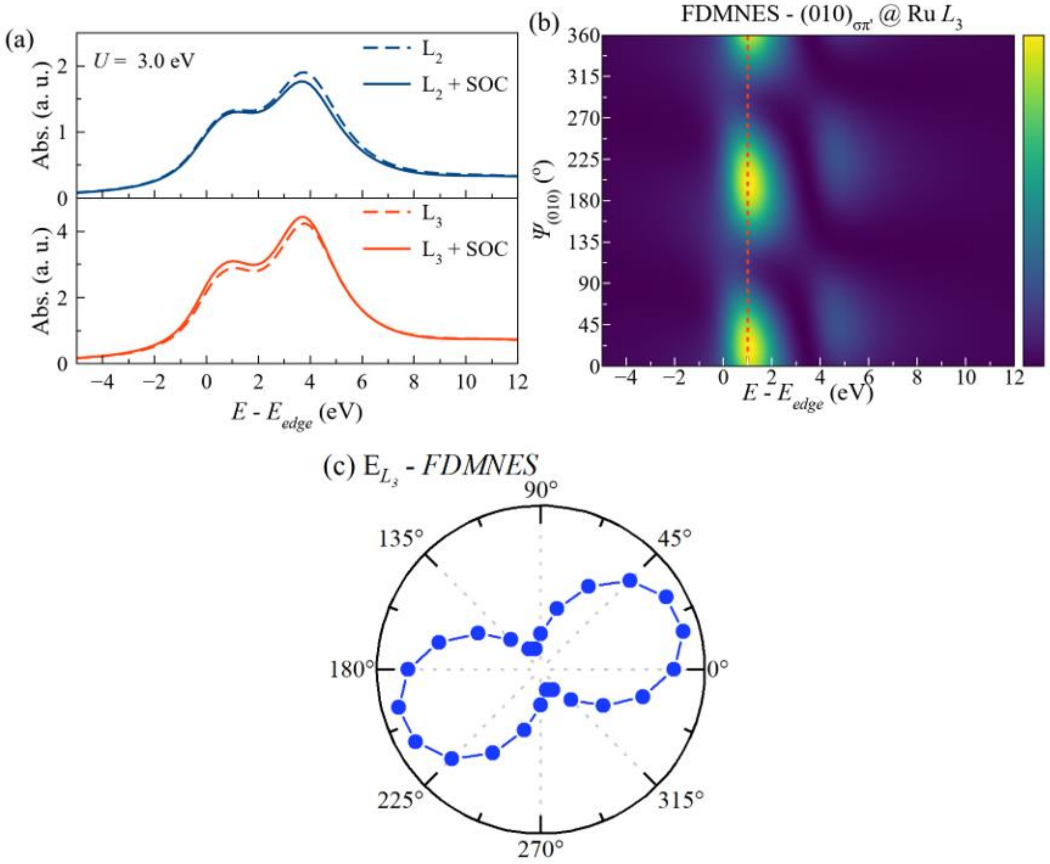

Figure 4.6 The calculations with the FDMNES code. (a) XAS spectra at both absorption edges. The dashed lines are the calculation without SOC, and the solid lines are with SOC. (b) the REXS spectra at the L_3 edge. The calculation at the L_2 edge was the same as that of L_3. (c) The energy cut along the red dash line in the 4.7*b*. It has a 2-fold symmetry about the azimuthal angle.

4.5 Discussion and Summary

I discussed that the single electron approach does not operate well for the dimerized system, and the correlation between electrons in different atoms has to be considered [Ref.4. 16]. In particular, the relationship between Ru's in the same dimer is much more important than the others. Furthermore, the interaction between electron and x-ray is sufficiently local. Thus, this system could be simplified into the model with the Ru and surrounding oxygen atoms: the dimer model. It was already mentioned in the previous chapter, explaining the anisotropy in the van Vleck magnetism.

This model could be solved by the exact diagonalization method, which is a numerical technique to determine the eigenstates and energy of the model Hamiltonian, because of the proper size of this system. The computation cost for this method was too expensive to calculate a larger system. But our previous model does not include the interaction between the dimer and X-ray in the resonant regime. Thus further theoretical studies are required to realize a model with the light-matter interaction.

Our fitting result for the REXS spectra shows that it requires complex numbers to explain the azimuthal scan at the Ru L_3 edge. A series of studies about Fe_3O_4 with REXS show that the orbital states described by linear combinations of the t_{2g} wave functions with complex number coefficients can occur with complex-number elements in the atomic scattering factor [Ref.4. 13,17,18]. In general, those complex number coefficients are related to the spin-orbit coupling (SOC) of the transition metal ions. Although the size of the SOC of the Ru ion, which is about 150 meV, is not that big, its contribution to the complex number mixing of the t_{2g} orbitals is not ignorable. The previous researches on iridates have verified its importance, and I expect that the SOC also plays an important role in the dimer system [Ref.4. 19].

I suggested a modified azimuthal equation for the σ-π' scattering channel. The equation is composed of two resonant components, the 2-fold sinusoidal and the azimuthal angle independent one. There are several examples of interference between several resonant signals. The REXS on GdB_4 shows interference between the M1 and E1 scattering processes: both have 2-fold symmetry, and the interference result also indicates the same symmetry [Ref.4. 20]. The resonant scattering result for germanium shows interference between the resonant peak and the multiple scattered Bragg peak [Ref.4. 21]. In this case, the curves for the azimuthal scan have a sharp anomaly.

In our case, it is hard to identify the azimuthal independent factor in the fitting formula. One candidate is an asymmetric atomic electron-density distribution induced by forming the covalent bond between the transition metal atoms. In the resonant regime, they can be considered small 'pseudo-atoms' and produce a resonant reflection in the proper positions. But this idea requires further discussion [Ref.4. 7].

In summary, the results of XAS and REXS on Li_2RuO_3 shows that there are absorption edge selective behaviors. It implies that the SOC of Ru plays an essential role in the dimer; the azimuthal background of the REXS at the L_3 absorption edge also supports it. Besides, the (010) resonant reflection at both edges behaves as distinct resonant signals are interfering. The FDMNES calculation, which adopts a single electron approach, cannot explain the results; thus, it requires a model considering the correlation effect induced by the dimerization.

References

[Ref.4. 1] S. W. Lovesey, E. Balcar, K. S. Knight, and J. Fernández Rodríguez, Phys. Rep. **411**, 233 (2005).

[Ref.4. 2] J. Fink, E. Schierle, E. Weschke, and J. Geck, Reports Prog. Phys. **76**, 056502 (2013).

[Ref.4. 3] S. Di Matteo, J. Phys. D. Appl. Phys. **45**, 163001 (2012).

[Ref.4. 4] S. P. Collins, A. Bombardi, A. R. Marshall, J. H. Williams, G. Barlow, A. G. Day, M. R. Pearson, R. J. Woolliscroft, R. D. Walton, G. Beutier, and G. Nisbet, AIP Conf. Proc. **1234**, 303 (2010).

[Ref.4. 5] F. de Groot and A. Kotani, *Core Level Spectroscopy of Solids* (CRC Press, 2008).

[Ref.4. 6] G. Jackeli and D. I. Khomskii, Phys. Rev. Lett. **100**, 147203 (2008).

[Ref.4. 7] V. E. Dmitrienko, K. Ishida, A. Kirfel, and E. N. Ovchinnikova, Acta Crystallogr. Sect. A Found. Crystallogr. **61**, 481 (2005).

[Ref.4. 8] Y. Joly, Phys. Rev. B **63**, 125120 (2001).

[Ref.4. 9] H. Gretarsson, H. Suzuki, H. Kim, K. Ueda, M. Krautloher, B. J. Kim, H. Yavaş, G. Khaliullin, and B. Keimer, Phys. Rev. B **100**, 1 (2019).

[Ref.4. 10] H. Wu, Z. Hu, T. Burnus, J. D. Denlinger, P. G. Khalifah, D. G. Mandrus, L. Y. Jang, H. H. Hsieh, A. Tanaka, K. S. Liang, J. W. Allen, R. J. Cava, D. I. Khomskii, and L. H. Tjeng, Phys. Rev. Lett. **96**, 256402 (2006).

[Ref.4. 11] S. V. Streltsov and D. I. Khomskii, Phys. Rev. B **89**, 161112(R) (2014).

[Ref.4. 12] Y. Miura, Y. Yasui, M. Sato, N. Igawa, and K. Kakurai, J. Phys. Soc. Japan **76**, 033705 (2007).

[Ref.4. 13] A. Tanaka, C. F. Chang, M. Buchholz, C. Trabant, E. Schierle, J. Schlappa, D. Schmitz, H. Ott, P. Metcalf, L. H. Tjeng, and C. Schüßler-Langeheine, Phys. Rev. Lett. **108**, 227203 (2012).

[Ref.4. 14] D. Sutter, C. G. Fatuzzo, S. Moser, M. Kim, R. Fittipaldi, A. Vecchione, V. Granata, Y. Sassa, F. Cossalter, G. Gatti, M. Grioni, H. M. Rønnow, N. C. Plumb, C. E. Matt, M. Shi, M. Hoesch, T. K. Kim, T. R. Chang, H. T. Jeng, C. Jozwiak, A. Bostwick, E. Rotenberg, A. Georges, T. Neupert, and J. Chang, Nat. Commun. **8**, 1 (2017).

[Ref.4. 15] Z. V. Pchelkina, A. L. Pitman, A. Moewes, E. Z. Kurmaev, T.-Y. Tan, D. C. Peets, J.-G. Park, and S. V. Streltsov, Phys. Rev. B **91**, 115138 (2015).

[Ref.4. 16] S. Yun, K. H. Lee, S. Y. Park, T. Y. Tan, J. Park, S. Kang, D. I. Khomskii, Y. Jo, and J. G. Park, Phys. Rev. B **100**, 165119 (2019).

[Ref.4. 17] D. J. Huang, H. J. Lin, J. Okamoto, K. S. Chao, H. T. Jeng, G. Y. Guo, C. H. Hsu, C. M. Huang, D. C. Ling, W. B. Wu, C. S. Yang, and C. T. Chen, Phys. Rev. Lett. **96**, 096401 (2006).

[Ref.4. 18] H. Uzu and A. Tanaka, J. Phys. Soc. Japan **77**, (2008).

[Ref.4. 19] B. J. Kim, H. Ohsumi, T. Komesu, S. Sakai, T. Morita, H. Takagi, and T. Arima, Science (80-.). **323**, 1329 (2009).

[Ref.4. 20] S. Ji, C. Song, J. Koo, J. Park, Y. J. Park, K. B. Lee, S. Lee, J. G. Park, J. Y. Kim, B. K. Cho, K. P. Hong, C. H. Lee, and F. Iga, Phys. Rev. Lett. **99**, 1 (2007).

[Ref.4. 21] J. Zegenhagen, T. L. Lee, B. Cowie, R. Felici, K. Hirano, and R. Colella, Phys. Rev. B **64**, 201316(R) (2001).

Chapter 5

A Mn doping study on the valence bond solid phase in Li_2RuO_3

5.1 Valence Bond Liquid phase in Li_2RuO_3

Until the previous chapter, I have focused on the Ru dimer itself in Li_2RuO_3. In particular, most of the study has dealt with the electrons in the bonding state of the dimers as in a spin-singlet state, which is a maximally entangled spin pair or a molecular orbital state, including the roaming electronic state in the cluster [Ref.5. 1]. Although this viewpoint on the system is valid as I have discussed, there is still an ambiguous point: the influence of the interaction between the dimers themselves. Transition metal clusters in a solid form a periodic array called a valence bond solid (VBS) or, sometimes, a valence bond crystal [Ref.5. 2]. For symmetry, the periodicity and pattern of the system are related to the internal degrees of freedom of the cluster. The orbital degree of freedom, especially, as discussed in Chapter 1, is crucially important for the orbital-selective behavior of such bonding formation. Thus, determining how the VBS order evolves by several statistical factors, such as the temperature of the system and doping with other transition metal ions, shows the nature of the cluster.

The previous research has shown that Li_2RuO_3 has a peculiar state above the structural phase transition temperature [Ref.5. 3]. In the x-ray diffraction results, there is no signature of Ru dimers above the transition temperature: the dimers composing the herringbone pattern in the honeycomb lattice are smoothed out (Figure 5.1a). However, pair distribution function analysis, which is the Fourier transformation results of the total scattering measurement and describes a histogram of the bond length in the system, revealed that they are still present above the transition in a disordered or fluctuating manner up to at least 650 °C (Figure 5.1e). The phase with these thermally fluctuating dimers is called a valence bond liquid (VBL). Because of the fluctuations, the system exhibits a diminished local spin moment of $S = 1/2$, instead of the $S = 1$ expected from a typical t_{2g}^4 electron configuration of the case of Ru^{4+} [Ref.5. 3].

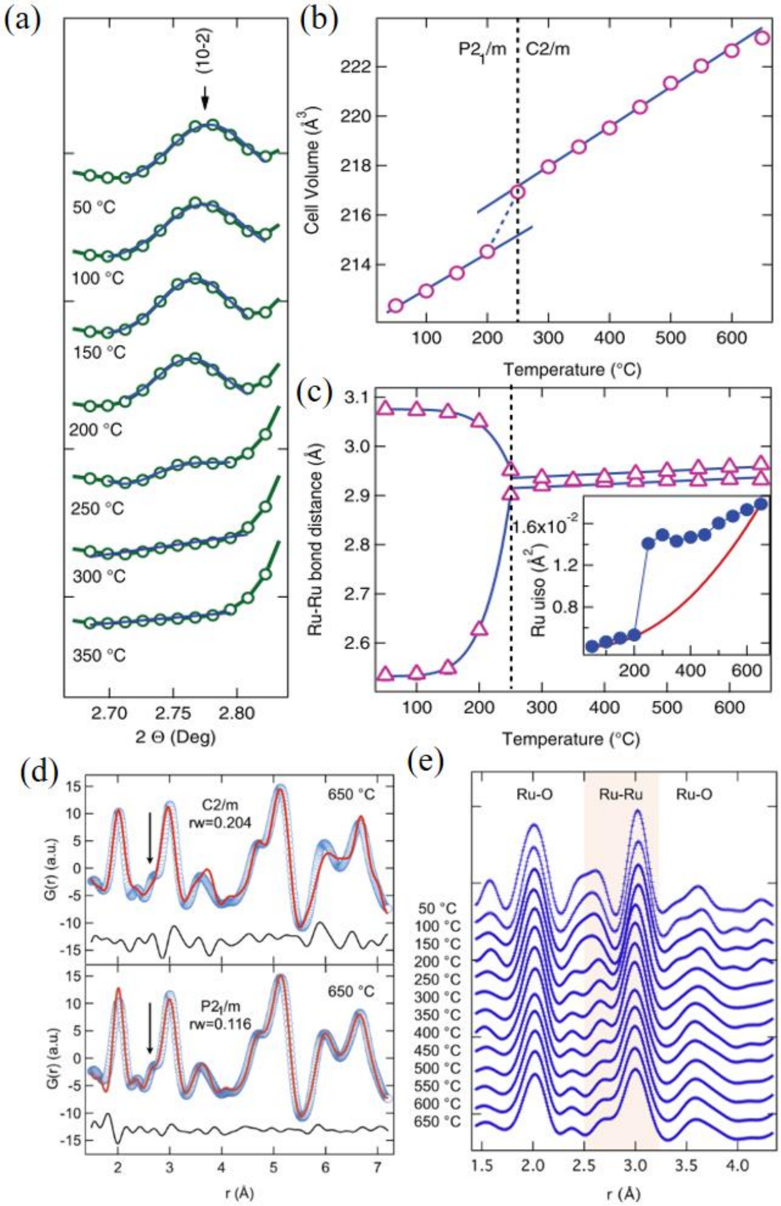

Figure 5.1 Valence bond liquid phase in Li_2RuO_3. (a) Selected narrow region of the X-ray diffraction profile of Li_2RuO_3 as a function of temperature: the (10-2) reflection disappears at the structural phase transition temperature (550 K ~ 270 °C). Temperature dependence of (b) the unit cell volume and (c) the Ru-Ru bond length. (d) Pair distribution data fitting result with the C2/m (top) and $P2_1/m$ (bottom) structure at 650 °C. (e) Temperature evolution of the PDF. The colored region contains the dimerized Ru-Ru bonds [Ref.5. 3]**.**

In this chapter, I will discuss the physical properties of the $Li_2Ru_{1-x}Mn_xO_3$ systems. The purposes of this experiment are as below.

(1) How VBS behaves near the breaking of the Ru dimers by Mn substitution: Because the radial distribution function of the orbital wave function increases with the periodicity of the elements, the replacement with Mn diminishes the direct orbital overlap between transition metal ions and reduces the electronic bandwidth or hopping constant. Thus, the substitution is expected to destroy the dimerization locally, and the accumulation of such defects will break the VBS order if it goes beyond a limit.

(2) Observing the VBL phase with a spectroscopic local probing tool and comparison with the result attained by the total scattering method: The extended absorption fine structure (EXAFS) method is a powerful tool for observing the local structure of a selected absorber [Ref.5. 4]. While the pair distribution analysis with XRD in the previous study provides information about all interatomic distances, the x-ray absorption process-based probing method is specialized for detecting paths centered on the absorbing ion.

5.2 Structural variation of Li_2RuO_3 by Mn doping

Polycrystalline samples of $Li_2Ru_{1-x}Mn_xO_3$ (x = 0, 0.03, 0.05, 0.08, 0.1, 0.2, 0.4, 0.5, 0.6, 0.8, 0.9 and 0.95) were synthesized by a solid-state reaction method. The starting materials were Li_2CO_3 (99.995%, Alfa Aesar), RuO_2 (99.95%, Alfa Aesar), and MnO_2 (99.995%, Alfa Aesar). All of the starting materials were dried at 600 K for 6 h due to their hygroscopic character. The stoichiometric quantity of each compound plus a 5% excess of Li_2CO_3 was placed in an alumina crucible, and the mixture was sintered sequentially at 700 and 900 °C for 12 h at each of the temperatures. After that, each mixture was pelletized and heated at 1000 °C for 24 h.

Li_2RuO_3 ($P2_1/m$) and Li_2MnO_3 (C2/m) form a layered honeycomb lattice with crystal structures, as shown in the right in Figure 5.2a [Ref.5. 5,6]. Both structures are composed of edge-sharing octahedra, but only the ruthenate has the contracted transition metal bonds with the space group $P2_1/m$. Because of the structural similarity between both materials, I could replace the Ru ion with a Mn ion and form a $Li_2Ru_{1-x}Mn_xO_3$ solid solution as in our previous study on $Li_2Mn_{1-x}Ti_xO_3$ solid solution. The structures of the samples were confirmed by powder X-ray diffraction (XRD) using a Rigaku Miniflex2 (Cu target, suppressing K_β with Ni-filter). There raw XRD data of the solid solution is provided in Figure 4.2a. With increasing Mn composition, two peaks at 44°

and 45° come closer and almost merged at x = 0.2, which signifies that the structure with $P2_1/m$ is not valid anymore in $x > 0.2$: In this range, the system has the C2/m structure of Li_2MnO_3 (C2/m Phase).

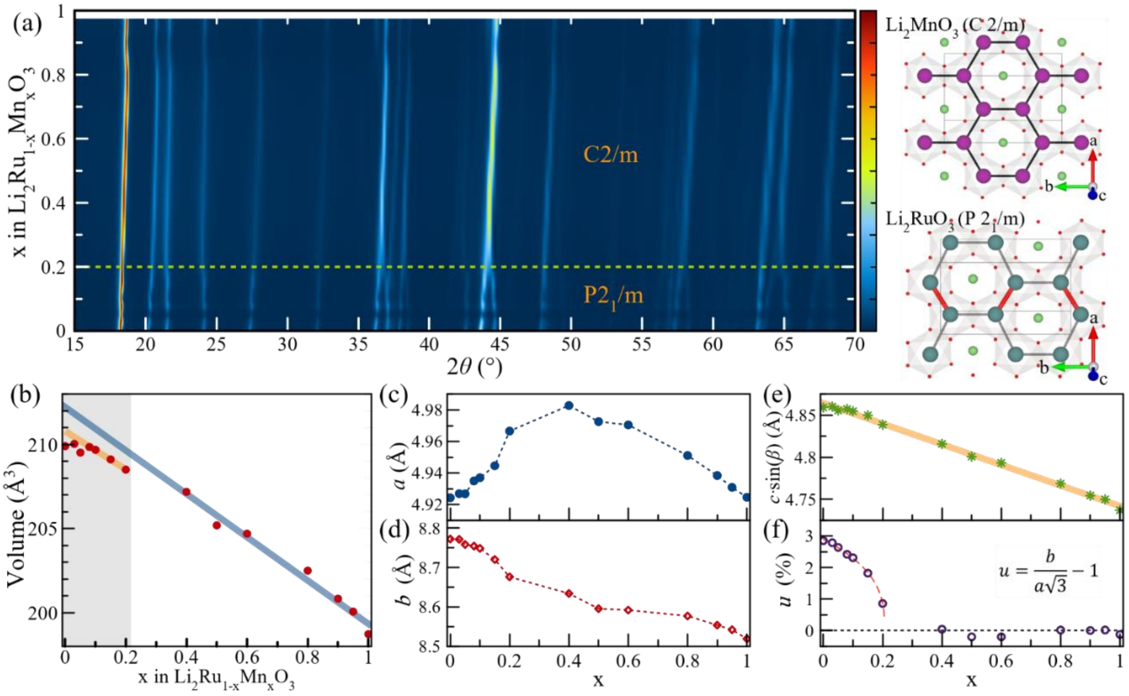

Figure 5.2 (a) XRD data for the $Li_2Ru_{1-x}Mn_xO_3$ systems. The systems with $x \leq 0.2$ have a $P\,2_1/m$ space group, and the rest have C 2/m. The right figures are the crystal structures of Li_2RuO_3 (right bottom) and Li_2MnO_3 (right-top). Both have a layered honeycomb structure separated by Li^+ ions, but only the ruthenate has strong dimerization. The dimer (red) bonds are 2.57 Å, and the black bonds are about 3.05 Å. In contrast, the manganite has regular inter-transition metal ion bonds in the range of 2.82 ~ 2.84 Å. (b) Unit cell volumes of the $Li_2Ru_{1-x}Mn_xO_3$ systems refined by the Le bail method. The blue line is a fitting result for the volume data of the systems with $x > 0.2$, and the orange line is that of the systems with $0.08 \leq x \leq 0.2$. (c ~ e) The lattice parameters *a, b,* and the interlayer distance ($c\cdot\sin\beta$) of $Li_2Ru_{1-x}Mn_xO_3$ systems. *b* and $c\cdot\sin\beta$ decrease monotonically with increasing Mn doping, but *a* has the maximum about at Mn 40 %. The orange line in (e) is the linear fit of the data. (d) The distortion parameter $u = \frac{b}{a\sqrt{3}} - 1$ for $Li_2Ru_{1-x}Mn_xO_3$ systems.

The lattice parameters of each sample were refined with the Le Bail method [Ref.5. 7]. The unit cell volume of the $Li_2Ru_{1-x}Mn_xO_3$ solid solution decreased monotonically with increasing x. Still, it did not show a linear behavior, as expected from Vegard's law, due to the volume reduction by the structural phase transition [Ref.5. 8].

The blue line and the orange line in Fig 5.2b are linear fitting results with $0.4 \leq x \leq 1$ and $0.08 \leq x \leq 0.2$, respectively. This discrepancy between the expectation from Vegard's law and our observation is crucial evidence of the existence of the VBS state in those systems. Furthermore, the volume reduction is related to a distortion in the transition metal honeycomb layer. The inter-layer spacing $c \cdot \sin\beta$ shows the typical behavior of decreasing linearly with increasing Mn because it has a smaller ionic radius than that of Ru (Mn^{4+}: 0.53 Å / Ru^{4+}: 0.62 Å) [Ref.5. 9]. However, *a* and *b* do not show typical behavior, especially the *b/a* ratio, which is $\sqrt{3}$ for a perfect honeycomb case, as mentioned in previous studies, and increases in the $x \leq 0.2$ ($P2_1/m$ phase) [Ref.5. 10].

The distortion parameter *u* in Figure 4.2f indicates how the *b/a* ratio deviates from the ideal honeycomb case. It decreases from 3 to 0 % as Mn content increases in the $P2_1/m$ phase, while it stays at near 0% in the C2/m phase. Besides, the curve fitting with a mean-field type order-parameter shows that the distortion parameter will converge to zero around x = 0.21, which is between x = 0.2 and 0.4. Therefore, our XRD data confirm that the solid solution in the $P2_1/m$ phase has an additional volume reduction related to the distortion in the honeycomb layer, and is maintained until the system with x=0.2.

5.3 Physical Properties of $Li_2Ru_{1-x}Mn_xO_3$

5.3.1 Electrical properties of $Li_2Ru_{1-x}Mn_xO_3$

I measured the high temperature (HT) resistivity of each pelletized sample using the four-probe method with our home-built setup. The voltage difference between I+/I- electrodes was kept below 0.2 V to prevent any possible charging effects due to the high mobility of the Li^+ ions [Ref.5. 11]. The curves in Figure 5.3a are normalized resistivity with the value of 600 K. The data were acquired during cooling. They show insulating (or semiconducting) behavior in the whole range of x, but only the samples with $x < 0.2$ display a distinct phase transition. The black arrows in the figure indicate the phase transition temperature of each curve. The temperature decreases with increasing x, as shown in Figure 5.3b. Also, the value of resistivity above the phase transition reveals an anomaly at the boundary between the $P2_1/m$ and the $C2/m$ phases. The resistivity at 600 K decreases with small Mn doping because they behave as a p-type dopant for the semiconductor. The value increases to $0.05 < x < 0.2$ and has an inflection point at $x = 0.2$.

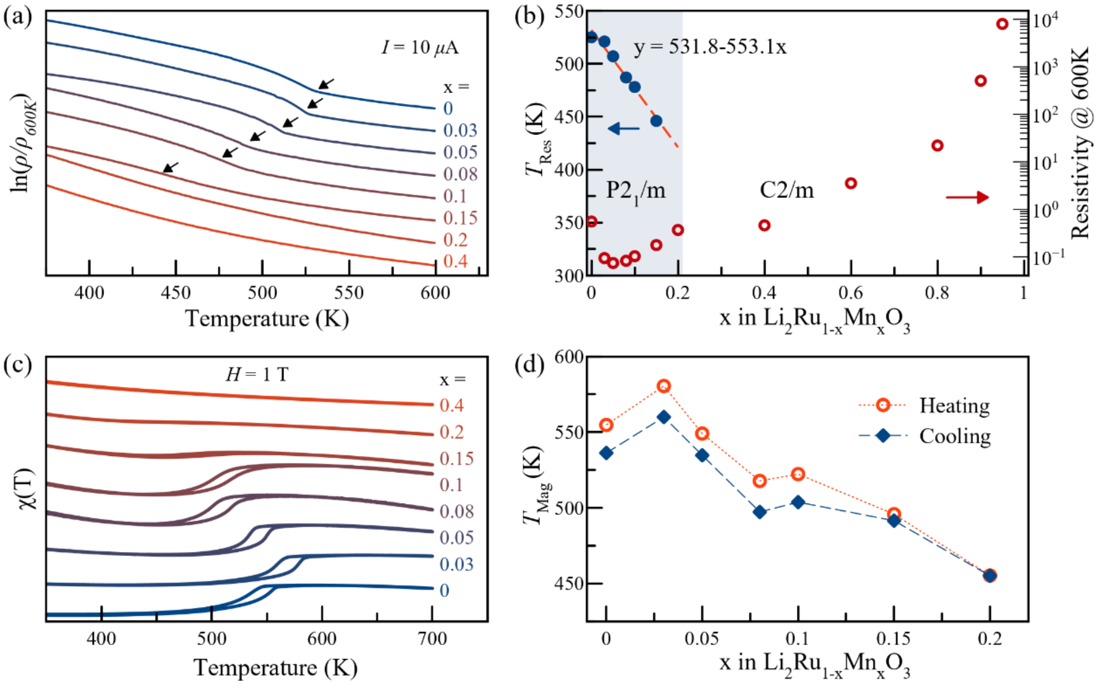

Figure 5.3 (a) Normalized resistivity data with $I = 10\ \mu A$ for $Li_2Ru_{1-x}Mn_xO_3$ systems. The black arrows indicate the phase transition temperature of each resistivity curve. (b) Resistivity phase transition temperature (T_{Res}, left) and resistivity of the $Li_2Ru_{1-x}Mn_xO_3$ systems at 600 K (right). The red dashed line and the equation are a line fitting result of the transition temperatures. (c) Normalized magnetic susceptibility data at $H = 1$ T for $Li_2Ru_{1-x}Mn_xO_3$ systems. (d) Magnetic phase transition temperature (T_{Mag}) of $Li_2Ru_{1-x}Mn_xO_3$ systems.

5.3.2 Magnetic properties of $Li_2Ru_{1-x}Mn_xO_3$

I also studied how magnetic susceptibility evolves upon Mn doping. The HT magnetic susceptibility measurements were carried out in a magnetic property measurement system (MPMS-3, Quantum Design). During the measurement, I sealed the sample with non-magnetic zirconium cement to improve the thermal conduction of the samples. The curves in Fig 5.3c are normalized magnetic susceptibility measured with a magnetic field of 1 T. There are hysteresis loops in the curves for $x \leq 0.2$ due to the phase transition. Interestingly, the phase transition temperatures of both physical properties were the same in the pure Li_2RuO_3 [Ref.5. 6], but they split with increasing Mn. The magnetic transition temperatures rose from 530 K for $x = 0$ to 560 K for $x = 0.03$.

The resistivity transition temperature, on the other hand, decreased monotonically with increasing x. The temperature difference for $x = 0.15$ was about 50 K. Previous studies by K. Mehlawat and Y. S. Ponosov reported that the transition of Li_2RuO_3 is a combination of two consecutive phase transitions [Ref.5. 12,13], and it has both the nature of the first- and second-order phase transitions. Our result also shows that the transition is complicated, but additional experiments are needed for a more comprehensive understanding. Given the results of the electric and magnetic properties so far, the $Li_2Ru_{1-x}Mn_xO_3$ systems can be divided into the $P2_1/m$ and the $C2/m$ phases, and the solid solution in the $P2_1/m$ phase has a phase transition like the pure Li_2RuO_3.

5.3.3 Thermal properties of the phase transition of $Li_2Ru_{1-x}Mn_xO_3$

The enthalpy change during the HT phase transition of the sample was measured using differential scanning calorimetry (Discovery DSC, TA Instrument). Figure 5.4a shows the heat consumption of the $Li_2Ru_{1-x}Mn_xO_3$ solid solution in the $P2_1/m$ phase during the phase transition. The phase transition temperature decreases linearly, and its value is close to that of resistivity in Figure 5.3b. The deviation between the two sets of transition temperatures is due to the hysteresis in the first-order phase transition. The integrated area for $x = 0$ is 1.0 kW·K/mol, and the enthalpy change during phase transition is 6.0 kJ/mol (Heating rate: 10 K/min). This value corresponds to 62 meV per chemical formula (Figure 5.4b).

A previous study by S. A. J. Kimber reported that the calculated energy difference between the Armchair ($P2_1/m$) and Parallel ($C2/m$) structure is 42 meV, which is suggested to represent the energy difference between the VBS and VBL phases [Ref.5. 3]. Our result is 20 meV bigger than this value. The excess did not originate from the volume change: the 10^{-30} m^3 unit cell volume variation only contributed about 0.0006 meV to the enthalpy at normal atmospheric pressure. Instead, it perhaps has an electronic origin. Li_2RuO_3 is an insulator over the entire temperature range. Still, the calculated electronic density of states in the Kimber's study has no electronic energy gap near the Fermi energy, regardless of the phase transition. This discrepancy could cause electronic energy reduction by the phase transition to be underestimated.

The enthalpy change ΔH of the phase transition decreases as x increases, and this indicates that the substitution of Mn for Ru breaks the dimers (Figure 5.3b). Furthermore, it also reduces the entropy variation per transition metal ion ΔS during the phase transition: the linear fitting result shows that a replacement of one Mn particle reduces the ΔS by 4.11. The ΔS per ruthenium ion of pure Li_2RuO_3 is 1.3, which is closer to 1.38 (= ln4) than 1.10 (= ln3). In the case of x = 0.2, the vicinity of the boundary of the $P2_1/m$ and the C2/m phases, the averaged entropy variation ion is only 0.51. Even converse the entropy variation to the value per remaining Ru ions, the entropy variation is 0.631, which is smaller than ln2.

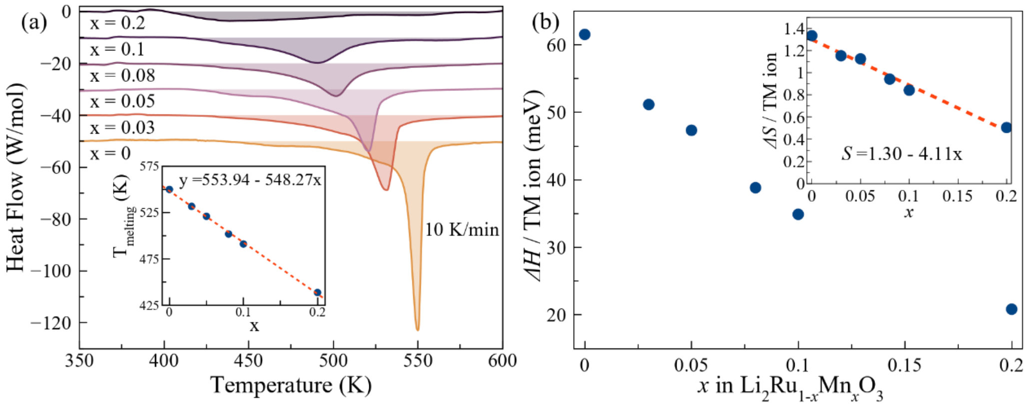

Figure 5.4 (a) Differential scanning calorimetry (DSC) heat flow curves for a series of $Li_2Ru_{1-x}Mn_xO_3$ systems. The inset graph shows the phase transition temperature ($T_{melting}$) of the systems. The linear fitting result is shown as a dashed red line. (b) Variation of enthalpy change ΔH per transition metal ion with x for $Li_2Ru_{1-x}MnO_3$. The inset graph shows the calculated entropy change ΔS $(=\int dQ/T)$ per transition metal ion during the phase transition

5.4 Local variation in Li_2RuO_3 Structure by Mn doping

The EXAFS spectra were measured at the Ru *K*-edge, and the experiment was carried out in the transmission mode at the beamline 10C at Pohang Accelerator Laboratory (PAL). The samples were sealed in polyethylene for room temperature measurement. For HT measurement, I mixed the sample with BN at a 1:1 ratio and pelletized it. The data were processed and analyzed with Demeter [Ref.5. 14]. Fig5.5a is a k^2-weighted Fourier transform (FT) 300 K EXAFS spectra at the Ru–*K* edge for $Li_2Ru_{1-x}Mn_xO_3$ (x = 0, 0.05, 0.1, 0.2 and 0.4, the range of FT: 3 ~ 14 $Å^{-1}$). The position of a peak on the spectra is generally 0.3 ~ 0.4 Å shorter than the actual interatomic length because of the phase shift by the potentials near scatting and absorbing ion.

In the previous research, the peaks around 1.5 Å and 2.2 Å were identified as single scattering paths for Ru-O (2.0 ~ 2.1 Å) and Ru-Ru (Dimer, 2.57 Å) respectively [Ref.5. 15]. Our 300 K data showed that the length of the Ru-Ru dimer was not affected by Mn doping regardless of the symmetry of the system. The 2.2 Å peak was not shifted by Mn doping until x = 0.4. Fig5.5a and 5.5c show the temperature dependence of EXAFS spectra for $Li_2Ru_{0.9}Mn_{0.1}O_3$ and $Li_2Ru_{0.8}Mn_{0.2}O_3$, respectively. The peak at 2.2 Å, which represents the single scattering path between Ru ions in the dimer, does not shift with increasing temperature. However, its intensity decreases because of thermal broadenings. Besides, there is no obvious change between before and after phase transition temperature, unlike the EXAFS results on other VBS systems such as VO_2 and 1*T*-$CrSe_2$ [Ref.5. 16,17]. This analysis shows that the dimers still exist above the phase transition temperature, and the samples are in the VBL state.

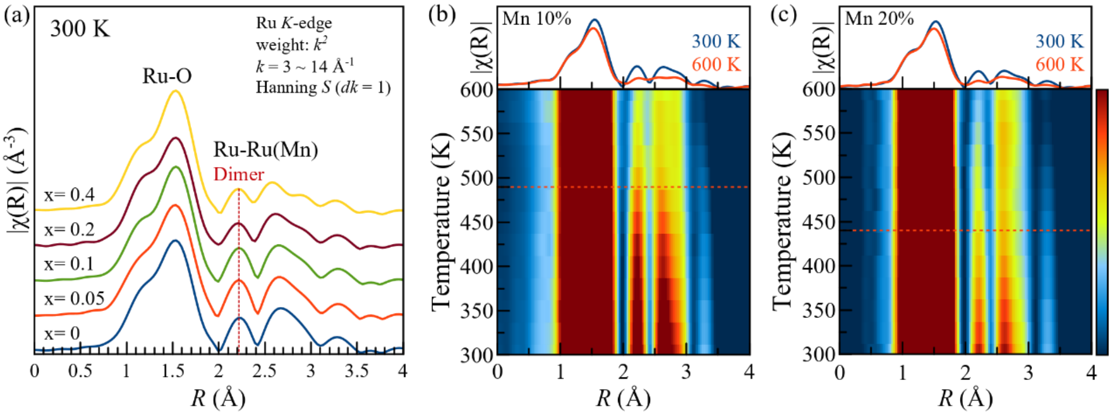

Figure 5.5 (a) The k^2-weighted Fourier transform magnitudes of the Ru K-edge EXAFS spectra of the $Li_2Ru_{1-x}Mn_xO_3$ (x=0, 0.05, 0.1, 0.2) systems. The red dashed line is a guide for the eye. (b) and (c) are the temperature evolutions of the EXAFS spectra of $Li_2Ru_{0.9}Mn_{0.1}O_3$ and $Li_2Ru_{0.8}Mn_{0.2}O_3$, respectively. The graphs on top show that the half-path length related to the dimer (~ 2.2 Å) exists regardless of the structural phase transition in both compositions. The red dashed lines in both color maps are the phase transition temperatures of both compounds.

5.5 Discussion and Summary

In the view of the EXAFS, the local environment of the Ru does not seem to change much despite the structural phase transition with increasing volume. It is more apparent than the PDF analysis because the EXAFS result only displays bonds, including Ru. This technique is more powerful when studying a doped system: it is possible to distinguish the bond, including a specific atom.

The previous EXAFS study with the photon energy of the Mn K-edge showed that Mn ions in the $Li_2Ru_{0.5}Mn_{0.5}O_3$ did not participate in the transition metal dimer [Ref.5. 15,18]. It is presumed the reason why this happened is that the energy reduction from the Ru-Mn dimer is smaller than that of the Ru-Ru dimer. It is because the overlap between the *d* orbitals and direct hopping between Ru-Mn are smaller than those of the Ru-Ru, due to the radially confined nature of the *3d* electrons in Mn. But in the case of the Mn ion, instead, it can reduce more energy by indirect O-assisted hopping through the super-exchange mechanism. As a result, the Mn ions prefer not to get involved in the dimer. Thus the substitution breaks the dimers and collapses the VBS order in the end. The previous theoretical discussion demonstrated that the orbital degeneracy causes spontaneous dimerization of spins and induces the herringbone pattern of the VBS. From our experimental data, the calculated value of $\partial(\Delta H)/\partial x|_{x=0}$, which is the latent heat variation due to the Mn substitution, is - 0.26 eV, and the $\partial(\Delta S)/\partial x|_{x=0}$ is -4.11. I expect that those values can be calculated from the orbital model in [Ref.5. 19] and be related to the parameter of the model.

The experimental results of the structural deformation, resistivity, and magnetic susceptibility showed that the ordered dimer phase is only maintained until x = 0.2. On the other hand, our EXAFS data for x = 0.4 and Ru K-edge data of $Li_2Ru_{0.5}Mn_{0.5}O_3$ in Y. Lyu's research [Ref.5. 15] show that the Ru dimer still exists in the C2/m compounds. But it is hard to consider those systems to be in VBS state because of the absence of the reduction in the unit cell volume. Instead, a disordered honeycomb lattice with local clustering is more reasonable: the VBL state exists. The previous theoretical study mentioned other types of orbital patterns, such as trimers or closed chains [Ref.5. 19]. Although those patterns were rejected in the case of the perfect Ru honeycomb, it could be a proper ground state in the heavily doped system because the Mn substitution breaks the dimers and makes the Ru network finite. It requires further calculations, such as Monte Carlo simulation.

In summary, the structural deformation, resistivity, and magnetic susceptibility of $Li_2Ru_{1-x}Mn_xO_3$ show that this system has a phase transition above x = 0.2. The thermal analysis for the VBS state shows that the enthalpy and entropy variation during the phase transition decreases with increasing Mn substitution. But the local structure study with EXAFS indicates that the dimerization is not much changed by the Mn doping and rising temperature. It indicates Mn doping also can induce the VBL state in Li_2RuO_3.

References

[Ref.5. 1] K. Boguslawski, P. Tecmer, Ö. Legeza, and M. Reiher, J. Phys. Chem. Lett. **3**, 3129 (2012).

[Ref.5. 2] N. Read and S. Sachdev, Phys. Rev. B **42**, 4568 (1990).

[Ref.5. 3] S. A. J. Kimber, I. I. Mazin, J. Shen, H. O. Jeschke, S. V. Streltsov, D. N. Argyriou, R. Valentí, and D. I. Khomskii, Phys. Rev. B **89**, 081408(R) (2014).

[Ref.5. 4] J. J. Rehr and R. C. Albers, Rev. Mod. Phys. **72**, 621 (2000).

[Ref.5. 5] S. Lee, S. Choi, J. Kim, H. Sim, C. Won, S. Lee, S. A. Kim, N. Hur, and J. G. Park, J. Phys. Condens. Matter **24**, (2012).

[Ref.5. 6] Y. Miura, Y. Yasui, M. Sato, N. Igawa, and K. Kakurai, J. Phys. Soc. Japan **76**, 033705 (2007).

[Ref.5. 7] A. Le Bail, Powder Diffr. **20**, 316 (2005).

[Ref.5. 8] L. Vegard, Zeitschrift Für Phys. **5**, 17 (1921).

[Ref.5. 9] R. D. Shannon, Acta Crystallogr. Sect. A **32**, 751 (1976).

[Ref.5. 10] S. Yun, K. H. Lee, S. Y. Park, T. Y. Tan, J. Park, S. Kang, D. I. Khomskii, Y. Jo, and J. G. Park, Phys. Rev. B **100**, 165119 (2019).

[Ref.5. 11] M. Sathiya, G. Rousse, K. Ramesha, C. P. Laisa, H. Vezin, M. T. Sougrati, M. L. Doublet, D. Foix, D. Gonbeau, W. Walker, A. S. Prakash, M. Ben Hassine, L. Dupont, and J. M. Tarascon, Nat. Mater. **12**, 827 (2013).

[Ref.5. 12] Y. S. Ponosov, E. V Komleva, and S. V Streltsov, Phys. Rev. B **100**, 134310 (2019).

[Ref.5. 13] K. Mehlawat and Y. Singh, Phys. Rev. B **95**, 075105 (2017).

[Ref.5. 14] B. Ravel and M. Newville, in *J. Synchrotron Radiat.* (International Union of Crystallography, 2005), pp. 537–541.

[Ref.5. 15] Y. Lyu, E. Hu, D. Xiao, Y. Wang, X. Yu, G. Xu, S. N. Ehrlich, K. Amine, L. Gu, X. Q. Yang, and H. Li, Chem. Mater. **29**, 9053 (2017).

[Ref.5. 16] T. Yao, X. Zhang, Z. Sun, S. Liu, Y. Huang, Y. Xie, C. Wu, X. Yuan, W. Zhang, Z. Wu, G. Pan, F. Hu, L. Wu, Q. Liu, and S. Wei, Phys. Rev. Lett. **105**, 226405 (2010).

[Ref.5. 17] S. Kobayashi, N. Katayama, T. Manjo, H. Ueda, C. Michioka, J. Sugiyama, Y. Sassa, O. K. Forslund, M. Månsson, K. Yoshimura, and H. Sawa, Inorg. Chem. **58**, 14304 (2019).

[Ref.5. 18] D. Mori, H. Kobayashi, T. Okumura, H. Nitani, M. Ogawa, and Y. Inaguma, Solid State Ionics **285**, 66 (2016).

[Ref.5. 19] G. Jackeli and D. I. Khomskii, Phys. Rev. Lett. **100**, 147203 (2008).

Chapter 6

Summary and Outlook

6.1 Summary

In this dissertation, Li_2RuO_3, a layered honeycomb structure consisting of Ru dimers in a herringbone pattern, was explored in various aspects to investigate the effect of direct overlap between d-orbitals of the transition metal ions.

The single-crystal growth of the ruthenate was successfully done. And the study on the anisotropy of physical properties shows that it is valid to regard the system as an array of the base unit, dimer. Besides, the DFT calculation result shows that the inter-atomic Coulomb interaction and electronic correlation are essential for describing this system correctly.

X-ray spectroscopic methods are appropriate to probe the state of transition metal clusters because they can detect not only the spin degrees of freedom but the charge and orbital ones. The x-ray absorption spectroscopy (XAS) and the resonant elastic x-ray scattering (REXS) result show that there are absorption edge selective behaviors that imply an influence of the spin-orbit coupling on this system. Furthermore, the REXS result reveals the correlation effect, which cannot be explained with the single-electron approach.

The solid solution $Li_2Ru_{1-x}Mn_xO_3$ was investigated to the inter-dimer interaction. The structural, resistivity and magnetic susceptibility of this system show that the herringbone-patterned dimer phase is maintained up to $x = 0.2$ and above that is in the disordered phase. The thermal analysis and the extended x-ray absorption fine structure result display that the replaced Mn does not participate in the dimer and breaks merely the herringbone pattern.

6.2 Outlook

A series of studies used to investigate Li_2RuO_3 could be applied to other clustered systems. The anisotropy of physical properties and x-ray spectroscopic methods could identify the electronic state of the cluster, and the doping study gives inter-cluster information. Trimer, which is a cluster of three transition metal ions, is also an interesting object to study; $LiVO_2$, Nb_3Cl_8 are such systems [Ref.6. 1,2]. The extension of the study on clustered systems could make systems of valence bond solids categorize.

My research shows that electrons in the dimer of Li_2RuO_3 are highly correlated. This system is expected to have triplon-type elementary excitations, which is a quasiparticle from a spin singlet-triplet excitation [Ref.6. 3]. The excitation would include entangled spin pair, which is originated from the dimer. Although XAS and REXS are outstanding in investigating the electronic state of the dimer, those methods cannot detect excitations in the system. Resonant inelastic x-ray scattering, which is an x-ray spectroscopy technique utilizing a resonant inelastic process, is an ideal method to observe such excitation. I expect to observe the effects of the entanglement at room temperature by investigating the triplon.

References

[Ref.6.1] H. F. Pen, J. Van den Brink, D. I. Khomskii, and G. A. Sawatzky, Phys. Rev. Lett. **78**, 1323 (1997).

[Ref.6.2] Y. Haraguchi, C. Michioka, M. Ishikawa, Y. Nakano, H. Yamochi, H. Ueda, and K. Yoshimura, Inorg. Chem. **56**, 3483 (2017).

[Ref.6.3] M. Kohno, O. A. Starykh, and L. Balents, Nat. Phys. **3**, 790 (2007).

Appendix

FDMNES Code for Li_2RuO_3

```
-----------------------------------------------------------------------------------------------------------
 Comment
    Ru- L edges in Li2RuO3
 Filout
   LRO_XAS/L3_U3/XAS_U3
 Range
   -15.0 1.0 -8.0    0.2    10. 1. 20.0
 Radius
   3.9
 Edge
   L3
 Hubbard
   3.0
 Eimag
   0.1
 Spinorbit
 Quadrupole
 Density
 Polarise
 Green
RXS
 0 1 0    1 2    0. ! Sigma - Pi; The azimuth is specified, thus a scan is not performed
 0 1 0    1 2    30.
 0 1 0    1 2    60.
 0 1 0    1 2    90.
 0 1 0    1 2    120.
 0 1 0    1 2    150.
```

```
0 1 0    1 2    180.
0 1 0    1 2    210.
0 1 0    1 2    240.
0 1 0    1 2    270.
0 1 0    1 2    300.
0 1 0    1 2    330.
0 1 0    1 2    360.

Atom
 44 2    4 2 6. 5 0 2.
   3 0
   8 0
Spgroup      ! number 11
 P121/m1
Crystal
         4.931        8.795      5.132      90.      108.22002      90.
  1      0.27949      0.076748      0.00411        ! Ru    sym= 1 (4f)
  2      0.77370      0.250000      0.00560        ! Li1 sym= m_b (2e)
  2      0.77010      0.095500      0.50740        ! Li2 sym= 1 (4f)
  2      0.25230      0.250000      0.48590        ! Li3 sym= m_b (2e)
  3      1.00490      0.077620      0.22640        ! O1 (4f)
  3      0.50270      0.082920      0.74550        ! O2 (4f)
  3      0.50940      0.250000      0.23410        ! O3 (2e)
  3      0.04510      0.250000      0.78190        ! O4 (2e)

Convolution
End
```

Publication list

[1] **Seokhwan Yun**, Ki Hoon Lee, Se Young Park, Teck-Yee Tan, Junghwan Park, Soonmin Kang, D. I. Khomskii, Younjung Jo, and Je-Geun Park, *"Magnetic and electrical anisotropy with correlation and orbital effects in dimerized honeycomb ruthenate* Li_2RuO_3*"*, Phys. Rev. B **100**, 165119 (2019).

[2] Soonmin Kang, Yi Tseng, Beom Hyun Kim, **Seokhwan Yun**, Byungmin Sohn, Bongju Kim, Daniel McNally, Eugenio Paris, Choong H. Kim, Changyoung Kim, Tae Won Noh, Sumio Ishihara, Thorsten Schmitt, and Je-Geun Park, *"Orbital-selective confinement effect of Ru 4d orbitals in* $SrRuO_3$ *ultrathin film"*, Phys. Rev. B **99**, 045113 (2019).

[3] So Yeun Kim, Min-Cheol Lee, Garam Han, Marie Kratochvilova, **Seokhwan Yun**, Soon Jae Moon, Changhee Sohn, Je-Geun Park, Changyoung Kim, and Tae Won Noh, *"Spectroscopic studies on metal-insulator transition mechanism in correlated materials"*, Advanced Materials **30**, 1704777 (2018).

[4] Vladimir V. Gapontsev, Ernst Z. Kurmaev, Clastin I. Sathish, **Seokhwan Yun**, Je-Geun Park, and Sergey V. Streltsov, *"Spectral and magnetic properties of* Na_2RuO_3*"* J. Phys.: Condens. Matter 29, 405804 (2017).

[5] Soonmin Kang, Kangwon Kim, Beom Hyun Kim, Jonghyeon Kim, Kyung Ik Sim, Jae-Ung Lee, Sungmin Lee, Kisoo Park, **Seokhwan Yun**, Taehun Kim, Abhishek Nag, Andrew Walters, Mirian Garcia-Fernandez, Jiemin Li, Laurent Chapon, Ke-Jin Zhou, Young-Woo Son, Jae Hoon Kim, Hyeonsik Cheong, and Je-Geun Park, *"Ultra-narrow magnetic exciton in van der Waals antiferromagnet* $NiPS_3$*"*, Accepted in Nature.

[6] J. Jeong†, S. H. Chun†, **Seokhwan Yun**†, J. H. Lee, I. Eom, M. Kim, K. S. Kim, S.-Y. Park, J. Park, S. Kang, C. Kim, D. Cho, H. Lee, I. H. Baek, D. G. Porter, A. Bombardi, Y. U. Jeong, C. Song, and J.-G. Park, *"Ultrafast dynamics of the dimer state in* Li_2RuO_3 *measured by tender X-ray free-electron laser*", submitted to Nature Material. (†: equally contribution)

[7] **Seokhwan Yun**, B. H. Kim, K. H. Lee, D. G. Porter, S. Di Matteo, S. Kang, J. Jeong, A. Bombardi, and J.-G. Park, *"Resonant elastic x-ray scattering on the molecular orbital in* Li_2RuO_3*"*, in preparation.

[8] **Seokhwan Yun**, K. H. Lee, C. Kim, J. Park, D. Y. Cho and J.-G. Park, *"Freezing point depression of valence bond liquid in* $Li_2Ru_{1-x}Mn_xO_3$*"*, in preparation.

국문초록

Li_2RuO_3 내의 루테늄 이합체에 관한 연구

윤석환
물리천문학부 물리학전공
서울대학교 대학원

전이금속 산화물 내의 전이금속 이온들은 *d*-궤도 원자가 전자를 가지며, 해당 함수의 국소성으로 인하여 인접하는 리간드와의 궤도 겹침만이 이 전자의 거동을 기술하는데 중요한 영향을 미칠 것으로 생각되어왔다. 그러나 최근 연구는 해당 전이금속의 주기에 따른 궤도 반경의 변화, t_{2g} 다양체의 특성, 리간드의 국지적 구조에 의하여 이 궤도 함수가 큰 직접 겹침이 가능하고 이러한 경우 이 궤도 겹침 또한 전자의 거동을 기술하는데 중요한 역할을 한다는 것을 보고하였다. 특히 이러한 조건들이 만족하는 경우 전이금속 이온들 몇몇씩 뭉치 (cluster)를 이루어 행동하며 이 때 뭉치 내 전자의 파동 함수는 분자 궤도 함수 (molecular orbital)로 기술된다. 본문에서는 이에 대한 연구의 일환으로 루테늄 산화물 Li_2RuO_3 내의 이합체 (dimer) 뭉치에 대하여 연구하였다.

Li_2RuO_3는 리튬으로 분리되어있는 루테늄 벌집 모양 격자가 첩첩이 쌓여있는 구조를 갖는 물질이다. 이 육각격자 내의 루테늄 이온들은 두 개씩 짝지어 서로의 간격을 줄여 이합체를 이루며 550 K의 구조상전이를 통하여 청어뼈 (herringbone) 모양의 격자를 만든다. 이 청어뼈 유형의 격자는 비등방적인 기하를 갖고 있어, 격자 내의 방향에 따라 물성의 차이를 가질 것으로 예상되었고, 이를 통하여 루테늄 이합체 내의 전자들의 행태를 확인하고자 하였다.

이전의 연구에서 Li_2RuO_3의 여러가지 물성이 측정되어 왔으나, 이는 모두 다결정 시료를 이용한 것이었고 단결정 시료는 합성법이 보고되지 않았었다. 본 연구에서는 이방성을 측정하기 위하여 고품질의 단결정 시료를 합성하고 합성된 시료의 전기적, 자기적 비등방성을 측정하고 이를 밀도 범함수 이론 계산과 비교하였다. 그 결과, 이합체 내 두 루테늄 이온의 전자 간의 쿨롱 반발력 고려해야만 전기적 띠틈의 존재를 모사할 수 있으며, 이에 의한 전자 간 상관 관계가 전기적 이방성에 영향을 미치는 것을 확인하였다. 이를 바탕으로 전자 간 상관 관계를 고려한 모델을 세워 완전 대각화 계산을 통하여 자기적 비등방성을 재현해낼 수 있었다. 이로부터, Li_2RuO_3 의 이합체의 전자 구조와 그 물성을 설명하기 위해서는 전자 간 상관 관계를 고려해야 함을 확인할 수 있었다.

이보다 좀 더 Li_2RuO_3의 전자구조와 스핀, 오비탈의 배열 형태에 대해 직접적인 관측을 통하여 이합체에 대한 이해를 증진하고자 X선을 이용한 일련의 연구를 진행하였다. 루테늄은 4주기 원소로서 약 2.9 keV에 해당하는 L-흡수 선단 (absorption edge)을 갖는데, 이 에너지는 전통적으로 연X선과 경X선으로 구분되는 두 영역의 중간에 위치하며 기술적 이유로 제어가 힘들다고 알려져 있다. 따라서 해당 영역대의 에너지를 활용한 실험을 지원하는 영국의 Diamond 방사광 가속기의 I16 빔라인에서 해당 연구를 수행하였다.

Li_2RuO_3 시료에 대하여 루테늄 L_2와 L_3 두 흡수 선단에서 X선 흡수 분광학 (x-ray absorption spectroscopy)을 실시한 결과, Li_2RuO_3의 흡수 스펙트럼이 흡수 선단에 따라 다름을 확인하였다. 이를 바탕으로 (010) 봉우리에서 공명 탄성 X선 산란을 수행하였고, 두 흡수 선단에서 (010) 공명 봉우리의 거동이 다름을 확인하였다. 이는 공명 대상인 2p 속전자 (core-electron)의 각운동량에 따라 전이 규칙이 적용 됨을 시사하며, 이합체 내의 t_{2g} 전자의 스핀-궤도 결합이 유효한 영향을 미침을 의미한다. 또한 두 흡수 선단에서의 공명 탄성 X선 산란 신호의 방위각 의존성을 확인한 결과 서로 다른 방위각 의존성을 갖는 두 신호가 간섭한 것을 확인하

였다. 이러한 실험의 결과들을 단일 전자 근사 계산 코드인 *FDMNES* 계산과 비교한 결과 크게 맞지 않음을 확인하였으며, 이는 이합체화에 의한 오비탈의 직접 겹침과 이에 따른 전자간 상관이 물질의 전자/스핀/오비탈 구조에 영향을 미친 결과이다.

Li_2RuO_3는 구조 상전이 (550 K)이상의 온도에서는 X선 산란 실험 결과로부터 벌집 모양 격자 내에 이합체가 존재하지 않는 것으로 간주되어왔다. 그러나 전산란 (total scattering)법을 이용한 짝분포 함수 분석 (pair distribution function analysis) 결과, 상전이 온도 이상에서도 이합체가 여전히 남아 있음이 확인되었다. 본문에서는 격자 내의 루테늄을 망간으로 치환한 고용체 (solid solution)를 합성하여 전이 금속 오비탈 간 직접 결합을 감소시켜 상전이가 변화하는 경향을 확인하고, 광역 엑스선 흡수 미세 구조법 (extended x-ray absorption fine structure, EXAFS) 방법을 이용하여 치환률과 계의 온도에 따른 국소 구조변화를 관찰하였다. 그 결과 치환률에 따른 구조와 저항, 자화율의 변화로부터 치환률이 20 %까지 Li_2RuO_3와 같은 이합체를 포함하는 청어뼈 격자를 갖는 것을 확인하였다. 또한 망간 치환에 따라 상전이 시의 엔트로피 변화가 선형적으로 감소하고 루테늄 이온 주변의 국소 구조가 거의 바뀌지 않는 것을 관측하였다. 이는 전이 금속의 주기에 따른 오비탈 반경의 차이에 의해 루테늄과 망간이 이합체를 형성하지 않고, 망간 치환은 이합체 청어 뼈 모양 격자를 와해시키는 역할을 함을 뒷받침한다. 또한 루테늄 주변 국소 구조가 상전이 전후로 바뀌지 않음을 확인하였는데, 이는 이합체가 상전이에 의해 사라지지 않음을 짝분포 함수 분석 결과보다 분명하게 보여준다.

주요어: Li_2RuO_3, 루테늄 산화물, 이합체화, 이방성, 공명 탄성 엑스선 산란, 광역 엑스선 흡수 미세 구조법, 엑삼스

학 번: 2015-20340

감사의 글

최종 심사가 끝나고도 며칠간 학기가 끝난 정도의 해방감 밖에 들지 않았으나, 이 글을 쓰려 감사한 분들을 떠올리니 지난 몇 년간 제가 추구해온 목표가 목전에 있음이 비로소 실감이 됩니다. 운이 좋게도 제 대학원 기간 동안 너무 좋은 환경에서 연구를 할 수 있었습니다. 이렇게 좋은 연구 환경을 제공해 주신 박제근 교수님께 깊이 감사드립니다. 교수님께서는 연구자의 모범으로서 저에게 많은 가르침을 주시고 제가 처한 어려움의 해결책과 나아가야 할 방향에 대한 단초를 주셨습니다. 제게 알려주신 것들을 체화하여 이후로 찾아올 시련을 헤쳐나가도록 하겠습니다. 또한 팀 리더이신 정재홍 박사님께 감사드립니다. 박사님께서는 저의 연구실 선배로서, 또 바로 앞선 세대의 연구자로서 후배인 저에게 박사가 갖춰야 할 자격이 무엇인지를 알려주셨습니다. 학위를 받는 것이 정해졌음에도, 저에게 부족한 것이 너무 많습니다. 앞으로 부족한 것들을 갖추어 연구자로서 거듭나도록 하겠습니다. 이기훈 박사님께서는 저에게 물리에 대한 많은 것을 알려주셨습니다. 제 첫 프로젝트를 진행하면서 박사님과 했던 많은 논의와 공부들이 자양분이 되어 박사학위를 받는 데 큰 도움이 되었습니다. 조연정 교수님께서는 실험물리학자로서 추구해야 할 바를 알려주셨습니다. 2, 3년 차에 교수님과 함께 실험하며 얻은 배움이 이후에도 많은 도움이 되었습니다. 앞으로도 이론적, 실험적 지식을 쌓는 데 게으름 없이 정진하겠습니다.

Dear Prof. Khomskii, it was a great honor for me to work with you. Your previous works and the discussion with you have made me inspired. I look forward to working with you again next time.

제 학위 심사를 맡아 주신 김기훈 교수님, 유재준 교수님, 박철환 교수님께도 감사의 말씀을 드립니다. 심사 중에 주신 조언들이 제 연구의 부족한 부분을 채우는 데 큰 도움이 되었습니다. 바쁘신 와중에도 제 학위 발표를 경청해 주시고 학위 논문을 심사해주셔서 감사합니다.

재능있는 동료들과 함께한 경험들은 저에게 가르침과 반성을 주고 새로움에 대한 자극과 열정을 일깨워주었습니다. 지난 십 년이 넘는 학위 기간 동안 훌륭한 동기, 선후배들과 함께한 기억들은 제가 학교로부터 얻은 가장 큰 자산으로 이후 제 삶의 밑바탕이 될 것입니다. 제 학부 동기이자 연구실 선배인 강순민 박사는 저와 몇 년간 X선 실험을 함께하며 자신의 경험을 전수해주었을 뿐만 아니라 어려운 순간들을 함께하였습니다. 제 학위 기간 동안 가장 즐겁고 값진 경험을 하게 해준 순민이에게 감사의 뜻을 표합니다. 박기수 박사는 제가 지도교수를 선택하는 데 가장 크게 기여한 사람입니다. 기수와의 상담 덕분에 박제근 교수님을 제 지도교수로 선택할 수 있었고, 좋은 환경에서 만족스러운 학위 기간을 보낼 수 있었습니다. 뿐만 아니라 제 연구실 선배인 최성일 박사, 오주성 박사, 심하성 박사, 조환범

박사 및 이성민에게 감사드립니다. 이분들 덕분에 연구에 필요한 많은 것들을 배울 수 있었고 연구실에 잘 적응할 수 있었습니다. 연구실 동기인 태훈이는 제 하소연과 고민을 들어줘 제 정서적 안정에 큰 도움을 주었습니다. 채빈, 평제, 희준은 같은 팀원이자 재능있는 후배들로 타성에 젖은 저를 반성하게 하였습니다. 또한 반데르발스팀 멤버인 수한, 유진, 인호, 정현 그리고 기웅은 함께 일할 기회는 많지 않았지만 같은 연구실 구성원으로 함께 공부하고 토의를 통해 제가 더 성장할 수 있도록 도움을 주었습니다. 우리 연구실에서 인턴으로 함께한 김하림, 박승현, 심상우 학생은 저에게 많은 놀라움을 주었습니다. 그들의 지적 성취도와 학문에 대한 열정, 그리고 연구에 대한 자세는 저보다 훌륭합니다. 이 학생들이 훗날 학계의 핵심 연구자가 될 것을 믿어 의심치 않습니다. 또한 제 학창 시절을 함께 한 동기인 강성모, 신상원, 유용찬, 이한호, 김진욱에게 감사를 표하고 싶습니다.

제 학사 과정 동안 장학금을 지원해 준 MBK 장학재단에 감사드립니다. 대학생 시절 등록금을 마련하는 데 쫓기는 삶을 살았더라면 제가 박사 학위를 하고자 하는 의지를 지속하지 못하였을 것입니다. 김병주 이사장님과 류주희 국장님께 감사드리며 지원해주신 바에 보답하는 삶을 살도록 하겠습니다.

학위를 받는 것은 저 자신의 노력만으로 이루어진 것이 아닙니다. 제가 학위를 받는 동안 묵묵히 저를 지켜봐 준 가족에게 감사합니다. 아버지와 어머니께 드리는 감사는 그 어떤 표현을 써도 부족할 것입니다. 못난 아들이 이토록 오랫동안 공부하는 것을 지켜봐 주셔서 감사합니다. 누나와 매형께, 학위 기간 동안 여러가지로 제 편의를 봐주셔서 감사 드립니다. 여동생 어진이에게, 여러모로 이상한 오빠를 참아줘서 고맙다. 작은아버지들께 감사드립니다. 철호 할아버지와 태중 삼촌에게, 학업의 선배님들로서 저를 지켜봐 주시고 조언 주셔서 감사드립니다. 마지막으로 곧 나와 가족이 될 여진이에게. 지난 9년간 옆에서 내 불안한 청춘의 날들을 함께 해줘서 고마워. 너와 내일을 함께 할 수 있다는 것이 오늘 나의 가장 큰 기쁨이야. 나와 함께 하기로 약속해줘 정말 고맙다.

일주일에 한 번씩 앞으로 어떤 세상이 다가올 것인지, 그곳에서 제가 할 수 있는 것은 무엇인지에 대하여 생각합니다. 제가 대학에서 보낸 지난 10년간 세상이 너무 급격하게 바뀌었고 앞으로는 이전보다 더 빠른 속도로 많은 것들이 변하리라 생각됩니다. 제가 공부를 한 것들이 차후에 어떻게 쓰일지 아직은 모르겠으며, 어리석게도 앞으로 할 고민과 이를 해결하는 과정들의 가치를 세상으로부터 인정받을 수 있을지 두려움이 앞섭니다. 저와 같은 길에 서셨던 선배들께서 그러셨듯, 제게 주어진 길을 초연히 걸어가도록 하겠습니다.

2020. 7. 20.
윤석환